Waveguide-Based Surface-Enhanced Raman Spectroscopy for Protease Activity Detection

Golfgeleider- en oppervlakteversterkte ramanspectroscopie voor de detectie van protease-activiteit

Nina Turk

Promotoren: prof. dr. ir. R. Baets, prof. dr. K. Gevaert
Proefschrift ingediend tot het behalen van de graad van
Doctor in de ingenieurswetenschappen: fotonica

UNIVERSITEIT
GENT

Vakgroep Informatietechnologie
Voorzitter: prof. dr. ir. B. Dhoedt
Faculteit Ingenieurswetenschappen en Architectuur
Academiejaar 2020 - 2021

ISBN 978-94-6355-436-7
NUR 959, 952
Wettelijk depot: D/2020/10.500/113

UNIVERSITEIT
GENT

Universiteit Gent
Faculteit Ingenieurswetenschappen en
Architectuur
Vakgroep Informatietechnologie

Promotoren:
prof. dr. ir. Roel Baets
prof. dr. Kris Gevaert

Examencommissie:

prof. dr. ir. Filip De Turck (voorzitter)	Universiteit Gent
prof. dr. ir. Roel Baets (promotor)	Universiteit Gent
prof. dr. Kris Gevaert (promotor)	VIB-Universiteit Gent
prof. dr. Mohamed Lamkanfi	Universiteit Gent
prof. dr. Andre Skirtach	Universiteit Gent
prof. dr. Stephane Clemmen	Universiteit Gent
dr. ir. Haolan Zhao	Universiteit Gent
dr. Simon Devos	Universiteit Gent
dr. Paul Jacobs	PharmaFluidics

Universiteit Gent
Faculteit Ingenieurswetenschappen en Architectuur

Vakgroep Informatietechnologie
Technologiepark Zwijnaarde 126, 9052 Gent, België

Proefschrift tot het behalen van de graad van
Doctor in de ingenieurswetenschappen: fotonica
Academiejaar 2020-2021

Acknowledgements

I am writing this acknowledgement right as Belgium copes with the second wave of the corona pandemic. Even though 2020 has been very uniquely challenging, I am glad that I could nevertheless wrap up this PhD work. This wouldn't be possible without the support from many people. With the following words I would like to thank each and every one of you, my colleagues, friends and family for your help, advice and support.

First and foremost, I would like to thank my promoters Roel and Kris for the generous advice and guidance. I am grateful for the freedom and trust you gave me to explore and experiment extensively. I appreciate the many opportunities you have created for me to develop my career professionally and to grow as a person. I really couldn't have wished for better guides on this journey. A special mention goes to Mo, who was my bio-promotor for the first two years of my PhD. My work would not be possible without the interdisciplinary collaboration first established between the research groups of Roel and Mo. To my PhD defense jury members, I am grateful for your concise feedback that has helped to shape this thesis to its current quality.

Special thanks to Raman team members (Ali, Kristof, Haolan, Zuyang, Yang and Xiaomin). Our long but useful discussions during the Raman meeting helped me a lot throughout this journey. I am very thankful to former members of the Raman group (Ashim, Frederic and Pieter). It has been my pleasure to build my research on the foundation made by all of you during your PhD projects. Here, I would like to especially thank Pieter, who first explored the SERS sensing of protease activity, laying a solid foundation for my research work, and Ali, whose work on nanoplasmonic slot waveguides proved integral for the success of this PhD.

The heavy work of the peptide synthesis was done by Hans - thanks for

your patience when fabricating the countless iterations of the peptides. In the cleanroom, I couldn't have done without the help of Liesbet, Muhammad and Steven. Thanks to Michiel from the Cocoon group for the ALD depositions. I am also thankful to Ilse, Ilse and Kristien for your aid in all administrative and technical matters. In the end a special mention for Joan for proofreading my thesis, and Stijn for the Dutch translation of the thesis summary.

I would like to thank all the PRG group members for creating a lively work atmosphere. It was always a pleasure to have a productive discussion or just a chat in the 4th floor kitchen. Thanks to the people on the 3rd floor for all the coffee breaks. I could always drop by the office of Mahmoud and Alejandro for a quick chat or a darts match. It was always fun to spontaneously end up in a long discussion with Camiel, and with Stijn we managed to keep the office plants alive even during the first corona lockdown. I was always happy to send Ewoud pictures of cows and to see Tom's happy dance. Dennis, I hope the cava Fridays make a comeback soon! Thanks as well to all the regular guests of the lunches on the 5th floor. Irfan made my day with his carefully thought out jokes, and I could always count on Ali and Kristof to lift my spirits after a failed Raman experiment. We could count on Mimis to provide an interesting (and sometimes controversial) choice of conversation topics. And special thanks to Alessio and Margherita for the countless homemade Italian meals.

One of my favourite parts of my PhD life were the travels, either for work or for pleasure, or sometimes both. I would like to thank all my travel companions throughout the years. Andrew was my guide at my first ever conference, and later that year welcomed us on an amazing trip in Uganda. Thanks to Tomasso and Zaira for a perfect weekend trip in Tuscany, and to Joan for inviting us over to explore Catalunya. Thanks to Jeroen for inviting us for a day trip (and brunch!) to Limburg. And even though corona stopped our plan to visit Slovenia, we still could spend an awesome week exploring Alsace with Stijn and Ewoud.

Even after living abroad for many years now, I still feel right back at home every time I visit my home country thanks to the special people whom I wish to thank below in Slovenian.

Na koncu se želim zahvaliti še svojim prjateljem iz Slovenije - Tim, Primož, Tjaša, Tanja in Jakob, hvala za enkratno atomsfero vsakič, ko se dobimo, ne glede na to, koliko časa preteče vmes.

Posebna zahvala gre mojim staršem, Tonetu in Mariji, hvala za vajino podporo! Nataša, moja najljubša sestra, hvala za najine (včasih maratonske) pogovore, in veliko sreče v novem življenskem poglavju!

Ghent, November 2020
Nina Turk

Table of Contents

List of Acronyms

A

A	Alanine
ABC	Ammonium Bicarbonate
ACE	Angiotensin-Converting Enzyme
AFC	7-Amino-4-triFluoromethyl Coumarin
AIDS	Acquired Immune Deficiency Syndrome
ALD	Atomic Layer Deposition
Al_2O_3	Aluminum Oxide
AMC	7-Amino-4-MethylCoumarin

C

C	Cysteine
CARS	Coherent Anti-Stokes Raman Spectroscopy
CCD	Charge-Coupled Device
CMOS	Complementary Metal Oxide Semiconductor
CN-F	Cyano-phenylalanine
CO_2	Carbon Dioxide
COVID-19	Coronavirus Disease 2019

D

DI	Deionized
DMF	Dimethylformamide
DMSO	Dimethyl sulfoxide
DNA	Deoxyribonucleic Acid

E

E	Glutamic acid
ELISA	Enzyme-Linked ImmunoSorbent Assay
EM	Electromagnetic

F

F	Phenylalanine
FDTD	Finite-difference time-domain
Fmoc	Fluorenylmethyloxycarbonyl chloride
FRET	Fluorescence Resonance Energy Transfer
FWHM	Full Width at Half Maximum

G

G	Glycine
GluC	Endoproteinase GluC

H

HBTU	Hexafluorophosphate Benzotriazole Tetramethyl Uronium
HCP	Hexagonally Close Packed
HIV	Human Immunodeficiency Virus
HOBT	Hydroxybenzotriazole
HPLC	High Performance Liquid Chromatography

I

IR	Infrared

K

K	Lysine

L

L	Leucine
LSP(P)	Localized Surface Plasmon-Polariton
LSPR	Localized Surface Plasmon Resonance

M

MALDI	Matrix-Assisted Laser Desorption/Ionization
MMF	Multimode Fiber
MPTMS	(3-Mercaptopropyl)trimethoxysilane

MS	Mass Spectrometry

N

N_2	Nitrogen
NA	Numerical Aperture
NIR	Near Infrared
NSL	Nanosphere lithography
NTP	4-Nitrothiophenol
NWERS	Nanophotonic Waveguide-Enhanced Raman Spectroscopy

P

PMSF	Phenylmethylsulfonyl Fluoride
pNA	p-NitroAniline
PP	Plasmon-Polariton
PIC	Photonic Integrated Circuit

R

R	Arginine
RPC	Reversed-Phase Chromatography
RP-HPLC	Reverse Phase High Performance Liquid Chromatography

S

S	Serine
S0	Ground electronic State
S1	Excited electronic State
SAM	Self-Assembled Monolayer
SBR	Signal-to-Background Ratio
SEM	Scanning electron microscope
SERRS	Surface-Enhanced Resonance Raman spectroscopy
SERS	Surface-Enhanced Raman spectroscopy
Si	Silicon
Si_3N_4	Silicon Nitride
SiO_2	Silicon Oxide
SMF	Single Mode Fiber
SNR	Signal-to-Noise Ratio
SOI	Silicon On Insulator
SPP	Surface Plasmon-Polariton
SPR	Surface Plasmon Resonance
SRS	Stimulated Raman Scattering

T

TE	Transverse Electric
TFA	Trifluoroacetic acid
Ti	Titanium
TIPS	Tip Enhanced Raman Spectroscopy
TM	Transverse Magnetic
TOF	Time-Of-Flight

U

UV	Ultraviolet

V

V	Valine
VIS	Visible

W

W	Tryptophan

Y

Y	Tyrosine

Samenvatting

Proteasen zijn enzymen die de hydrolyse van peptidebindingen katalyseren. Ze spelen een belangrijke rol in veel signaalroutes en zijn belangrijke actoren in verschillende menselijke ziektes, waaronder ontstekingen, besmettelijke ziekten, kanker en neurodegeneratieve ziekten. Als zodanig zijn proteasen buitengewoon interessant als doelwit voor geneesmiddelen en worden krachtige proteaseremmers gebruikt als geneesmiddelen voor de behandeling van onder andere hart- en vaatziekten en HIV-infecties. Meer recent is de zoektocht naar een geneesmiddel voor het coronavirus dat COVID-19 veroorzaakt, gefocust op het identificeren van een geschikte remmer voor het hoofdprotease van het coronavirus, $3CL^{pro}$. Dergelijke remmers zijn over het algemeen kleine moleculen die de actieve plaats van een protease blokkeren, waardoor de activiteit hiervan wordt onderdrukt. Bij de ontwikkeling van geneesmiddelen is een gevoelige analyse van proteaseactiviteit van cruciaal belang, omdat hiermee remmers kunnen worden geïdentificeerd die de proteaseactiviteit efficiënt blokkeren. Aangezien bijna 600 genen die coderen voor proteasen geïdentificeerd zijn in het menselijk genoom, is er ook duidelijk behoefte aan een selectieve, gevoelige en gemultiplexte methode voor het meten van proteaseactiviteit.

In de afgelopen decennia zijn colorimetrische testen en vloeistofchromatografie op grote schaal gebruikt. Deze bieden echter geen hoge gevoeligheid of mogelijkheden voor multiplexing. In de afgelopen jaren zijn verschillende strategieën, gebaseerd op nanodeeltje-peptide complexen fluorescentie ontwikkeld om proteaseactiviteit te detecteren, waardoor zowel *in vitro* als *in vivo* metingen met hoge gevoeligheid mogelijk worden. Dergelijke op fluorescentie gebaseerde technieken bieden echter beperkte mogelijkheden voor multiplexing. Anderzijds maakt Ramanspectroscopie spectraal gemultiplexte metingen mogelijk door de specificiteit van Ramanspectra. Oppervlakte-versterkte Ramanspectroscopie (Surface-Enhanced Raman Spectroscopy of kortweg SERS) kan gebruikt worden om het in-

herent zwakke Raman signaal te versterken in de nabijheid van metalen nanostructuren. De typische afmetingen van plasmonische hotspots die in SERS gebruikt worden, komen goed overeen met peptiden van nanometerformaat die herkend en gesplitst worden door proteasen. Dit maakt SERS een aantrekkelijke methode om proteaseactiviteit te beoordelen via dispersie of aggregatie van SERS-nanodeeltjes in de aanwezigheid van actieve proteasen. Ongecontroleerde aggregatie van metalen nanodeeltjes kan echter reproduceerbaarheidsproblemen veroorzaken. Om deze te overwinnen, kan het peptide geïmmobiliseerd worden op een goed gecontroleerde SERS-structuur en vervolgens specifiek gesplitst worden door een protease. Dit maakt een reproduceerbare, kwantitatieve benadering mogelijk, die van groot belang is voor het detecteren van proteaseactiviteit.

Op SERS gebaseerde detectie van proteaseactiviteit berust op het volgen van het splitsen van peptidesubstraten, schematisch weergegeven in Figuur 1. Hier is het SERS-signaal afkomstig van de aromatische aminozuren. De peptiden vormen een monolaag op de gouden nanostructuren en worden vervolgens gesplitst door een protease – in dit proefschrift hebben we trypsine als modelprotease gebruikt. Terwijl het afgesplitste deel van het peptide weg van het goud oppervlak diffundeert, neemt de overeenkomstige SERS-piekintensiteit af. De verhouding in SERS-piekintensiteit kan dus als maat gebruikt worden voor de efficiëntie van de splitsing door trypsine.

Een verscheidenheid aan vrije ruimte SERS-structuren zijn ontwikkeld, die hoge en reproduceerbare SERS-verbeteringen mogelijk maken. Gouden nanodomes zijn één van de hoogst performante vrije ruimte SERS-structuren. Wuytens *et al.* (Faraday Discussions, 2017) demonstreerden SERS-waarnemingen van proteaseactiviteit met behulp van natuurlijke aromatische aminozuren op gouden nanodomes. Vrije ruimte SERS-substraten zijn echter afhankelijk van omvangrijke en dure toestellen, zoals een confocale Ramanmicroscoop, wat hun gebruik voornamelijk beperkt tot laboratoriumomgevingen. Er is in dit werk vooral gestreefd naar draagbare, geminiaturiseerde apparaten, die gevoelige en accurate spectroscopische detectie kunnen uitvoeren. Een geïntegreerde fotonische aanpak kan een oplossing bieden door verschillende vrije ruimte optische componenten op één enkele chip te brengen. Hun integratie leidt tot apparaten die robuust, goedkoop, in grote hoeveelheid reproduceerbaar en betrouwbaar zijn en bovendien parallelle analyses mogelijk maken. In de afgelopen jaren is het siliciumnitride (Si_3N_4) platform ontwikkeld, dat op golfgeleider gebaseerde excitatie en verzameling van Raman- en SERS-spectra mogelijk maakt.

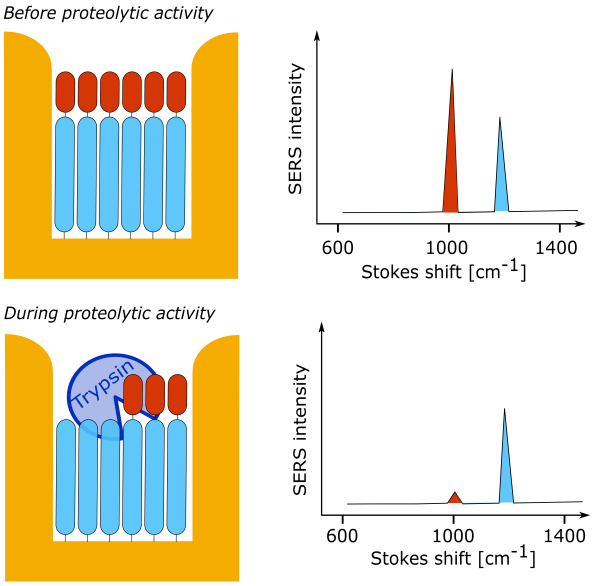

Figuur 1: Schematische representatie van de SERS-detectie van proteaseactiviteit via splitsing van peptidebindingen.

Ondanks de voortdurende verbetering van de prestaties van de op golfgeleiders gebaseerde SERS-platformen, zijn deze platformen gelimiteerd door het achtergrond signaal van het Si_3N_4. Momenteel presteren vrije ruimte SERS-substraten nog steeds iets beter dan op golfgeleiders gebaseerde SERS-platformen. Desondanks, in lopend onderzoek, worden geïntegreerde Raman-platformen steeds interessanter voor biologische toepassingen, omdat ze een geïntegreerde lab-on-a-chip aanpak mogelijk maken.

In dit werk hebben we de verschillende mogelijkheden onderzocht om de SERS-versterking van op golfgeleiders gebaseerde SERS-structuren te vergroten, om detectie van biologisch relevante moleculen met typisch lage Raman werkzame doorsneden mogelijk te maken. Op golfgeleiders gebaseerde SERS-detectie van een organische molecule nitrothiofenol (NTP) werd voor het eerst aangetoond op geïntegreerde bowtie antennes door Peyskens *et al.* (ACS Photonics, 2016). Met behulp van de geïntegreerde bowtie antennes hebben we het gebruik van een organische adhesielaag (3-mercaptopropyl)-trimethoxysilaan (MPTMS) onderzocht als vervanging voor de veelgebruikte titanium adhesielaag. We hebben aangetoond dat het gebruik van MPTMS het SERS-signaal minstens drievoudig verhoogt, maar

gepaard gaat met grote variaties in de SERS-signaalintensiteit.

Om op golfgeleiders gebaseerde SERS-detectie van proteolytische activiteit aan te tonen, hebben we daarom de recent ontwikkelde nanoplasmonische slotgolfgeleiders gebruikt, ontwikkeld door Raza *et al.* (APL Photonics, 2018), die een hogere SERS-verbetering bieden in vergelijking met de geïntegreerde bowtie antennes. Figuur 2 toont een nanoplasmonische slotgolfgeleider afgebeeld met behulp van rasterelektronenmicroscopie. Vanwege de slechtere SERS prestaties van de nanoplasmonische slotgolfgeleiders in vergelijking met vrije ruimte SERS-substraten, leveren enkel de natuurlijke aromatische zuren onvoldoende SERS-signaal voor op golfgeleiders gebaseerde detectie. Daarom hebben we een verbeterd peptidesubstraat ontwikkeld, waarbij het natuurlijke aromatische aminozuur vervangen werd door het onnatuurlijke aromatische cyano-fenylalanine. We rapporteerden dat dergelijke onnatuurlijke aromatische aminozuren kunnen gebruikt worden als SERS-reporters wanneer ze opgenomen worden in een peptide, dat vervolgens met succes gesplitst wordt door het modelprotease trypsine. Door het gebruik van het peptide met deze onnatuurlijke aromaat om op golfgeleider gebaseerde SERS-detectie van trypsine activiteit aan te tonen (Figuur 3), openen we de weg naar op SERS gebaseerde waarnemingen van protease activiteit op een geïntegreerd lab-on-a-chip platform. Aangezien slechts drie natuurlijke aromatische aminozuren, namelijk fenylalanine, tyrosine en tryptofaan, een relatief sterk SERS-signaal geven, vergroot het gebruik van onnatuurlijke aromatische aminozuren bovendien aanzienlijk de mogelijkheden van gemultiplexte metingen, waarbij de activiteit van meerdere proteasen tegelijkertijd gedetecteerd wordt. Naast cyano-fenylalanine hebben we ook de SERS-spectra van verscheidene andere onnatuurlijke aromatische aminozuren onderzocht om hun geschiktheid voor proteasemetingen te beoordelen.

Vanwege het minder efficiënte fabricageproces van de op golfgeleiders gebaseerde SERS-platformen in vergelijking met de gouden nanodomes, hebben we ook mogelijkheden onderzocht om de op golfgeleiders gebaseerde SERS-chips recycleren. Meestal wordt zuurstofplasma gebruikt om (peptide) monolagen te verwijderen om de plasmonische nanostructuren recycleren voor verdere SERS-metingen. We hebben echter aangetoond dat zuurstofplasma het SERS-achtergrondsignaal en de variabiliteit ervan verhoogt. We ontdekten dat reiniging met waterstofplasma tot veel meer reproduceerbare SERS-spectra leidt, waardoor een beter alternatief wordt geboden voor reiniging met zuurstofplasma van SERS-substraten.

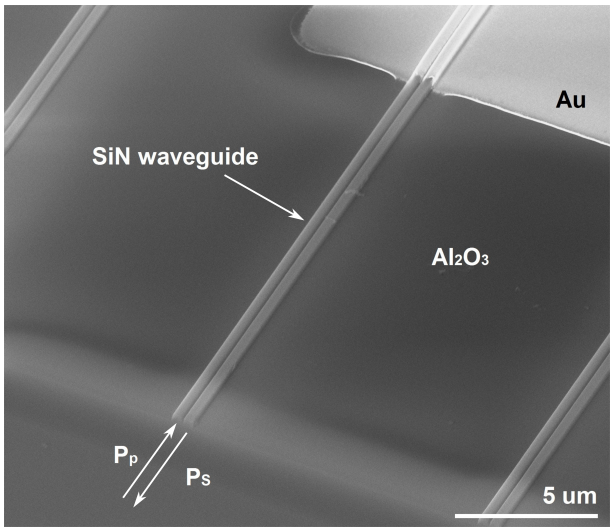

Figuur 2: Rasterelektronenmicroscopische afbeelding van de nanoplasmonische slotgolfgeleider.

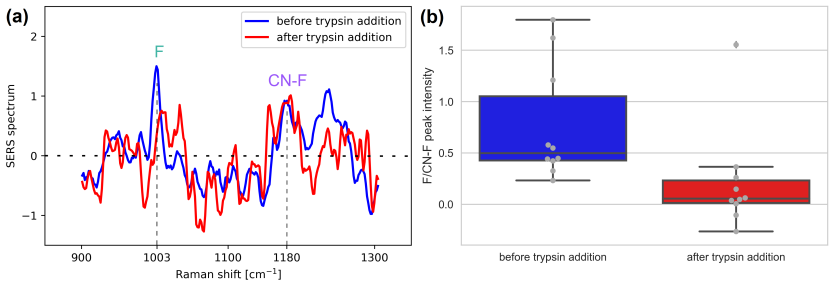

Figuur 3: (a) SERS-spectra van het peptide voor en na toevoeging van trypsine. De afname van de F piek bij 1003 cm^{-1} wijst op trypsineactiviteit. (b) Een box plot van de F/CN-F piekintensiteiten voor en na toevoeging van trypsine.

Tot slot, in dit proefschrift hebben we ons gericht op het ontwikkelen van een hoog-performant op golfgeleiders gebaseerd SERS-platform voor gemultiplexte detectie van de proteaseactiviteit. Omdat de aard van dit werk sterk interdisciplinair is, benaderden we dit zowel van de fotonische als van de biochemische kant. Aan de fotonicazijde hebben we dit probleem op volgende manieren aangepakt:

- Gebruik maken van MPTMS als alternatief voor de titanium adhesielaag om de SERS-signalen 3-voudig te verbeteren op geïntegreerde bowtie antennes.
- Vervangen van reiniging met zuurstofplasma van de op golfgeleiders gebaseerde SERS-substraten door reiniging met waterstofplasma om de vervuiling van de peptide monolaag te minimaliseren.
- Onderzoeken van verschillende op golfgeleiders gebaseerde SERS-substraten qua signaalverbetering om de best presterende te bepalen.

Van de biochemische kant hebben we de volgende onderwerpen onderzocht:

- Gebruik maken van onnatuurlijke aromatische aminozuren om de Raman werkzame doorsnede van het peptidesubstraat te verbeteren en gemultiplexte metingen uit te voeren.
- Aantonen dat het peptide met ingebouwde onnatuurlijke aromatische aminozuren efficiënt gesplitst kan worden door onze modelprotease.
- Ontwerpen en synthetiseren van complementaire peptidesubstraten voor verschillende proteasen (hier, trypsine en endoproteïnase-GluC) om gemultiplexte detectie van proteaseactiviteit aan te tonen.

Door de twee benaderingen te combineren, waren we in staat om de nanoplasmonische slotgolfgeleider te gebruiken om SERS-detectie van proteaseactiviteit met behulp van onnatuurlijke aromatische aminozuren aan te tonen. Er zijn echter verdere inspanningen nodig om de multiplexing mogelijkheden van dit platform te demonstreren.

Summary

Proteases are enzymes that catalyze the hydrolysis of peptide bonds. They play important roles in many signaling pathways and are important actors in several human diseases, including inflammation, infectious diseases, cancer and neurodegenerative diseases. As such, proteases are extremely interesting as drug targets and potent protease inhibitors are used as drugs to treat cardio-vascular diseases and HIV infection amongst others. More recently, the drug search for the coronavirus causing COVID-19 focuses on identifying a suitable inhibitor for the coronavirus main protease $3CL^{pro}$. Such inhibitors are generally small molecules that block the active site of a protease, thereby suppressing its activity. In drug development, sensitive analysis of protease activity is of crucial importance as it allows to identify inhibitors that efficiently block protease activity. As almost 600 genes coding for proteases have been identified in the human genome, there is also a clear need for a selective, sensitive and multiplexed method for measuring protease activities.

In the past decades, colorimetric assays and liquid chromatography have been widely used. However, these do not offer a high sensitivity or multiplexing capabilities. In recent years, different strategies based on nanoparticle-peptide complexes used fluorescence to detect protease activity, offering high sensitivity measurements both *in vitro* and *in vivo*. Such fluorescence-based techniques however provide limited multiplexing possibilities. On the other hand, Raman spectroscopy enables spectrally multiplexed measurements due to the specificity of Raman spectra. Surface-Enhanced Raman Spectroscopy (SERS) can be used to enhance the inherently weak Raman signal in close proximity to metallic nanostructures. The typical sizes of the plasmonic hotspots used in SERS match well with the nanometer-sized peptides recognized and cleaved by proteases. This makes SERS an attractive method for assessing protease activity, which can be detected via dispersion or aggregation of SERS nanoparticles in the presence of proteases. Uncontrolled

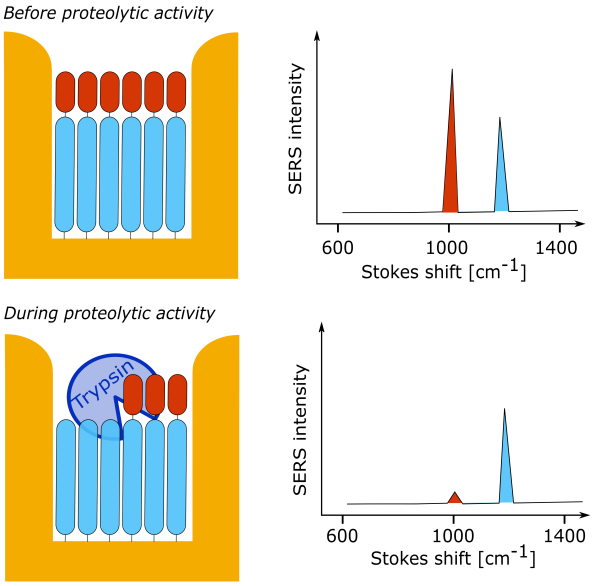

Figure 4: The concept of protease activity detection via peptide bond cleavage using SERS.

aggregation of metal nanoparticles can however create reproducibility issues. To overcome these, the peptide can be immobilized on a well-controlled SERS structure and then specifically cleaved by a protease. This allows a reproducible, quantitative approach of great interest for protease activity sensing.

SERS-based protease activity sensing relies on monitoring cleavage of peptide substrates, shown schematically in Figure 4. Here, the SERS signal originates from the aromatic amino acids. The peptide forms a monolayer on the gold nanostructures and is then cleaved by a protease – in this thesis, we used trypsin as a model protease. As the cleaved-off part of the peptide diffuses away from the gold surface, its corresponding SERS peak intensity decreases. The SERS peak intensity ratio can thus be used as a metric for the efficiency of trypsin cleavage.

A variety of free-space SERS structures enabling high and reproducible SERS enhancements has been developed, and among them are gold nanodomes. Wuytens *et al.* (Faraday Discussions, 2017) demonstrated SERS sensing of protease activity using natural aromatic amino acids on gold nanodomes. However, free-space SERS substrates rely on bulky and expensive

instrumentation such as a confocal Raman microscope, which mostly limits their use to laboratory environments. There has been a push for portable miniaturized devices, which can perform sensitive and accurate spectroscopic detection. An integrated photonics approach can offer a solution by bringing various free-space optical components to a single chip. Their integration leads to devices that are robust, cheap, mass-reproducible and reliable, and additionally allow parallel analyses. In recent years, the silicon nitride (Si_3N_4) platform was developed, which enables waveguide-based excitation and collection of Raman and SERS spectra. Despite the continuous improvement in the performance of the waveguide-based SERS platforms, these platforms are limited by background signal of the Si_3N_4. Currently, free-space SERS substrates still slightly outperform waveguide-based SERS platforms. Nevertheless, with ongoing development, integrated Raman platforms are becoming increasingly interesting for biological applications as they enable an integrated lab-on-a-chip approach.

In this work, we examined the different possibilities to increase SERS enhancement of the waveguide-based SERS structures to allow to detect biologically relevant molecules with typically low Raman cross-sections. Waveguide-based SERS detection of an organic molecule nitrothiophenol (NTP) was first demonstrated on integrated bowtie antennas by Peyskens *et al.* (ACS Photonics, 2016). Using the integrated bowtie antennas, we explored the use of an organic adhesion layer (3-mercaptopropyl)-trimethoxysilane (MPTMS) as a substitute for the widely used titanium adhesion layer. We showed that the use of MPTMS increases the SERS signal at least 3-fold, but is however associated with big variations in the SERS signal intensity.

To demonstrate waveguide-based SERS detection of proteolytic activity, we therefore used the recently developed nanoplasmonic slot waveguide developed by Raza *et al.* (APL Photonics, 2018), which provides higher SERS enhancement compared to the integrated bowtie antennas. Figure 5 shows the image of nanoplasmonic slot waveguide acquired using scanning electron microscopy. However, due to the poorer SERS performance of the nanoplasmonic slot waveguide compared to free-space SERS substrates, the natural aromatic acids only do not provide sufficient SERS signal for waveguide-based detection. We therefore developed an improved peptide substrate, where the natural aromatic amino acid was replaced by the non-natural aromatic cyano-phenylalanine. We reported that such non-natural aromatics can be used as SERS reporters when incorporated in a peptide,

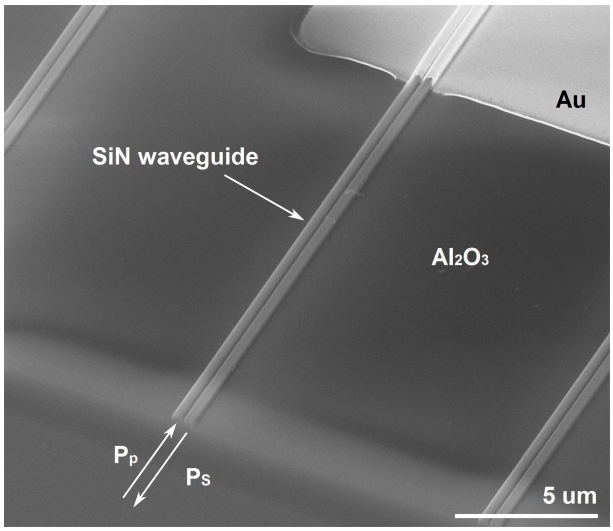

Figure 5: Scanning electron microscopy image of the nanoplasmonic slot waveguide.

which is then successfully cleaved by the model protease trypsin. By using the peptide with the incorporated non-natural aromatic to show waveguide-based SERS detection of trypsin activity (Figure 6), we open the way towards SERS-based monitoring of protease activity on an integrated lab-on-a-chip platform. Considering that only the three natural aromatic amino acids, namely phenylalanine, tyrosine and tryptophan, provide a relatively high SERS signal, the use of non-natural aromatics furthermore significantly extends the possibilities of multiplexing measurements, during which the activity of several proteases is simultaneously detected. Besides cyano-phenylalanine, we also examined the SERS spectra of several other non-natural aromatics to assess their suitability for protease sensing.

Due to the less efficient fabrication process of the waveguide-based SERS platforms compared to the gold nanodomes, we also explored possibilities to clean and reuse the waveguide-based SERS chips. Oxygen plasma is typically used to remove (peptide) monolayers in order to clean and reuse the plasmonic nanostructures for further SERS measurements. We however showed that oxygen plasma increases the SERS background signal and its variability. We found that hydrogen plasma cleaning leads to much more reproducible SERS spectra, thus providing a better alternative to oxygen plasma cleaning of SERS substrates.

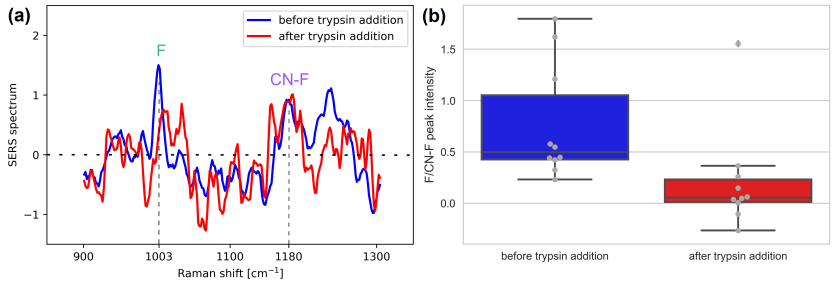

Figure 6: (a) SERS spectra of the peptide before and after trypsin addition. The decrease in the F peak at 1003 cm^{-1} indicates trypsin-mediated cleavage of the peptide. (b) A box plot of F/CN-F peak intensities before and after trypsin addition.

To conclude, in this thesis work we focused on developing a high-performing waveguide-based SERS platform for multiplexed detection of the protease activity. As the nature of this work is highly interdisciplinary, we approached this from both the photonics and the biochemical side. From the photonics side, we tackled this problem in the following ways:

- Using MPTMS as an alternative to titanium adhesion layer in order to improve the SERS signals 3-fold on integrated bowtie antennas.
- Replacing oxygen plasma cleaning of the waveguide-based SERS substrates with hydrogen plasma cleaning to minimize the contamination from the peptide monolayer.
- Examining several different waveguide-based SERS substrates in terms of their signal enhancement to determine the best performing one.

From the biochemical side, we explored the following topics:

- Using non-natural aromatic amino acids to enhance the Raman cross-section of the peptide substrate and perform multiplexing measurements.
- Demonstrating that the peptide with incorporated non-natural aromatics can be efficiently cleaved by our model protease.
- Designing and synthesizing complementary peptide substrates for different proteases (here, trypsin and endoproteinase-GluC) to demonstrate multiplexed detection of protease activity.

By combining the two approaches, we were able to use the nanoplasmonic slot waveguide to demonstrate SERS detection of protease activity using non-natural aromatics. Further effort is however needed to demonstrate the multiplexing capabilities of this platform.

1 Introduction

1.1 Background and rationale

Light has always played a crucial role in studying biological phenomena. From the discovery of the cell using the optical microscope, to the spectroscopic methods used in modern day medical diagnostics and drug development, interaction of light with biomolecules allows sensitive, non-invasive studies of biological processes. The continuous development of optical and photonic biosensing techniques has however resulted in increasingly complicated and expensive laboratory equipment needed to support analyses. To address this, an integrated photonics approach aims to bring the various free-space optical components to a single miniaturized device. These photonic chips are mass-reproducible, cheap, robust and reliable, and they vastly expand the possibilities to use the advanced optical techniques outside a laboratory environment [1].

The main objective of my thesis work was to implement an integrated approach for protease sensing. Proteases are enzymes that hydrolyze peptide bonds in proteins and peptides, and they play important roles in a variety of human diseases, ranging from cardiovascular diseases to AIDS [2]. Very recently, the drug search for the coronavirus causing COVID-19 is focusing

on identifying an inhibitor for the main viral protease $3CL^{pro}$ [3, 4]. Proteases are thus important drug targets, and efficient and sensitive techniques to monitor their activity are required to identify inhibitors than can be used as potential drugs.

A variety of established and novel techniques for the detection of protease activities exists. Typically, mass spectrometry, fluorescence and colorimetric assays are used for protease activity sensing [5]. Whereas mass spectrometry is a very sensitive technique, it is quite labor-intensive and requires the use of expensive instruments. Colorimetric and fluorescence assays can be performed using more affordable absorption spectrometers, but require the use of external labels. They furthermore provide only limited multiplexing abilities, during which the activity of several proteases can be monitored simultaneously. Novel techniques have therefore emerged to mitigate these problems and detection of protease activities was demonstrated using electrochemical, liquid crystal and SERS assays.

Surface-Enhanced Raman Spectroscopy (SERS) sensing relies on probing vibrational frequencies of molecules, thereby obtaining a vibrational spectrum which is highly specific for each molecule. The Raman signals are however inherently weak, and one of the most widely used ways to enhance them is by using SERS. Here, the Raman signals are enhanced up to 10^7-times in the proximity of metal nanostructures [6]. SERS thus has the potential to provide a sensitive and specific method for detection of protease activity. It is furthermore label-free, offering a big advantage over fluorescence techniques, and enables extensive multiplexing [5].

In my thesis, I focused on SERS-based protease activity detection by monitoring proteolytic cleavage of a peptide substrate[1]. To translate this technique from free-space to a waveguide-based platform, we approached this from both the biochemical and photonics point of view. We succeeded in increasing the Raman cross section of the peptide substrate by using a peptide substrate with incorporated non-natural aromatic amino acids. In parallel, we worked on increasing the SERS enhancements offered by the waveguide-based SERS platforms. By combining the two approaches, we were able to demonstrate waveguide-based SERS detection of trypsin

[1]The term 'substrate' is used in both protease and SERS research to name two different concepts. In SERS, a substrate is a nanostructured surface that provides a localized surface-plasmon resonance responsible for the SERS enhancement. When referring to the proteases, a substrate is the material upon which the protease acts, i.e. the peptide chain, which is cleaved by the protease. In this thesis, we use the terms SERS substrate and peptide substrate in order to distinguish between the two.

activity.

1.2 Thesis outline

In **Chapter 2**, the principles of Raman spectroscopy and SERS are introduced. First, the theoretical background of Raman spectroscopy is described, followed by a discussion on the differences between different kinds of spectroscopies, their advantages and drawbacks, especially in the context of sensing of biological molecules. Next, we introduce basic concepts of plasmon physics, which enables SERS measurements. Both Raman spectroscopy and SERS are usually measured in free-space using a confocal Raman microscope. As in my thesis the confocal Raman microscope is used extensively, we describe its working principle. Further, we discuss how photonic integrated chips can replace the bulky Raman microscope, providing a cheap, reproducible and sensitive way of measuring both Raman and SERS signals.

The motivation for the use of SERS in protease activity detection is explained in **Chapter 3**. First, the proteases and their catalytic properties are described, followed by a section on the role proteases play in the various human pathologies. Given such crucial roles of proteases in different diseases, fast, efficient and reliable techniques for protease activity detection are needed for the pharmacological search for protease inhibitor-based drug development. An overview of established and more novel methods of protease activity sensing is given, along with the motivation for the use of SERS for detecting protease activity.

In **Chapter 4**, the principle of SERS detection of protease activity via peptide substrate cleavage is presented. There, also the use of different non-natural aromatic amino acids as Raman reporters is explored. Further, we discuss the design of the peptide substrate in order to achieve a peptide monolayer on the gold surface of the SERS substrate. We present an overview of different peptides we fabricated as substrates for trypsin and endoproteinase-GluC, and summarize the problems encountered during peptide production.

The transition from free-space to waveguide-based SERS substrates is described in **Chapter 5**. The main challenge faced here was the fact that the waveguide-based SERS substrates are currently still underperforming compared to the more established free-space substrates. To mitigate this, the

use of an organic adhesion layer of MPTMS was examined as an alternative to the typically used titanium adhesion layer. The use of MPMTS did provide a limited improvement of the SERS signal of the integrated bowtie antennas however, nanoplasmonic slot waveguides emerged as better performing waveguide-based SERS platforms. The different waveguide-based SERS platforms were compared to the free space-based gold nanodomes. Finally, the cleaning of the SERS substrates was examined in order to reuse the samples and extend their lifetime.

Chapter 6 focuses on the implementation of the waveguide-based SERS sensing of trypsin activity. To increase the Raman cross section of the peptide substrate, we used peptides containing non-natural aromatics. The efficiency of trypsin cleavage of these substrates was first assessed using RP-HPLC, and then using gold nanodomes in a free space-based SERS experiment. Finally, we used the nanoplasmonic slot waveguide to demonstrate waveguide-based SERS detection of trypsin activity.

In **Chapter 7**, we draw the most important conclusions resulting from this PhD project, and highlight the possible future directions of our work.

1.3 Attribution of work

This PhD was conceived as an interdisciplinary collaboration between the Photonics Research Group (UGent-imec, prof. R. Baets), the Inflammation Research Center (VIB-UGent, prof. M. Lamkanfi) and Center for Medical Biotechnology (VIB-UGent, prof. K. Gevaert), established during the PhD project of P. Wuytens [7]. The main purpose of this collaboration was to develop a generic SERS-based platform for detecting protease activity. The proof-of-concept SERS detection of trypsin activity was achieved using peptides with natural aromatics on gold nanodomes in free-space configuration, as demonstrated by P. Wuytens. In this PhD project, the main ideas were to demonstrate the waveguide-based protease activity sensing using SERS, and to additionally show multiplexing measurements of protease activity.

Since the nature of this PhD project was highly interdisciplinary, the author worked closely with several collaborators to tackle the different aspects of the work. In the following paragraphs, the contribution of the collaborators to this project is summarized.

The photonics side of the research was supervised by prof. R. Baets. P. Wuytens developed the free-space gold nanodomes, and A. Raza developed

the nanoplasmonic slot waveguides, which were fabricated by the author to perform the protease experiments. For the fabrication of the nanoplasmonic slot waveguide, the atomic layer deposition of aluminum oxide was developed by M. van Daele, J. Dendooven and C. Detavernier, and performed by M. van Daele. The SERS experiments were performed on a confocal Raman microscope under the guidance of prof. A. Skirtach.

From the biochemical perspective, the first two years of research were supervised by prof. M. Lamkanfi. After prof. Lamkanfi left UGent and VIB for a job in industry, prof. K. Gevaert stepped in as a co-promotor for the rest of the PhD project. In his lab, H. Demol was instrumental in fabricating the peptides with non-natural aromatic amino acids and performing mass spectrometry measurements. All the protease cleavage experiments using HPLC and SERS were performed by the author.

1.4 Publications

This dissertation has led to the following list of publications in conferences and international peer-reviewed journals.

1.4.1 Publications in international journals

1. **N. Turk**, A. Raza, P.C. Wuytens, H. Demol, M. van Daele, C. Detavernier, A. Skirtach, K. Gevaert, R. Baets,"Waveguide-based surface-enhanced Raman spectroscopy detection of protease activity using non-natural aromatic amino acids", *Biomedical Optics Express*, 11(8), pp.4800-4816, 2020.

2. **N. Turk**, A. Raza, P.C. Wuytens, M. Van Daele, C. Detavernier, A. Skirtach, K. Gevaert, R. Baets,"Comparison of Free-Space and Waveguide-Based SERS Platforms", *Nanomaterials*, 9(10), 1401, 2019.

3. X. Nie, **N. Turk**, Y. Li, Z. Liu, R. Baets, "High extinction ratio on-chip pump-rejection filter based on cascaded grating-assisted contra-directional couplers in silicon nitride rib waveguides", *Optics Letters*, 44(9), pp. 2310–2313, 2019.

4. P.C. Wuytens, H. Demol, **N. Turk**, K. Gevaert, A.G. Skirtach, M. Lamkanfi, R. Baets, "Gold Nanodome SERS platform for label-free detection of protease activity", *Faraday Discussions*, 205(345), pp. 345-361, 2017.

1.4.2 Publications in international conferences

1. **N. Turk**, A. Raza, P.C. Wuytens, H. Demol, M. van Daele, C. Detavernier, A. Skirtach, K. Gevaert, R. Baets,"Waveguide-based Detection of Protease Activity using Surface-Enhanced Raman Spectroscopy", Frontiers in Optics 2020 (online conference).

2. **N. Turk**, H. Demol, A. Skirtach, R. Baets, K. Gevaert,"Towards SERS-based multiplexed monitoring of protease activity using non-natural aromatic amino acids", EOS Annual Meeting 2020 (online conference).

3. **N. Turk**, A. Skirtach, K. Gevaert, R. Baets, "Hydrogen plasma cleaning of gold plasmonic nanostructures for better reproducibility of the SERS spectra", Proceedings of the 24th Annual Symposium of the IEEE Photonics Benelux Chapter, the Netherlands, 2019.

4. X. Nie, **N. Turk**, Z. Liu, R. Baets, "Grating assisted contra-directional filters with high rejection ratio in silicon nitride rib waveguides", European Conference on Integrated Optics (ECIO 2019), Belgium, paper T.Po2.11, 2019.

5. **N. Turk**, A. Raza, P.C. Wuytens, H. Demol, A. Skirtach, K. Gevaert, R. Baets, "Towards SERS-based on-chip detection of protease activity using nanoplasmonic slot waveguides", Proceedings of the 23rd Annual Symposium of the IEEE Photonics Benelux Chapter, Belgium, 2018.

6. **N. Turk**, P.C. Wuytens, H. Demol, K. Gevaert, A. Skirtach, M. Lamkanfi, R. Baets, "Towards multiplexed SERS-based on-chip detection of protease activity", International Conference on Biomedical Photonics, France, 2018.

7. **N. Turk**, P.C. Wuytens, A. Raza, A. Skirtach, R. Baets, "Organic Adhesion Layer for an Increased Waveguide-Excited Surface-Enhanced Raman Signal", Frontiers in Optics, United States, paper JW3A.82, 2017.

1.4.3 Publications in national conferences

1. P.C. Wuytens, A. Raza, H. Zhao, **N. Turk**, F. Peyskens, X. Nie, A. Dhakal, E.M.P. Ryckeboer, S. Clemmen, N. Le Thomas, R. Baets, "On-chip Raman Spectroscopy", FEA Research Syposium 2017, Belgium, 2017.

2

Introduction to Raman spectroscopy and SERS

Raman spectroscopy enables the acquisition of a distinctive spectral fingerprint of a molecule without the need for external labels. It is based on the Raman scattering process, probing the vibrational frequencies of the molecules. Raman signals are however extremely weak, so Surface Enhanced Raman Spectroscopy (SERS) can be used to enhance the Raman signal close to the surface of metal nanostructures, providing a sensitive and selective method for the detection of various analytes. A free-space Raman microscope is typically used to detect the Raman and the SERS spectra. In the last years, waveguide-based Raman and SERS platforms have emerged where the excitation and the collection of the signals is done on an integrated photonic chip, bringing several advantages over conventional free-space Raman microscopy.

In this chapter, we take a look at the commonly used spectroscopic techniques and highlight the advantages Raman spectroscopy offers compared to the other techniques. Next, we describe the basic concepts of Raman spectroscopy. We continue with the explanation of the surface-enhanced Raman scattering, and describe the confocal Raman microscope used for the acquisition of the Raman and SERS spectra in free space. In the end,

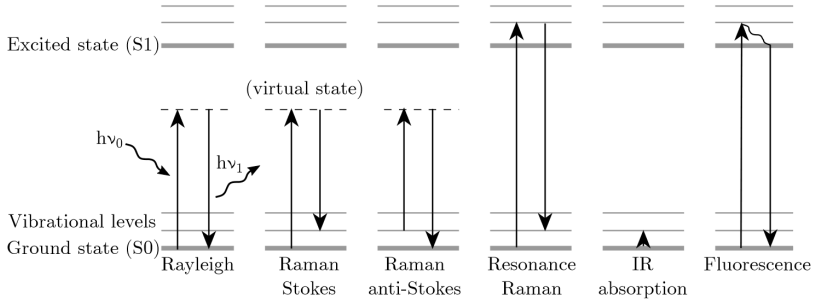

Figure 2.1: Jablonski diagrams of different linear scattering and absorption processes. Adapted from [7].

we give a short overview of waveguide-based Raman and SERS platforms that have lately emerged as an alternative to the conventional free-space approach.

2.1 Overview of spectroscopic techniques

Spectroscopy is the analysis of the interaction between matter and light. The response of the analyte molecules to the incident light at various frequencies reveals some information about the analyte. In spectroscopy, a molecule can be treated as a dipole oscillating at a specific frequency, which interacts with the incident electromagnetic field. This formalism will be used in the next section to derive the vibrational modes of the molecule, important in Raman spectroscopy. Besides the vibrational modes, the molecule also has its own rotational and electronic modes. Different spectroscopic techniques have been developed to study the electronic, vibrational and rotational transitions of the molecule. The fluorescence spectroscopy studies the electronic transitions, whereas the Raman and the infrared (IR) absorption spectroscopy use the vibrational transitions to examine the analyte. The rotational transitions can be studied by absorption spectroscopy and are typically found in the microwave spectral region.

In this section a short overview of the spectroscopic techniques is presented, with the special emphasis on the Raman, fluorescence and near IR spectroscopy. These widely used spectroscopic techniques can be used to complement each other, so special attention is given to the comparison of the different techniques.

Different linear scattering and absorption processes are explained with the help of the Jablonski diagram in Figure 2.1. Here, the electronic state of the molecule are indicated as S0 for the ground state and S1 for the excited state. Each electronic state then has its own subset of the vibrational states. The concept of a 'virtual state' helps us explain the Rayleigh and Raman scattering, but it does not have a physical meaning. It can be imagined as a transient state that is populated after the absorption of the incident photon and before the emission of the scattered photon.

2.1.1 Fluorescence spectroscopy

When the energy of the absorbed photon is equal or greater than that of an electron transition, the excited electron transitions to a vibrational mode of the excited state (S1). The electron is excited to one of the higher vibrational states of the excited electronic state and then decays to the lowest vibrational level of the excited electronic state (S1) due to the non-radiative dissipation of the absorbed energy. Next, the electron falls back to the ground electronic state (S0), while emitting a red-shifted photon with lower energy (Stokes photon).

Compared to the virtual levels in Rayleigh and Raman scattering, the presence of a real energy level in fluorescence results in a finite time of several nanoseconds between the absorption and the emission of the photons. In Raman scattering, this time is on the other hand on a scale of only a few picoseconds [8]. Fluorescence is also much stronger than Raman scattering, since it involves the resonant electronic transitions. In the most optimal cases, the fluorescent scattering can be $10^{10} - 10^{14}$ times stronger than the Raman scattering of a comparable molecule.

Fluorescence however only occurs at specific wavelengths that are characteristic for each molecule, and depend on the energy of the electronic transitions. Fluorescent labels are therefore usually needed to detect the molecule of interest [9]. The development of fluorescent labels with large scattering cross sections has led to the widespread use of fluorescence in a variety of (bio)applications, such as DNA sequencing, cell identification, genetics and environmental monitoring.

The addition of external fluorescent labels can however also change the intrinsic properties of the analyte we wish to investigate. Fluorescent labels can furthermore experience photobleaching, i.e. the gradual loss of fluorescence properties due to the chemical changes in the molecule. In this

regard, Raman spectroscopy can be a preferred alternative to fluorescence.

2.1.2 IR absorption spectroscopy

Absorption spectroscopy measures the absorption of electromagnetic radiation caused by its interaction with a sample. The sample is illuminated with the light of different frequencies, and it only absorbs the light at the frequencies that correspond to the internal energy transitions of the molecule.

In infrared (IR) absorption spectroscopy, the energy of the absorbed photon equals the energy difference between the two vibrational modes. Upon absorption of the photon, the electron is thus excited in the higher vibrational state. At room temperature, most of the electrons are in the lowest vibrational state, thus making the transition between the ground and the first excited vibrational state the most probable. This transition is called the fundamental transition, and is much more probable compared to the hot band transitions between the higher vibrational states.

It can be shown that the vibrations are IR active only when the vibrational mode experiences a change in the dipole moment [10]. In the case of the CO_2 molecule, that occurs for the vibration states ν_2 and ν_3 (Figure 2.5). These states can therefore be probed by IR absorption spectroscopy, whereas the vibrational state ν_1 can be probed by Raman spectroscopy, as explained in Section 2.2. These techniques are thus complementary, and only by employing both of them all the vibrational states of an analyte molecule can be fully examined. In practice, one can notice that the IR-modes are not always necessarily Raman-inactive - for non-centrosymmetric molecules some of the IR-active modes are also Raman-active.

To make the results more comparable, both Raman and IR absorption spectra are usually expressed in terms of the relative inverse wavelength shift, i.e. the wavenumber, with units [cm^{-1}]:

$$\Delta\lambda_S = \frac{1}{\lambda_0} + \frac{1}{\lambda_S} \tag{2.1}$$

where λ_0 is the excitation wavelength and λ_S the Stokes scattered wavelength. The wavenumber is thus independent of the excitation wavelength, simplifying the comparison of spectra acquired at different excitation wavelengths.

Typically, the IR absorption transitions happen in the mid-infrared region, requiring the use of the more expensive sources and detectors in the

Figure 2.2: Absorption spectrum of water. [11]

mid-IR region. These requirements can be partly relaxed due to the large scattering cross sections of the IR absorption compared to the Raman scattering. Important drawback, especially when examining the biological samples, can also be the strong absorption of water in the mid-IR region. The water absorption is however significantly lower in the range of 400-1000 nm, which is more suitable for the typical excitation wavelengths in Raman spectroscopy.

2.1.3 Raman spectroscopy

The scattering of light in matter can be elastic (i.e. Rayleigh scattering) or inelastic Raman scattering. The latter consists of the Stokes component emitted with the frequency $\omega_0 - \omega_S$ and the anti-Stokes contribution at $\omega_0 + \omega_S$. The ratio of the intensity of anti-Stokes compared to the Stokes scattered light additionally depend on the Boltzmann factor, which states that the higher energy states are comparatively more populated at higher temperatures. The ratio between Stokes and anti-Stokes scattered power is thus determined as:

$$\frac{P_{aS}}{P_S} = \frac{(\omega_0 + \omega_s)^4}{(\omega_0 - \omega_S)^4} e^{-\frac{\hbar\omega_S}{k_B T}} \tag{2.2}$$

where $\hbar$ is the reduced Planck constant, k_B the Boltzmann constant and ω_s the frequency of the molecular vibration. At room temperature, the Rayleigh, anti-Stokes and Stokes scattered light intensities are in the order of 10^{-5}, 10^{-11}, 10^{-8} respectively, normalized to the incident intensity.

These numbers are typical for the Stokes shift in the order of approx. 0.3 eV (approx. 2500 cm^{-1}). At different Stokes shifts and temperatures, the intensity ratio of Stokes and anti-Stokes scattering can vary from the above mentioned values.

Since anti-Stokes scattering is much lower at room temperature, in this work only the Stokes scattering is measured. The weaker anti-Stokes scattering might however be of interest when the fluorescent background presents an issue. As opposed to the Stokes spectrum, the anti-Stokes spectrum is completely free of the fluorescence background due to the fact that the fluorescent processes only scatter photons with lower energy than the incident.

In the Eq. 2.20 in the next section we establish the dependence of the Raman cross section on the wavelength of the incident light $\sigma \propto \frac{1}{\lambda^4}$. This dependence means that the Raman response of the molecule will be stronger at shorter wavelengths. The advantage of using the lower wavelengths is also lower heat absorption by the analyte. On the other hand, as mentioned in the previous paragraph, the fluorescence background at shorter λ can be high and thus potentially mask the weak Raman signals. The red and near IR excitation wavelengths (for example the 785 nm laser) provide a good compromise for Raman spectroscopy.

Resonance Raman scattering is a special case of the Raman scattering. It is characterized by the excitation wavelengths that are at or very close to the resonant wavelengths of the electronic transitions (Figure 2.1). Resonance Raman scattering enhances the intensity of the scattered light, but also suffers from the strong fluorescence background. The fluorescent background can however be quenched in the nanometer proximity of silver or gold nanostructures. The scattering cross section in the Surface-Enhanced Resonance Raman Scattering (SERRS) can be comparable to that of the fluorescent molecule.

In this section, different widely used spectroscopic techniques were compared. Whereas Raman spectroscopy offers several advantages over fluorescence and IR spectroscopy, its main drawback are the inherently weak Raman cross sections that limit the amount of Raman scattered light. For comparison, the scattering cross sections of the three different spectroscopic techniques are listed for the molecule of rhodamine 6G in Table 2.1. Several techniques have been developed to enhance the Raman signal, including resonance Raman spectroscopy (mentioned above), tip-enhanced Raman spectroscopy (TIPS) and surface-enhanced Raman spectroscopy (SERS). The latter relies on the metal nanoparticles, which enhance the Raman

Scattering process	λ_0 [nm]	σ [cm^2]	Reference
Absorption	514	10^{-16}	[12]
Fluorescence	514	10^{-16}	[12]
Resonance Raman	532	10^{-24}	[13]
Raman	785	10^{-27}	[7]

Table 2.1: Comparison of absolute scattering cross sections of the molecule of rhodamine 6G.

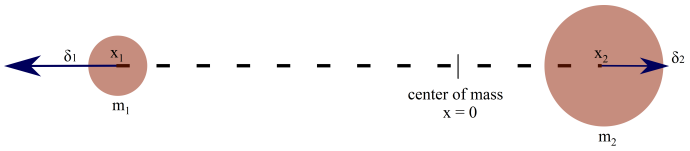

Figure 2.3: A simple molecule consisting of two atoms.

signals of the analyte molecules close to the metal surface. It is widely used in a variety of (bio)applications, and as the main topic of this thesis discussed more in detail in the Section 2.3.

2.2 Light-matter interaction in Raman scattering

All scattering processes are a result of the interaction of atoms with light. For a detailed understanding of the Raman scattering, the quantum theory is required to derive the energy levels of the atoms and molecules, and explain the interaction of photons with these energy states. On the other hand, the simpler classical theory can be used to sufficiently explain the Raman scattering and SERS for the purposes of this thesis, based on [12] and [14]. In this section the classical approach is therefore used to examine the vibrational states of a simple two-atom molecule. We then describe the interaction of this molecule with the incident electromagnetic (EM) wave leading to the generation of Raman scattering. The reader can find a more detailed treatment of the topic using quantum mechanics in [10], [15], [16]and [17].

The two-atom molecule can be treated using the classical approach as a spring, as shown in Figure 2.3. The atoms in the molecule have masses m_1 and m_2, and are situated at positions x_1 and x_2 in the equilibrium, with the center of mass at $x = 0$. Under an external force the atoms are displaced by

δ_1 and δ_2, while the center of mass is conserved:

$$\delta_1 = \frac{m_2}{m_1}\delta_2 \tag{2.3}$$

In the harmonic approximation the molecule obeys Hooke's law where the force required to displace the spring is proportional to the displacement:

$$F = -k(\delta_1 + \delta_2) = -k\frac{m_1 + m_2}{m_2}\delta_1 = -k\frac{m_1 + m_2}{m_1}\delta_2 \tag{2.4}$$

where k is the spring constant. Using the Newton's second law $F = ma$ we get the equation of the harmonic oscillator:

$$\frac{m_1 m_2}{m_1 + m_2}\left(\frac{\mathrm{d}^2\delta_1}{\mathrm{d}t^2} + \frac{\mathrm{d}^2\delta_2}{\mathrm{d}t^2}\right) = -k(\delta_1 + \delta_2) \tag{2.5}$$

To simplify the equation, we define reduced mass as $\mu = \frac{m_1 m_2}{m_1 + m_2}$ and the displacement q as $\delta_1 + \delta_2$. We can therefore write Eq. 2.5 as:

$$\mu\frac{\mathrm{d}^2 q}{\mathrm{d}t^2} = -kq \tag{2.6}$$

The solution to this equation is a harmonic oscillation:

$$q = q_0(e^{i\omega_S t} + e^{-i\omega_S t}) \tag{2.7}$$

where the angular frequency is defined as:

$$\omega_S = 2\pi\nu_S = \sqrt{\frac{k}{\mu}} \tag{2.8}$$

The potential energy U for this harmonic oscillation has the shape of a parabolic well:

$$U = \frac{1}{2}kq^2 \tag{2.9}$$

A more realistic model of the potential energy of a molecule has the shape of Morse potential. The comparison between the two is shown in Figure 2.4. The energy levels of the harmonic oscillator are evenly spaced by $\hbar\omega$, but in Morse potential the energy differences between the higher order transitions decrease. In Morse potential, also the effects of bond breaking are included, as well as the anharmonicity of real bonds and the non-zero transition probability for overtone and combination bands.

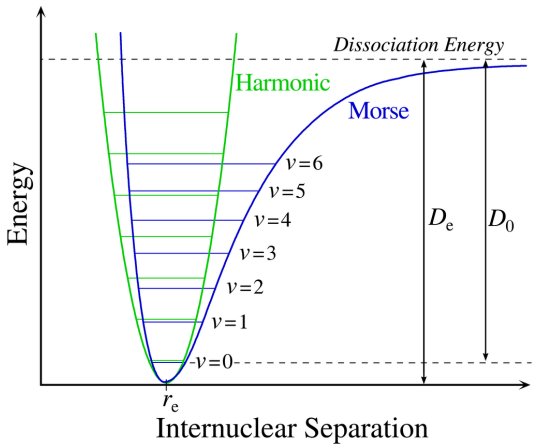

Figure 2.4: Comparison of the vibrational energy levels in the parabolic potential well of a harmonic oscillator and the more realistic Morse potential. [18].

Next, we examine the interaction of the model two-atom molecule with the external electromagnetic field. We now consider an electromagnetic wave with an angular frequency ω_0:

$$\vec{E} = \vec{E}_0 e^{i\omega_0 t} + \vec{E}_0 e^{-i\omega_0 t} \tag{2.10}$$

This electromagnetic wave causes the oscillation of dipoles in the molecule, inducing a dipole moment:

$$\vec{p} = \bar{\bar{\alpha}}\vec{E} \tag{2.11}$$

where α represents the polarizability tensor, a quantity that depends both on the material and the frequency of the EM field. Since here only the linear scattering processes are considered, we neglect the nonlinear components of the tensor that become more prominent at stronger field strengths. The nonlinear components however become crucial in the nonlinear scattering processes such as stimulated Raman scattering (SRS) and coherent anti-Stokes Raman scattering (CARS). We further assume that the polarization depends linearly on the electric field. The polarizability can then be expressed as a Taylor series, consisting of the static contribution and a component depending on the displacement:

$$\alpha = \alpha_0 + \frac{\mathrm{d}\alpha}{\mathrm{d}q} q \tag{2.12}$$

Since the displacement is relatively small compared to the equilibrium position, we only use the first order Taylor expansion [10]. We can now

write the polarizability as:

$$\vec{p} = \alpha_0 \vec{E}_0 e^{-i\omega_0 t} + \frac{\mathrm{d}\alpha}{\mathrm{d}q} q \vec{E}_0 e^{-i(\omega_0 - \omega_S)t} + \frac{\mathrm{d}\alpha}{\mathrm{d}q} q \vec{E}_0 e^{-i(\omega_0 + \omega_S)t} \tag{2.13}$$

The induced dipole moment therefore consists of three components:

$$\vec{p} = \vec{p}_{\omega_0} + \vec{p}_{(\omega_0 - \omega_S)} + \vec{p}_{(\omega_0 + \omega_S)} \tag{2.14}$$

where the term $\vec{p}_{\omega_0}$ represents the elastic scattering, where the dipole oscillates at the frequency ω_0, and eventually reemits light at the same frequency. This process is called Rayleigh scattering and is the predominant scattering process of light in matter. The other two terms represent the inelastic scattering process, where the molecule radiates light at a frequency that is shifted from the incident frequency ω_0 by the vibrational frequency of the molecule ω_S. If the light is radiated at the frequency $\omega_0 - \omega_S$ we call this Stokes scattering, and the anti-Stokes scattering occurs at the frequency $\omega_0 + \omega_S$.

For more complex molecules with multiple vibrational frequencies, Eq. 2.13 can be extended to:

$$\vec{p} = \alpha_0 \vec{E}_0 e^{-i\omega_0 t} + E_0 \sum_j [\frac{\mathrm{d}\alpha}{\mathrm{d}q_j} q_j e^{-i(\omega_0 - \omega_S)t} + \frac{\mathrm{d}\alpha}{\mathrm{d}q_j} q_j e^{-i(\omega_0 + \omega_S)t}] \tag{2.15}$$

The complex molecules thus have multiple vibrational frequencies. For example, in the case of a molecule of CO_2 three different vibrational modes are present, each with its own characteristic vibrational frequency (Figure 2.5). The modes ν_1, ν_2 and ν_3 correspond to the vibrational modes with increasing vibrational energy.

The average radiated power of an oscillating electric dipole, induced in a molecule by an electric field of frequency ω_d, is given by:

$$P_d = \frac{|p_d|^2 \omega_d^4}{12\pi\epsilon_0 c^3} \tag{2.16}$$

where $|p_d|$ can be obtained from the Eq. 2.15:

$$|p_d| = \frac{\mathrm{d}\alpha}{\mathrm{d}q_j} q_j \vec{E}_0 \tag{2.17}$$

$|p_d|$ should be non-equal to zero so that the vibrational mode is Raman active, therefore:

$$\frac{\mathrm{d}\alpha}{\mathrm{d}q_j} q_j \neq 0 \tag{2.18}$$

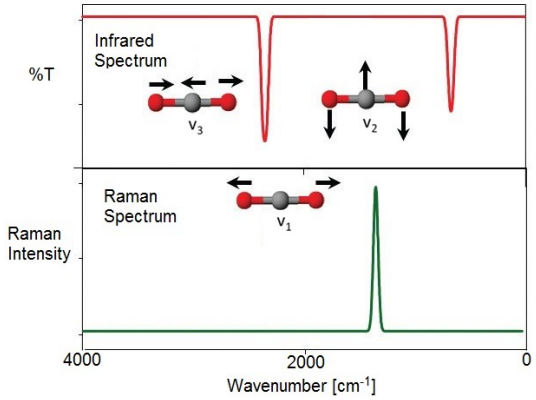

Figure 2.5: Vibrational modes of a molecule of carbon dioxide CO_2 and their corresponding IR and Raman spectral peaks. [19].

The induced displacement of the atoms around their equilibrium position must thus lead to a change in polarizability for the Raman mode to be active. In the previously mentioned example of the three vibrational modes of a CO_2 molecule, only the vibrations in mode ν_1 change the polarizability of the molecule, therefore making the mode Raman active. On the other hand, both ν_2 and ν_3 are Raman inactive modes (see Figure 2.5).

The activity of a Raman mode will depend on the symmetry of the molecule. Especially for the more complex molecules, it becomes harder to predict whether a specific vibrational mode will be Raman active or not. For this thesis, it is important to note that the vibrational mode can become Raman (in)active when a molecule gets bound to the surface of a substrate, as is often the case in surface-enhanced Raman spectroscopy (SERS).

Lastly, let's take a look at the strength of the Raman power scattered by a Raman active vibrational mode. The scattered Raman power per unit of solid angle can be expressed as a function of the irradiance I of an incident field:

$$P_S = \sigma I \tag{2.19}$$

Here, σ is the Raman cross section, a molecular property with typical values of 10^{-33} to 10^{-35} m^2 per steradian per molecule. The irradiance of the incident field can be written as $I = \frac{1}{2}c\epsilon_0|E|^2$ with the unit W/m^2. The intensity of the scattered Raman light is thus:

$$P_S = \frac{\pi^2 \alpha_{tr}^2}{\epsilon_0^2 \lambda_d^4} I = \sigma I \tag{2.20}$$

Here σ is the Raman cross section, and α_{tr} the general transition polarizability. The Raman cross section depends on the wavelength of the incident light as $\sigma \propto \frac{1}{\lambda^4}$, meaning that shorter wavelengths of the incident light evoke a stronger Raman response in the molecule. Using lower incident wavelengths can on the other hand have some other adverse consequences, discussed in more details in the previous section. In the next section we will see how we can increase the inherently weak Raman signal with Surface-Enhanced Raman Spectroscopy (SERS).

2.3 Surface enhanced Raman spectroscopy

Surface enhanced Raman spectroscopy (SERS) relies on the enhancement of the Raman signal of the analyte molecules in close proximity to the surface of metallic nanostructures. In these metallic structures, the localized surface plasmons can be optically excited, creating a strong electric field close to their surface, which can be used to enhance the inherently weak Raman signals. In this section, we will take a brief look at the theory of plasmon physics and show how the localized surface plasmons enable the enhancement of the Raman signal close to the surface of metallic nanoparticles in SERS. In the end, we will summarize the most commonly used SERS substrates.

2.3.1 Plasmon physics

Surface enhanced Raman spectroscopy relies on localized surface plasmons to enhance the intrinsically weak Raman signals. Before we take a look at the theory of the plasmon physics, we first define the terminology.

Plasmon is the quantized oscillation of the electron density in a metal.
Photon is a quantum particle representing electromagnetic field oscillations.
Polariton is a photon coupled to an electric dipole in an optically responsive medium. Often when talking about polaritons, we limit ourselves to photons in media with a strong optical response, i.e. metals.
Plasmon-Polariton (PP) is the quasi-particle related to the mixed photon-plasmon modes generated by an electromagnetic wave in a metal.
Surface Plasmon-Polariton (SPP) is the mixed state of a charge density wave (plasmon) and an electromagnetic wave (photon) at a metal-dielectric interface.

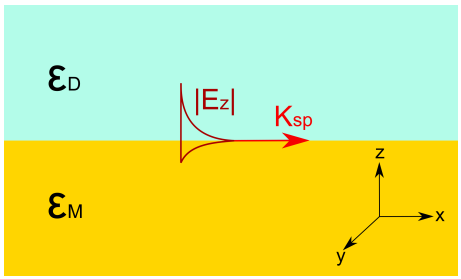

Figure 2.6: The schematic representation of the field of a surface plasmon polariton (SPP) at the interface of a metal and dielectric. ϵ_M and ϵ_D represent the permittivity of the metal and the dielectric respectively.

Localized Surface Plasmon-Polariton (LSPP, LSP) is a surface plasmon confined in three dimensions. It is often abbreviated as localized surface plasmon (LSP).

We start with a metal-dielectric interface shown in Figure 2.6.ϵ_M and ϵ_D are the dielectric constants of the metal and the dielectric respectively. The plasmon mode propagates along the interface so that the propagation constant of the surface plasmon K_{sp} is oriented along the x direction. The dispersion relation for a TM polarized surface plasmon mode (E_x, 0, E_z) and (0,H_y,0) is given by:

$$K_{sp}(\omega) = \frac{\omega}{c}\sqrt{\frac{\epsilon_D \epsilon_M}{\epsilon_D + \epsilon_M}} \tag{2.21}$$

Using the Drude theory, the permitivity of the metal with free electrons which are not bound to a particular nucleus can be written as [20]:

$$\epsilon_M(\omega) = 1 - \frac{\omega_p^2}{\omega^2 + i\omega\gamma} \tag{2.22}$$

Here ω_P is the bulk plasma frequency of the metal and γ a measure for the friction experienced by the electrons during their motion in the metal. The plasma frequency ω_p can be expressed as:

$$\omega_p^2 = \frac{n_e e^2}{\epsilon_o m_e} \tag{2.23}$$

where e is the electron charge, $\mathrm{m_e}$ its effective mass and $\mathrm{n_e}$ its density.

Next, we derive the conditions necessary for a metal-dielectric interface to exhibit the plasmonic properties. Here we assume a perfectly free electrons with γ = 0. The dispersion relation in air ($\epsilon_D = 1$) is therefore given

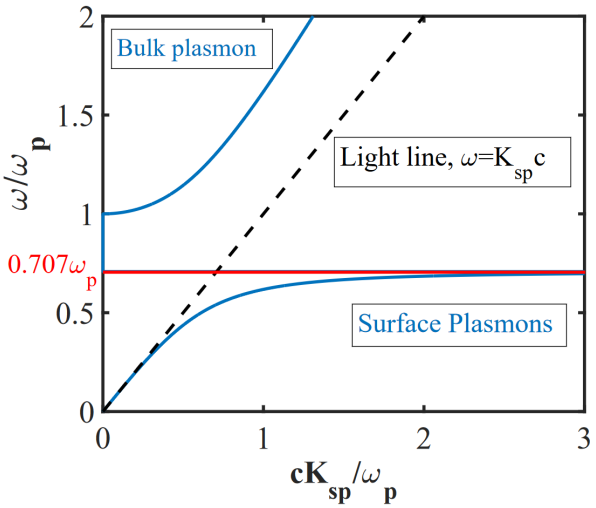

Figure 2.7: Dispersion relation of a SPP on an air-metal interface for a Drude metal. [21]

as:

$$K_{sp}(\omega) = \frac{\omega}{c}\sqrt{\frac{1-\frac{\omega_p^2}{\omega^2}}{2-\frac{\omega_p^2}{\omega^2}}} \tag{2.24}$$

There are two types of solutions to Eq.2.24, as plotted in Figure 2.7. For $0 < \omega < 0.707\omega_p$, the solution is a **surface plasmon** mode. Here, the frequency at $0.707\omega_p$ is the classical surface plasmon frequency for a metal-air system. The other solution for the frequency range of $\omega > \omega_p$ corresponds to the **bulk plasmon** mode. There is no solution that exists for the frequencies in the range $0.707\omega_p < \omega < \omega_p$.

The field decay length of the surface plasmon polariton L_i is inversely proportional to K_i:

$$L_i \propto \frac{c}{\omega}\sqrt{\frac{\epsilon_D + \epsilon_M}{\epsilon_i^2}} \tag{2.25}$$

Here, i can denote either the dielectric (D) or the metal (M). The dielectric constant of the metal is typically much larger than the dielectric constant of the dielectric, namely $\epsilon_M > \epsilon_D$. The L_M is therefore shorter as compared to the L_D. As an example, at a gold-air interface, L_{gold} = 31 nm and L_{air} = 280 nm. This means that the field in the metal next to the metal-dielectric interface is highly concentrated [22].

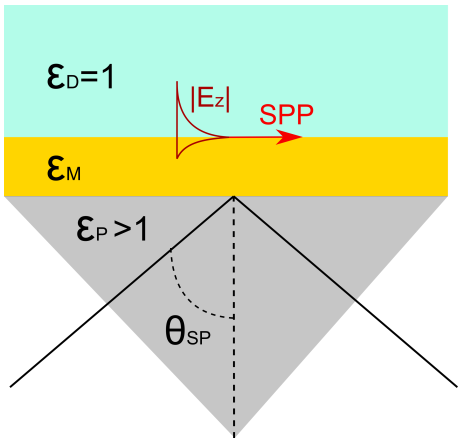

Figure 2.8: Kretschmann configuration uses a glass prism coated with a thin metal layer to excite SPPs at the metal-air interface.

From Figure 2.7 we see that the light line never crosses K_{sp}, which means that the light hitting a metal-dielectric interface at an arbitrary angle will not couple to the surface plasmon. A prism coupler [23] or periodic corrugation [24] is needed to couple the light to the metal-dielectric interface. In the so-called Kretschmann configuration, a prism with a dielectric permittivity ϵ_P is used to excite the surface plasmon. As shown in Figure 2.8, one facet of a prism is coated with a thin metal layer. The metal-dielectric facet is then illuminated at an angle greater than the total international reflection angle. The light is coupled to SPP when the in-plane component of the wave vector in the prism matches with K_{sp} of the air-metal interface:

$$\frac{\omega}{c}\sqrt{\epsilon_P}sin(\theta_{SP}) = K_{sp} \tag{2.26}$$

At θ_{SP}, we therefore observe a sharp minimum in the intensity of the reflected light. θ_{SP} allows the monitoring of ultra-thin films grown on the metal interface due to its high sensitivity to the variations in the refractive index of the surface. This phenomenon is called surface plasmon resonance (SPR) sensing [25, 26]. Similarly, biolayers on the gold surface can be monitored using the reflection measurements [27, 28].

We have seen that surface plasmons are propagating electromagnetic waves coupled to the electron plasma at the metal-dielectric interface. Now, we will take a closer look at the **localized surface plasmon modes (LSPP)**. LSPPs are non-propagating modes, which occur when a sub-wavelength conductive nanoparticle interacts with the oscillating electromagnetic field.

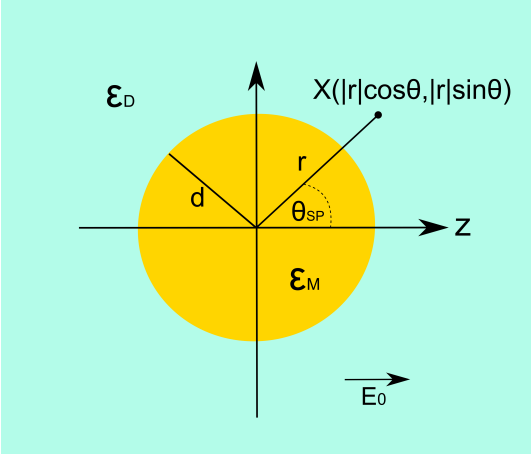

Figure 2.9: Schematic representation of a metallic nanosphere in a dielectric medium with permittivity ϵ_D. Nanosphere experiences a static electric field E_0.

Due to the spatially confined surface of the particle (for example a metallic nanosphere), a restoring force is applied on the electrons, which leads to a resonance behaviour named localized surface plasmon resonance (LSPR). In resonance condition, the particles exhibit bright colors both in transmitted and reflected light, due to resonantly enhanced absorption and scattering cross sections. For gold and silver particles, LSPR occurs in the visible wavelength, a phenomenon that was famously used in the staining of glass windows.

For an analytical treatment, we examine the (simplest) spherical geometry of the conducting nanoparticle. The nanosphere has a radius d $<<$ λ. It is further assumed that the nanoparticle is immersed in a medium with the permittivity ϵ_D and which has no dispersion and no losses. Figure 2.9 schematically shows the examined geometry. Here, a constant phase of EM waves across the nanoparticle is assumed. Therefore, a quasi-static approximation can be applied to extract the spatial field distribution. When $\nabla \times E$ = 0, the electric field can be written as the gradient of electric potential φ:

$$E = -\nabla\varphi \tag{2.27}$$

Using Gauss's law, we can write:

$$\nabla \cdot E = \nabla \cdot (-\nabla\varphi) = -\nabla^2\varphi = 0 \tag{2.28}$$

With the azimuthal symmetry of the problem, the general solution of Eq. 2.28

will be [17]:

$$\varphi(r,\theta) = \sum_{n=0}^{\infty}[A_n r^n + B_n r^{-(n+1)}]P_n(cos\theta) \tag{2.29}$$

where θ is the angle between the position vector r at point x (rsinθ,rcosθ) and the z-axis, and $P_n$cosθ are the Legendre Polynomials of the order n. Since φ(r,θ) must remain finite at the origin, Eq. 2.29 can be split into two solutions, one inside and one outside the sphere. The solution inside the sphere is therefore:

$$\varphi_{in}(r,\theta) = \sum_{n=0}^{\infty} A_n r^n P_n(cos\theta) \quad for \quad r < d \tag{2.30}$$

and solution outside the sphere:

$$\varphi_{out}(r,\theta) = \sum_{n=0}^{\infty}[B_n r^n + C_n r^{-(n+1)}]P_n(cos\theta) \quad for \quad r > d \tag{2.31}$$

The coefficients A_n, B_n and C_n can be determined by applying the boundary conditions at r $\rightarrow \infty$ and r = d. At r $\rightarrow \infty$, $B_1 = -E_0$ and B_n = 0 for n$\neq$1. At r = d, the tangential components of the electric field demand:

$$\frac{1}{d}\frac{\partial\varphi_{in}}{\partial\theta} = \frac{1}{d}\frac{\partial\varphi_{out}}{\partial\theta} \tag{2.32}$$

The continuity of the normal components of the displacement field then requires:

$$\epsilon_o\epsilon_M\frac{\partial\varphi_{in}}{\partial r} = \epsilon_o\epsilon_D\frac{\partial\varphi_{out}}{\partial r} \tag{2.33}$$

By combining Eq. 2.30 and Eq. 2.32, as well as Eq. 2.31 and Eq. 2.33, remaining coefficients can be computed as $A_n = C_n = 0$ for n $\neq$ 1. For n=1 (dipole mode), φ is thus given as [17] [29]:

$$\varphi_{in}(r,\theta) = -\frac{3\epsilon_D}{\epsilon_M + 2\epsilon_D}E_o r cos\theta \tag{2.34}$$

$$\varphi_{out}(r,\theta) = -E_o r cos\theta + \frac{\epsilon_M - \epsilon_D}{\epsilon_M + 2\epsilon_D}E_o d^3\frac{cos\theta}{r^2} \tag{2.35}$$

In the derivation of the above equations the differential properties of Legendre function mentioned in [30] are used. By applying Eq. 2.27, 2.34

and 2.35, it can be shown that both the internal φ_{in} and external dipolar fields φ_{out} show a resonance effect for the following condition:

$$\mathbb{R}(\epsilon_M) = -2\epsilon_D \tag{2.36}$$

This field enhancement at the plasmon resonance allows many applications in sensing [31] and modulation [32]. The resonance mode at ω_{LSP} is called dipole localized surface plasmon mode of a nanoparticle. For a metal whose permittivity follows the Drude model, this condition is satisfied at the frequency ω_{LSP}:

$$\omega_{LSP} = \omega_P \sqrt{\frac{1}{1+2\epsilon_D}} \tag{2.37}$$

Eq. 2.37 shows that the resonance depends on the dielectric permittivity and experiences a red shift with increased ϵ_D. ω_{LSP} also depends on the size of the nanoparticle, where the extinction cross section scales with the volume of sphere [20]. The nanoparticle size can therefore be engineered to have the resonance in the wavelength range of our interest [33], which is especially interesting for surface enhanced Raman spectroscopy. An example of resonance wavelengths of different plasmonic structures of varying dimensions are shown in Figure 2.10. Note that the quasi-static approximation that we used above is only valid for small spherical particles. For larger particles with more complex geometries [34], the surface plasmon frequency ω_{LSP} needs to be calculated numerically by solving the Maxwell equations. As seen in Figure 2.10, generally speaking the increasing size of plasmonic antennas causes a red shift in the localized surface plasmon frequency, as well as an increased FWHM.

Lastly, we will show that the dipole mode of a nanosphere can be excited efficiently at ω_{LSP} and estimate the field enhancement provided by a metallic nanoparticle [29]. Here, an isolated gold particle is considered, meaning that only the dipole mode can be coupled to the external EM radiation. Higher order modes cannot be excited because of their vanishing dipole moments [29].

We can express the total field enhancement $|E_o|$ of a dipole mode normalized to an electric field $|E_G|$ of a tightly confined Gaussian beam as:

$$\begin{aligned} F &= \frac{|E_o|}{|E_G|}\left(\frac{d}{d+x}\right)^3 \\ &= \frac{\sqrt{2}}{\sqrt{[Q^{-1}+2\chi_d^3/3\epsilon_D]^2+\delta^2}}\left(\frac{\chi_d}{\chi_d+\chi}\right)^3 \end{aligned} \tag{2.38}$$

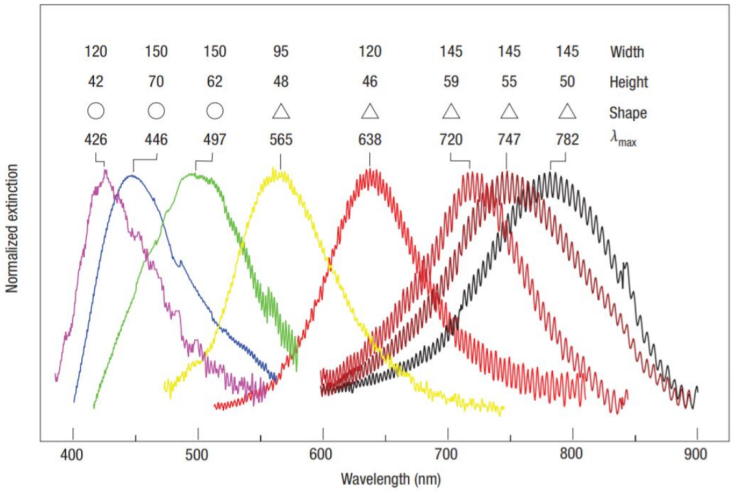

Figure 2.10: The geometrical dependence of the plasmon resonance for silver nanoprisms and nanodiscs. [34]

Here Q is the quality factor and given by Q = ω/γ, where γ is the non-radiative decay rate. δ is the normalized excitation detuning, χ and χ_d are the normalized radius and the distance from the sphere, namely $\chi_d = 2\pi d/\lambda_d$.

Gold nanoparticles have a Q in the order of 10, and thus offer the normalized field enhancement F of approximately 14. Quality factors of different metal-air nanoparticles are shown in Figure 2.11. Note that Q is larger when the non-radiative decay rate γ is small. Gold and silver both have a large quality factor in the NIR wavelength range. However, due to the quick oxidation of silver in the air, the gold is usually preferred for sensing applications. At visible wavelength, silver is the best performing plasmonic material, whereas aluminum has high Q values at UV wavelengths. A complete overview of the plasmonic properties of these materials is available in [35].

2.3.2 SERS enhancement mechanism

When a molecule is brought close to the surface of a metallic nanoparticle, which is resonant in the selected wavelength region, the enhanced field around the nanoparticle will excite the molecule. Its induced dipole moment is then given by:

$$p = \alpha_r E F(\lambda_P) E_0 \tag{2.39}$$

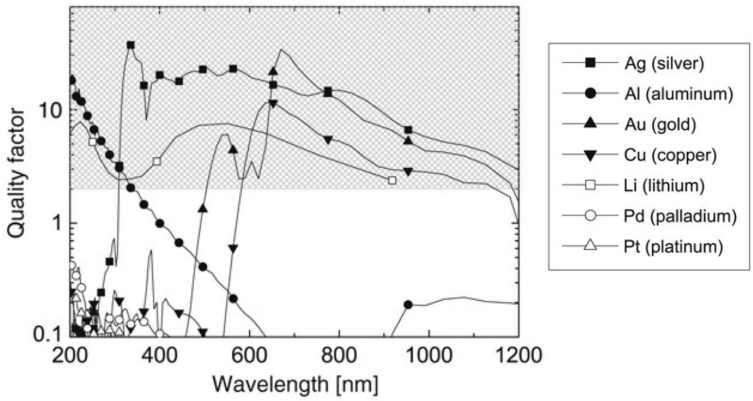

Figure 2.11: Quality factors of metal-air nanoparticles for different metals. The shaded area of interest for many plasmonic applications. [12]

where α_R is the general polarizability, EF(λ_P) the field enhancement at the pump wavelength λ_P and E_0 the incident electric field. The induced dipole of the molecule will generate an electric field E_S at a given Stokes wavelength λ_S. The Stokes electric field in itself can also be enhanced by the nanoparticle:

$$E_S = EF(\lambda_S)(\alpha_r EF(\lambda_P)E_0) \tag{2.40}$$

Here EF(λ_S) is the field enhancement at the Stokes wavelength. The overall intensity I_{SERS} of the scattered SERS light will then scale as:

$$I_{SERS} \propto |E_S|^2 \propto \alpha_r^2 EF(\lambda_P)^2 EF(\lambda_S)^2 I_0 \tag{2.41}$$

where I_0 is the incident intensity. We define the SERS enhancement factor EF as the ratio of the Raman scattered intensity in the presence of the metal nanoparticle over its value in the absence of the particle:

$$EF = (\frac{\alpha_R}{\alpha_{R0}})^2 EF(\lambda_P)^2 EF(\lambda_S)^2 \tag{2.42}$$

Here, α_{R0} is the polarizability of the isolated molecule, and α_R the polarizability of the molecule adsorbed to the metal surface. When a molecule is adsorbed on the metal surface, α_R also contains contributions from the (chemical) interactions of the molecule with the metal, and may experience an enhancement of up to a 100-fold compared to an isolated molecule [20]. This effect is called the chemical SERS enhancement [36].

On the other hand, we have the electromagnetic SERS enhancement that depends on the field enhancement. Since the difference between pump and

Stokes frequencies is quite small as compared to FWHM of the LSP, i.e. $\nu_p = \nu_s = \nu$, EF can be approximated as:

$$EF = (\frac{\alpha_R}{\alpha_{R0}})^2 EF(\lambda)^4 \tag{2.43}$$

The electromagnetic SERS enhancement therefore scales with the fourth power of the field enhancement [36]. The electromagnetic SERS enhancement typically lies in the range of 10^5-10^7 and is the main contribution to the SERS enhancement [6]. Note that however SERS itself is a linear optical process, since it scales with the first power of I_0 (Eg. 2.41). Figure 2.12 schematically summarizes the main differences between the spontaneous and surface enhanced Raman scattering.

2.3.3 SERS substrates

Colloidal metal nanoparticles were the first SERS substrates. They can be fabricated using either wet chemical methods such as reduction of silver or gold ions in a solution [37], or via a mechanical process like laser ablation [38]. They can be used in solution or an additional fabrication step can be performed where the metallic nanoparticles are immobilized on the secondary substrate [39]. The colloidal metal nanoparticles enable strong SERS enhancements, yet their fabrication methods offer only limited control of their geometry, size and position, consequently affecting the reproducibility of SERS measurements [40].

Conversely, a variety of SERS substrates has been developed using top-down fabrication techniques such as nanosphere lithography [41–44], and deep-UV [45] and electron beam lithography [46, 47]. These techniques enable precise control of the shape and position of the nanostructures, which allows more tunable and reproducible SERS enhancements [40]. Among the top-down fabricated SERS substrates, the gold nanodomes offer one of the highest SERS enhancements [48, 49]. Their fabrication is simple and scalable, while also ensuring better control of the hotspot size and enhancement factor as compared to colloidal approaches. In this work, gold nanodomes were exclusively used as the free-space SERS substrate.

Additionally, novel techniques for the more efficient collection of Raman signals have recently emerged as alternatives to the conventional Raman microscope, such as hollow-core photonic crystal fibers [50] and nanophotonic waveguides on photonic integrated circuits (PICs). The waveguide-based

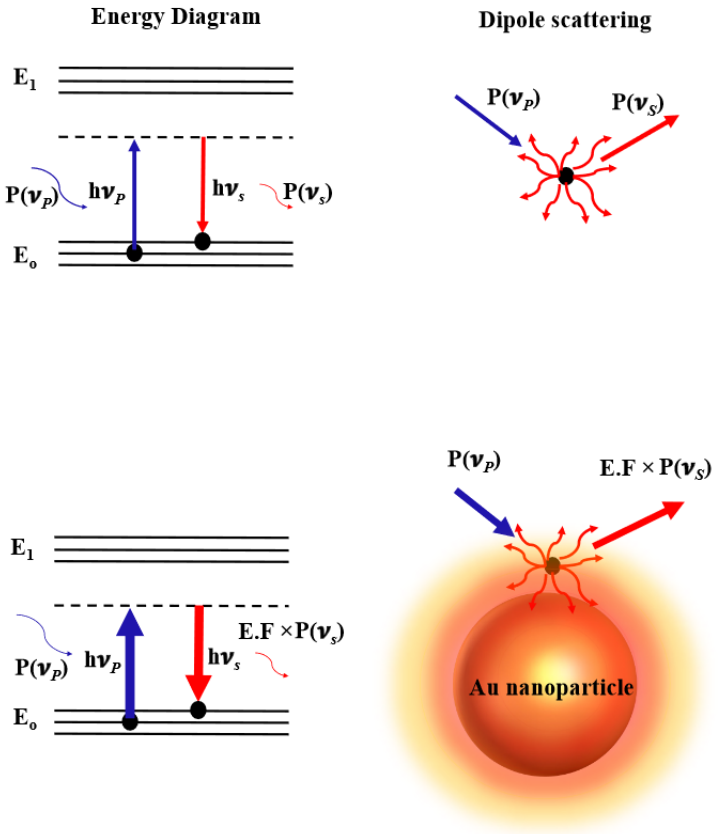

Figure 2.12: Comparison of spontaneous (top) and surface enhanced (bottom) Raman scattering. Spontaneous Raman signal is enhanced by the high field enhancement of the gold nanoparticle at both pump ν_P and Stokes ν_S frequencies. SERS can be additionally enhanced by the change of the polarizability of the molecule in the vicinity of the metal surface. [21]

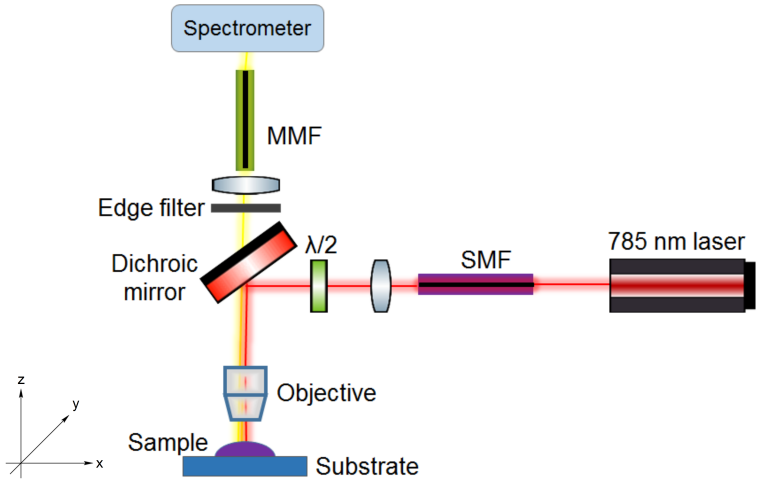

Figure 2.13: Schematic of the confocal Raman microscope WITec Alpha 300 R+.

SERS substrates and their advantages are discussed in more detail in Section 2.5.

2.4 Confocal Raman microscope

The sensitivity and the spectral resolution of the Raman setups used to acquire the Raman spectra has improved significantly in the last decades. The basic principle of every Raman setup includes the laser light incident on the sample, whereas the scattered light is collected under a 90° or 180° angle. An edge filter is then used to remove the Rayleigh scattered light and the Raman light is sent to a spectrometer where the Raman spectrum is acquired.

In this thesis, confocal Raman microscope (WITec Alpha300 R+) was used to perform all the experiments. The schematic of the microscope is presented in Figure 2.13. In this section we will briefly describe the working of the conventional confocal Raman microscope and its components. We will also introduce its conversion efficiency that will allow us to compare it with the waveguide-based Raman platforms in the next section.

First, the light from the excitation laser is focused on the sample through an objective. The wavelength of the laser is crucial in the Raman experiments, since Raman scattering cross section scales with λ^{-4}. The advan-

tages and the disadvantages of using UV-VIS light compared to the near infrared (NIR) spectral region were already discussed in Section 2.1. We concluded that the excitation wavelengths around 800 nm are optimal in order to minimize the fluorescent background prevalent at lower wavelengths while avoiding the high absorption of water at higher wavelengths. In our experiments, the pump laser Toptica XTRA II 785 nm with a < 10 MHz linewidth and $<< 30$ GHz frequency drift is used. The laser light is fiber coupled to a single mode fiber (SMF) with a maximum output power of 150 mW through the fiber. A lens then collimates the output laser beam and a half-wave plate allows to rotate the linear polarization of the light. The incident light is then directed towards the sample using a dichroic mirror and an objective is used to focus the laser beam on the sample. The sample here can simply be the analyte, or the analyte on a SERS substrate in the case of SERS measurements. In Raman spectroscopy, the power of a few 100 mW is routinely used in order to maximize the amount of the Raman scattered light. In SERS experiments on the other hand, the laser power should be kept low (< 1 mW) in order to avoid excessively heating and thus destroying the analyte molecules due to the high power density in the local field enhancement and the absorption of the gold.

The microscope objective plays a crucial role in the excitation and collection of the Raman scattered light. The objective characteristics have to therefore be carefully chosen. The numerical aperture determines the size of the focal spot, whereas the combination of the pinhole and the magnification of the objective will influence the confocality of the measurement. The apochromatic objectives are usually corrected for equal focal points in the visible range, but the focal length may drift above 800 nm. Since all materials have some Raman background, the Raman spectra are usually acquired on the upright Raman microscope where the light doesn't have to pass through a cover slip. The objectives used in Raman microscope therefore typically don't require the cover slip correction. In our SERS measurements we use non-transparent SERS substrates, which also requires signal collection in the upright microscope configuration. Depending on the medium in which we want to acquire the spectra, i.e. air or water, we furthermore need to use an objective suitable for the chosen immersion medium. The list of objectives used in this thesis is summarized in Table 2.2.

After the scattered light is collected by the microscope objective, it passes through a dichroic mirror that already filters out some of the Rayleigh scattered light, letting the Raman scattered light pass through. The edge filter serves to remove any remaining Rayleigh light. The Raman scattered light is then collected by the confocal pinhole, which assures that only

$Objective$	NA	n_d	Ω	$\Omega/4\pi$
Nikon CFI Plan Fluor 10x $\infty/0.16$	0.3	1	0.29	2.3%
Zeiss W N-Achroplan/W 20x $\infty/0$	0.5	1.33	0.46	3.7%
Zeiss W Plan-Apochromat 63x $\infty/0$	1	1.33	2.14	17%
Zeiss EC Epiplan Neofluar 100x $\infty/0$	0.9	1	3.54	28%

Table 2.2: The list of microscope objectives used in this work, including their numerical aperture (NA), the refractive index of the medium n_d, the solid angle Ω and the fraction of the maximum solid angle $\Omega/4\pi$.

the light scattered in the focal plane is collected, therefore reducing the Raman background signal. In the Witec confocal Raman microscope used in this work, a multimode fiber is used as a confocal pinhole, and then also guides the light to the input slit of the spectrometer. The use of a multimode fiber however means that the pinhole diameter can't be (easily) adjusted. The multimode fiber furthermore generates a ripple on the acquired Raman spectrum, possibly due to the interference between the different modes. This problem could be solved by using a single mode fiber, but this would also result in a low collected Raman signal. In practice, this problem is mitigated by shaking the collection fiber with the frequency of $20 - 100$ Hz, which temporally averages the beam profile, thus revealing small Raman peaks on the large Raman background.

The Raman scattered light then passes a diffraction grating and is imaged on a CCD camera. The spectral resolution of the spectrometer depends on the input slit, size of the spectrometer and periodicity of the grating. In our particular case, the easiest way to increase the spectral resolution is to use a grating with different periodicity. Our system has two different gratings - the 300 and 600 l/mm. The 300 l/mm grating covers the inverse frequency span of 3400 cm^{-1} and has a spectral resolution of 2 cm^{-1}. On the other hand, the 600 l/mm grating provides a better spectral resolution of 1.5 cm^{-1} with the inverse frequency span of 1800 cm^{-1}. Given that most of the organic molecules present characteristic peaks at the Raman shifts in the 600-1800 cm^{-1} and the 2600-2900 cm^{-1} region, the 600 l/mm grating is always used in this work.

The spectra are finally acquired on the CCD camera. Since the Raman signals are weak, the Raman spectrum is highly influenced by the thermal noise at the room temperature. The CCD camera (Andor iDus401 BR-DD) is therefore cooled to $-70°$C to ensure a low dark current. For the

lower temperatures and limited integration times, the readout noise becomes dominant. As the total readout- and dark-noise fluctuations scale linearly with the number of pixels, reading less pixels per spectral point helps to reduce it.

In the end, the amount of Raman power that can be captured by such a microscopy system is calculated. Later, this can be used as a metric to compare the Raman microscope with the waveguide-based Raman platforms. For the diffraction limited confocal microscope only the analyte molecules located in the focal volume will contribute significantly to the Raman signal strength. The collection efficiency ν_{col} can therefore be expressed as the ratio of the collected Raman power P_{col} compared to the pump power P_p:

$$\eta_{col} = \frac{P_{col}}{P_p} = \Omega \rho \sigma b \tag{2.44}$$

where Ω is the solid angle of the objective, ρ the concentration of the analyte molecule and σ its Raman cross section. b represents the depth of focus [51]. The solid angle Ω can be expressed as:

$$\Omega = 2\pi(1 - cos\theta) = 2\pi \left(1 - \sqrt{1 - \left(\frac{NA}{n}\right)^2}\right) \approx \pi \left(\frac{NA}{n}\right)^2 \tag{2.45}$$

where NA is the numerical aperture of the objective and n the refractive index of the immersion medium. For a Gaussian beam the numerical aperture NA and the depth of focus b can be expressed as:

$$NA = \frac{\lambda_p}{\pi w_0} \tag{2.46}$$

$$b = \frac{2\pi n w_0^2}{\lambda_p} \tag{2.47}$$

where w_0 is the beam waist and λ_p the excitation laser wavelength. The collection efficiency can thus be expressed as:

$$\eta_{col} = 2\rho\sigma \frac{\lambda_p}{n} \tag{2.48}$$

For a diffraction limited system, the collection efficiency depends solely on the excitation wavelength and the analyte properties, and can't be improved by changing the optics of the setup. In this regard, the waveguide-based Raman platforms have an advantage compared to the Raman microscope,

since their collected Raman signal scales proportionally with the length of the waveguide, as further discussed in Section 2.5.2. In the next section, the motivation for the transition to integrated approach to Raman is presented, along with the overview of the waveguide-based Raman and SERS platforms.

2.5 Waveguide-based Raman and SERS platforms

2.5.1 Integrated approach to Raman spectroscopy

Widely used spectroscopic techniques, including Raman spectroscopy, typically rely on bulky and expensive instrumentation, which largely limits their use to the laboratory environments. In recent years, there has been a push for portable miniaturized devices, which can perform sensitive and accurate spectroscopic detection. An integrated photonics approach can offer the solution by bringing various free-space optical components to a single chip. The integration leads to devices that are robust, cheap, mass-reproducible and reliable, and additionally enable multiplexing and parallelization [1].

On a photonic chip, the light is guided by optical waveguides consisting of a high refractive index core surrounded by the lower refractive index cladding material. Other components, such as the light source and the spectrometer can also be miniaturized and integrated on the photonic chip, so that the whole functionality of the free-space setup can be translated on a small chip. This concept is shown schematically in Figure 2.14 for the case of Raman microscope. Several papers were published in the last years that explore how to implement all the functionalities of the Raman microscope on an integrated photonic chip, including a III/V integrated laser [52], integrated filters [53], a waveguide collection region [54] and an on-chip spectrometer [55]. Further effort is however still needed to ensure the compatibility of all the different components and integrate them on the same photonic chip.

In the past decades, several material platforms have been developed for photonic integration, of which silicon photonics is widely used in various industrial applications of photonic integrated circuits. The principal component in silicon photonics is the silicon-on-insulator (SOI) waveguide, consisting of a silicon (Si) core on a silicon oxide (SiO_2) substrate. Because of the high index contrast, the light can be tightly confined in a 450x220 nm core, which allows the dense integration of the optical components on

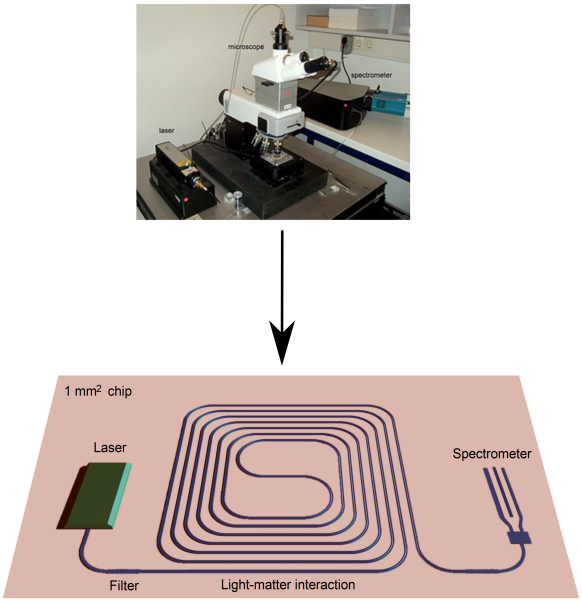

Figure 2.14: Conceptual representation of an integrated Raman system on a nanophotonic chip, where the laser source, the filters, the Raman signal excitation and collection, and the spectrometer are all integrated on a small photonic chip.

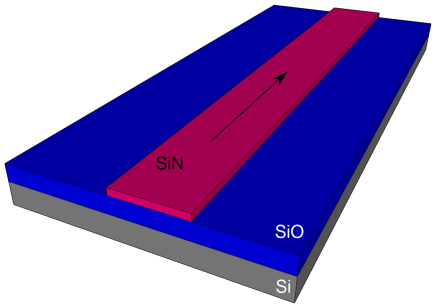

Figure 2.15: Schematic view of a Si_3N_4 strip waveguide. The light (represented by the arrow) is guided in the Si_3N_4 core with the higher refracting index that the surrounding material. The typical single mode waveguide has the height of 220 nm and the width of 700 nm.

the photonic chip. Because of the transparency of silicon in the wavelength range 1300-1600 nm, SOI platform is extremely suitable for telecom applications, but can also be used in sensing. When the light is confined in the Si core, part of the electromagnetic field extends out of the core. This so-called evanescent field can sensitively detect changes in the surrounding medium, which allowed the development of the absorption [56] and the refractive index sensors [57]. One of the main advantages of the SOI platform is also the compatibility with the CMOS-fabrication used for electronic chips, which is crucial for any potential industrial application.

Silicon absorbs light with wavelengths shorter than 1.1 μm, which prevents the use of silicon waveguides in the visible region. As a transparent alternative at these wavelengths, the silicon nitride (Si_3N_4) platform was developed. Since the intensity of the Raman scattered light scales with λ^{-4}, excitation at lower wavelengths is preferred. Si_3N_4 platform is thus more suitable for waveguide-based Raman applications, while still having the advantage of being produced on a wafer-scale in the CMOS-fab. In the next sections, we take a look at how the Si_3N_4 platform can be used for a waveguide-based detection of Raman and SERS signals.

2.5.2 Nanophotonic waveguide enhanced Raman spectroscopy

In nanophotonic waveguide enhanced Raman spectroscopy (NWERS), the waveguide-guided light can be used to excite and collect the Raman scattered signal from molecules in the close vicinity of the waveguide. The NWERS was first demonstrated in 1974 on micron-sized thin films of methylmethacrylate coated on a glass substrate [58]. Since then, several papers demonstrated NWERS on a variety of slab structures [59–63]. However, the slab-based structures provide limited modal overlap and can't be integrated with other photonic functionalities. The development of better fabrication techniques in the last decade led to the fabrication of low-loss and compact waveguide structures like strip and slot waveguides. Silicon nitride and titanium oxide waveguides were used to demonstrate the bulk sensing of the analyte [54, 64], and the waveguides covered with special absorbing coating were used to detect analytes in the gas phase [65]. NWERS also enables the measurement of more complex biological analytes such as DNA [66] and hemoglobin [67], that are directly bound to the waveguide surface.

In this thesis, the focus lies on the Si_3N_4 platform, which provides several advantages for Raman and SERS sensing, as discussed in the previous section. We build on the PhD works of A. Dhakal [68], F. Peyskens [69], P.

Wuytens [7] and A. Raza [21], where the Si_3N_4 waveguide-based Raman and SERS detection of different analytes have been established.

Si_3N_4 waveguide is a basic building block for all waveguide-based Raman and SERS applications. There, the light is guided in the Si_3N_4 waveguide. Using the guided light for the excitation and collection of the Raman spectra can increase the total collected Raman power by a factor of 10-1000 compared to the free-space excitation [66]. The enhancement stems partly from an increased excitation of the analyte molecules due to the strong evanescent field of the waveguide. The waveguide also collects the Raman scattered light more efficiently than the microscope objective in the free-space Raman microscope. The collected Raman signal furthermore accumulates along the whole length of the waveguide. In principle, the Raman signal increases linearly with the waveguide length [54], but is in practice limited to a few centimeters due to the propagation loss in the waveguide (1-5 dB/cm).

The typical decay lengths for SERS are < 10 nm, limiting its use to small molecules, whereas the confocal Raman microscopy can be used for objects > 500 nm, such as the cell. The evanescent field used to excite the Raman signal in the Si_3N_4 waveguides extends for 10-100 nm, which makes it a suitable technique for the detection of exosomes and large proteins, which can not be examined by the other two techniques.

The intrinsic problem to waveguide-based Raman and SERS applications is the Raman scattering from the waveguide core itself. This Raman background is always present and depends on the material used to fabricate the waveguide. An overview of the different material platforms and their background is presented in [70]. On our Si_3N_4 platform, the Si_3N_4 presents a broad shape of the background, which decreases at longer frequency shifts and exhibits a characteristic peak at 2330 cm^{-1} [71]. The background can however highly vary between different types of Si_3N_4, and even depending on the exact deposition parameters within the same Si_3N_4 type. The origin of the Raman background in NWERS has been analyzed in [72]. The strength of the Raman background increases with the waveguide length, so a compromise must always be made between maximizing the acquired Raman signal and minimizing the Raman background. The only inherent way to reduce the Raman background is to push the guided mode as much as possible out of the waveguide core into the analyte, for example using a TM mode in a thin strip waveguide [65] or the nanophotonic slotted waveguide (Figure 2.16) [54].

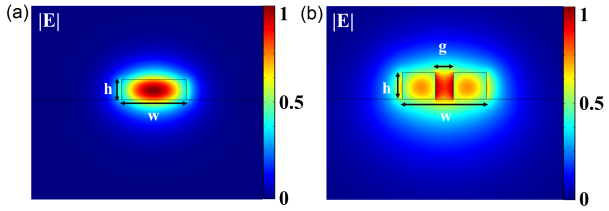

Figure 2.16: Comparison of the TE mode guided in the Si_3N_4 strip (a) and slot (b) waveguide. The TE mode in the slot waveguide is mainly guided outside the Si_3N_4 core, thereby reducing the Raman background signal. Typical waveguide dimensions are h = 220nm, w = 700 nm and g = 150 nm. [21].

2.5.3 Waveguide-based SERS platforms

Analogous to the waveguide-based detection of the Raman spectra, the on-chip SERS detection offers a promising alternative to the conventional Raman microscopy, enabling miniaturized chips for high-throughput SERS assays on low sampling volumes. First, photonic integrated circuits were only used to probe SERS signal from external, non-integrated metallic nanoparticles [73–75]. This approach however lacks the quantitative precision, since the coupling efficiency between the excitation laser light and the metallic nanoparticles can't be reliably and reproducibly assessed [76]. To address this issue, a novel SERS platform has been developed, where the SERS response of the integrated bowtie antennas is excited and collected by a single mode Si_3N_4 waveguide, shown in Figure 2.17(a) [77]. The bowtie antennas were developed to be resonant for the excitation wavelength of 785 nm, which is interesting also for the SERS detection of the biological molecules. This newly developed waveguide-based SERS platform was used for the detection of 4-nitrothiophenol, an organic molecule with a high Raman cross section. The SERS enhancement was however not high enough to measure the SERS spectra of the biological molecules with typically low Raman cross sections. Another disadvantage of the integrated bowties antennas is the use of the electron beam lithography in the fabrication process, which limits their potential use in the industrial applications.

The integrated gold nanotriangles depicted on Figure 2.17(b) enabled higher SERS enhancements compared to the integrated bowtie antennas [78]. They were additionally fabricated using nanosphere lithography on deep-UV patterned Si_3N_4 waveguides, in a process compatible with a potential large-scale manufacturing. The localized surface-plasmon resonance of these nanotriangles was again optimized for Raman excitation at 785 nm.

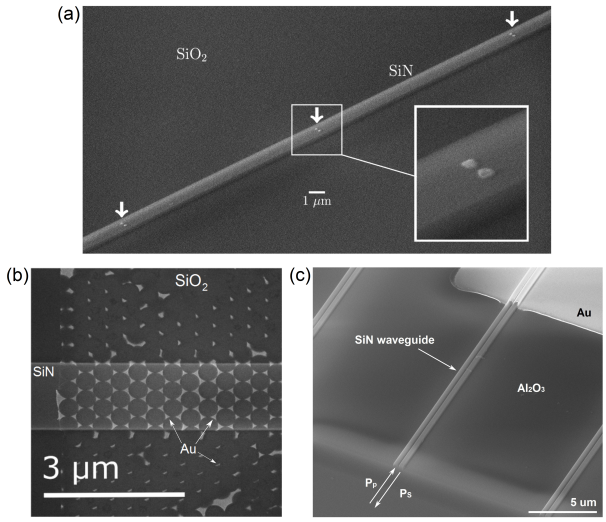

Figure 2.17: Waveguide-based SERS platforms. (a) Integrated bowtie antennas. [77]. (b) Integrated gold nanotriangles. [78]. (c) Nanoplasmonic slot waveguide.

Replacing the plasmonic antennas with a nanoplasmonic slot waveguide allowed to further increase the SERS enhancement of the waveguide-based SERS platforms [79]. Nanoplasmonic slot waveguides, shown in Figure 2.17(c), exhibit a strong field enhancement due to the highly confined propagating plasmon polariton gap mode. They moreover show a limited background thanks to the limited field overlap with the dielectric waveguide. In the fabrication, the atomic layer deposition (ALD) is used to create the nanometer-scale gaps needed for the large plasmonic enhancement, making the platform suitable for industrial applications. Compared to the integrated bowtie antennas and the integrated gold nanotriangles, the nanoplasmonic slot waveguide offers the non-resonant enhancement, meaning that the SERS enhancement doesn't depend on the excitation wavelength.

The SERS performance comparison of the different free-space SERS substrates is already difficult. It can among other depend on the definition of the enhancement factor, analyte, number of molecules, excitation wavelength and the optics used in the setup [80]. When comparing the free-space SERS substrates to the waveguide-based SERS platforms, the comparison gets even more complicated. In this thesis, we want to bring the SERS-based protease sensing from the free-space configuration to the waveguide-based SERS platform. It is therefore crucial to have a relevant assessment of

the performance of the waveguide-based SERS platforms, especially the nanoplasmonic slot waveguide used in our work. To critically examine that, the different platforms were compared based on the signal-to-noise ratio (SNR) and the signal-to-background ratio (SBG), as explained thoroughly in Chapter 5.

2.6 Conclusion

In this chapter, the origin of Raman scattering was presented, and Raman spectroscopy was compared to other commonly used spectroscopic techniques. Raman spectroscopy provides highly specific ”molecular fingerprints” of the molecules, yet Raman signals are inherently weak. To address that, Surface Enhanced Raman Spectroscopy (SERS) was developed, where Raman signal is enhanced close to the surface of metallic nanostructures. The conventional free-space Raman microscopy was described, followed by the motivation for the waveguide-based Raman and SERS detection. In the end, the recent developments in the on-chip Raman and SERS detection were summarized. In the next chapter, the proteases and their role in the human pathologies are described. The techniques used for the protease activity detection are assessed, and the motivation to use SERS for the protease activity sensing is explained.

3

Proteases and the detection of their activity

In this chapter, we will take a closer look at proteases and their various roles in the human body. As proteases are crucial in many different human diseases, they are important targets for the development of new inhibitory drugs. To identify such protease inhibitors that can be used as therapeutic drugs, there is a need for efficient methods to monitor protease activities. We will here review some of the techniques that were used in the past, and summarize the newest methods to monitor protease activities. Finally, we will examine SERS as a technique for protease activity monitoring, and evaluate its advantages and disadvantages over the other methods.

3.1 Proteases

3.1.1 What are proteases?

Proteases are enzymes that hydrolyze peptide bonds, thereby catalyzing the breakdown of proteins amongst others [81]. This hydrolysis reaction is shown in Figure 3.1. Here, a water molecule is used to break (hydrolyze)

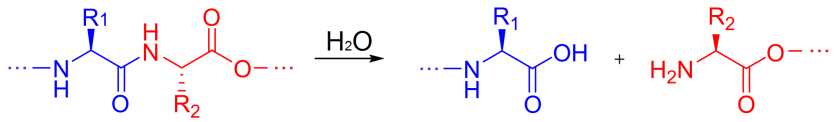

Figure 3.1: Proteases catalyze the hydrolysis of peptide bonds, effectively breaking down the peptide in smaller fragments. Adapted from [82].

the peptide bond that connects two adjacent amino acids.

In this hydrolysis reaction, a protease plays a role of a catalyst, which increases the reaction rate by lowering the activation energy [83]. The activation energy of a chemical reaction is the energy that must be provided to a chemical system in order to overcome the potential barrier between the reactants and the products, resulting in a chemical reaction. This principle is shown schematically in Figure 3.2. When a catalyst is present, the activation energy is lowered, thus decreasing the energy required to initiate the reaction.

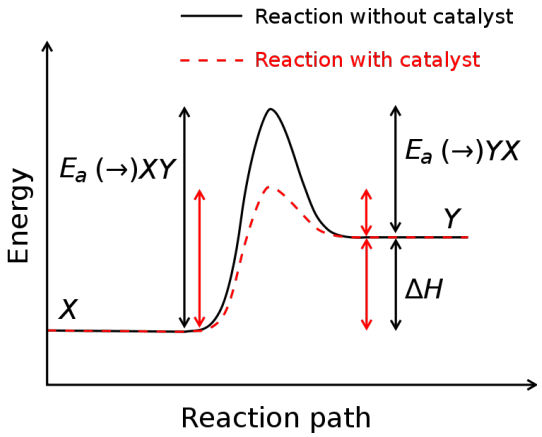

Figure 3.2: Energy diagram of a chemical reaction X→Y (black line). Sufficient activation energy E_a must be provided to the molecule X in order to reach the transition state (at the highest energy position) and be able to convert to Y. In the presence of a catalyst, for example a protease in the protein hydrolysis reaction, the activation energy is lowered, effectively speeding up the rate of the chemical reaction (red dashed line). [84]

A catalyst is therefore a substance that modifies the transition state, consequently lowering the activation energy of a chemical reaction and increasing its reaction rate. A subclass of catalysts are enzymes, which are thus proteinaceous catalysts. Enzymes can be assigned in six main groups

based on the nature of the chemical reaction they are catalyzing [85]:

- Oxidoreductases: catalyze oxidation/reduction reactions
- Transferases: transfer a functional group (e.g. a methyl or phosphate group)
- Hydrolases: catalyze the hydrolysis of various bonds
- Lyases: cleave various bonds by means other than hydrolysis and oxidation
- Isomerases: catalyze isomerization changes within a single molecule
- Ligases: join two molecules with covalent bonds

In this classification, proteases are hydrolases as they catalyze the hydrolysis of peptide bonds. However, all enzymes fundamentally have the same working principle. They have an active site, which consists of the binding site (preference site) and the catalytic site. The binding site recognizes the target molecule (also called substrate) and binds it. Once a target molecule is bound to the enzyme, various chemical bonds in the enzyme's catalytic site can be used to affect the substrate's chemical structure.

There are two proposed theories to explain the specificities of binding. The first one is the "lock and key" theory, which suggests that both the enzyme and the substrate possess specific complementary geometric shapes that exactly fit each other [86]. Later, the "induced fit" theory was introduced, which proposes that the active site is reshaped by interactions with the targeted molecule [87]. The principle of the induced fit is shown in Figure 3.3 and this theory helps to explain not only an enzyme's specificity, but also the stabilization of the transition state achieved by enzymes.

In the case of proteases, a nomenclature exists to describe the binding of a substrate to a protease [81], which we will also use in this thesis. This nomenclature is schematically shown in Figure 3.4. In the active site of the protease, there are so-called subsites that recognize the amino acid sequence of the targeted protein or peptide. These subsites are counted starting at the scissile bond, i.e. the bond that is hydrolyzed by the protease. Towards the N-terminus of this bond, these subsites are named S1, S2 ... Sn, and towards the C-terminus S1', S2' ... Sn'. The subsites thus accommodate the peptide with the residues corresponding to the specific subsite named P1, P2 ... Pn and P1', P2' ... Pn'. The specificity of the protease originates

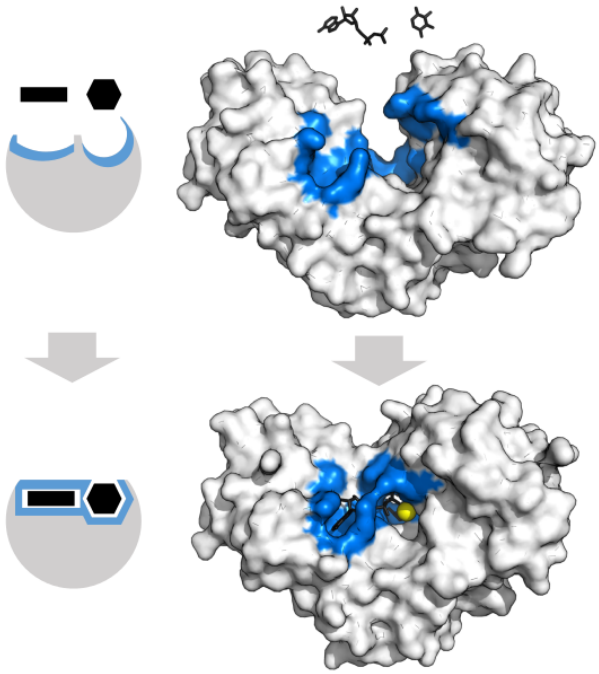

Figure 3.3: Representation of the induced fit theory where the target molecules actively interacts with the enzyme, reshaping its active site. The binding site of the enzyme is shown in blue. Schematic representation (left panel) and induced fit model of hexokinase binding its target molecules adenosine triphosphate and xylose (right panel). [88]

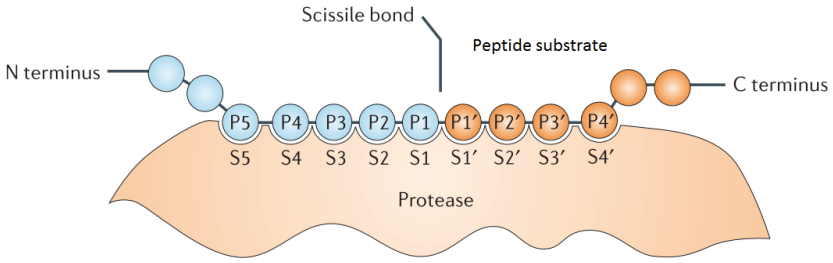

Figure 3.4: Schematic representation of a peptide substrate binding to a protease. [81]

from the overall structure of the active site, which determines which amino acid residues can bind to a specific protease subsite.

Especially important for this thesis work is that proteases, as other enzymes, exhibit the following characteristics [83]:

1. Proteases are usually highly specific, recognizing very precisely their target molecule. This molecule is called a substrate. Given that a SERS substrate is a common name for the metal nanoparticles used to enhance the Raman signal, we make a distinction by using the term peptide substrate in this thesis to refer to protease substrates.

2. Other molecules can affect the activity of a protease. Activators are molecules that can increase proteolytic activity, while inhibitors will decrease it. If activity of a protease is associated with a pathological state in the human body, inhibitors are thus possibly interesting therapeutic drugs, as will be discussed.

3. A protease has an optimal working temperature and pH, and its activity decreases if the conditions in which it is active deviate from the optimal. If a protease is exposed to heat, it may become permanently denatured, losing its structure and catalytic activity.

4. A protease, as any other catalysts, is not consumed during a chemical reaction.

Proteases can be classified into groups based on their catalytic residue, namely serine, cysteine, threonine, aspartic, glutamic and mixed proteases, as well as metalloproteases and asparagine proteases [89]. Additional group

is formed by the proteases for which the catalytic type is unknown. In total almost 600 proteases have been identified in the human genome [90], accounting for around 3% of all human protein-encoding genes [91]. Some of the most widely used proteases come from the family of serine proteases, namely chymotrypsin, trypsin and elastase [91]. Especially trypsin is used frequently for proteomics experiments, due to its stringent cleavage specificity [92]. Trypsin cleaves carboxy-terminal (C-terminal) to arginine and lysine residues, unless they are followed by a proline, in which case peptide bond hydrolysis is severely affected [93]. The catalytic mechanism of trypsin (and other serine proteases) is shown in Figure 3.5. Trypsin is found in the digestive system of many vertebrates, more specifically in the small intestine, where it hydrolyzes proteins [93]. It consequently performs optimal at the temperature of 37 °C and a pH of approx. 7.8. In this thesis, most of the protease experiments were performed using porcine trypsin with a molecular weight of 23.3 kDa [94], as described in more detail in Chapters 4 and 6.

We additionally performed some experiments with endoproteinase GluC [96], which is a bacterial serine protease that cleaves peptides and proteins after acidic amino acids, especially glutamic acid and to some extent aspartic acid [97]. Its molecular weight is 27 kDa and the optimal pH range for its activity is 4-9 [96], thus making it compatible with the reaction conditions for trypsin, which is important to evaluate multiplexed experiments.

3.1.2 Proteases as drug targets

Proteases play an essential role in almost all biological networks and pathways. Not surprisingly, their misregulation was found associated with numerous human diseases [2]. Some of the best-known proteases that cause diseases are:

- Thrombin and plasmin in bleeding disorders and in coagulopathies [98, 99]
- Renin and ACE in hypertension [100]
- Staphylococcal and streptococcal proteases in necrotic skin infections and in the destruction of hemostasis [101, 102]
- Matrix metalloproteases in cancer and inflammation [103, 104]

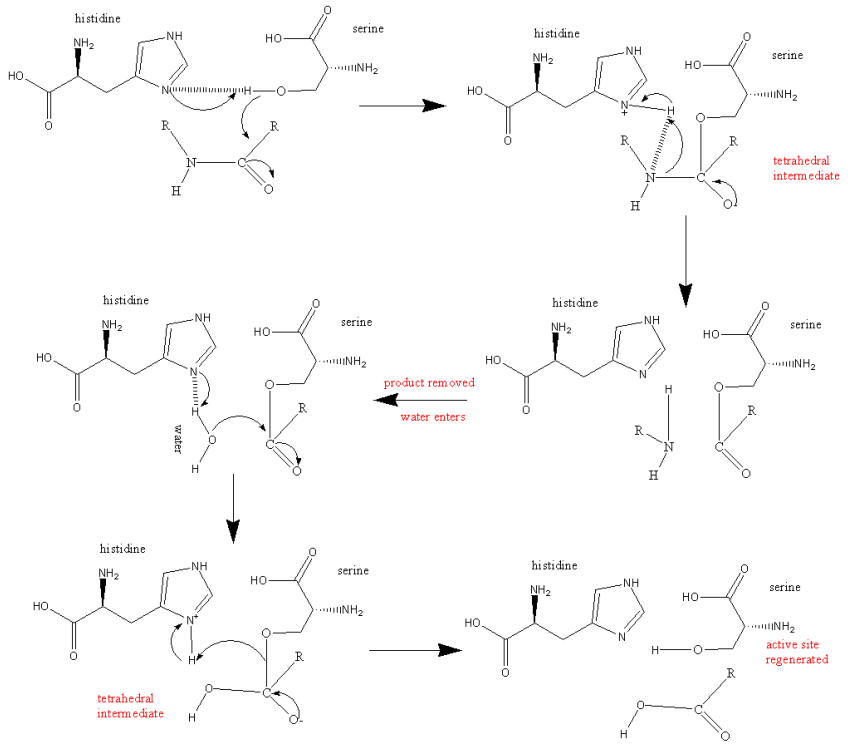

Figure 3.5: Catalytic mechanism of trypsin and other serine proteases. The schematic only shows the serine and histidine of the catalytic centre. The catalytic mechanism also includes an aspartic acid residue which pulls on one of the hydrogens in the histidine side-chain. [95]

- Cysteine cathepsins, caspases and the proteasome in cancer and in neurodegeneration [105–107]

Proteases frequently indicate a poor disease outcome, but their presence can in some cases also help combat the disease [2]. For instance, proteases such as caspases have a pivotal role in apoptosis (programmed cell death). Hence, activation of caspases can reinstate the cell death mechanisms that have been suppressed in cancer cells [108].

Once it is established that a particular protease has an essential role in a given pathology, pharmacological drug searches focus on the discovery of a protease inhibitor [2]. In the majority of cases, this is done by targeting the active site. However, there are several factors that need to be considered when searching for a suitable protease inhibitor as a therapeutic drug:

- Such an inhibitor should ideally be a **small molecule** with the suitable pharmacokinetic characteristics, which can be delivered efficiently to the target protease. The search for new inhibitors is usually based on the structure of known protease substrates, and relatively large peptidic inhibitors are typically required to achieve strong and selective active-site inhibition. It is therefore challenging to identify small molecules with the appropriate inhibition capabilities.
- **Reversible vs. irreversible inhibitors.** Commonly the pharmaceutical drugs are reversible inhibitors, which can reduce the risk of the (long-term) side effects.
- **Biological inhibitors.** This approach explores protein-based inhibitors but might suffer from delivery problems and limited selectivity of such inhibitors. In the last years, efforts have focused on using natural inhibitors as a starting point for the development of the selective inhibitors.

Notably, an estimated 5-10% of all pharmaceutical targets being pursued for drug development are proteases [2]. In the last decades several new protease inhibitors have been introduced on the market (Figure 3.6). For example, inhibitors of the HIV protease are now routinely used in the treatment of HIV infection [109], and inhibitors of the human protease angiotensin-converting enzyme (ACE) have been used for treating cardiovascular diseases for several decades [110].

To effectively assess the efficiency of protease inhibitors on the activity of the targeted protease, it is crucial to have sensitive, selective and accurate

Disease	Protease (class)	Drug name (trade name; company)	Date on market
Hypertension	ACE (metallo)	Captopril (Capoten; Brystol-Myers Squibb)	1981
Hypertension	Renin (aspartic)	Aliskiren (Tekturna/Rasilez; Novartis/Speedel)	2007
HIV/AIDS	HIV protease (aspartic)	Tipranavir (Aptivus; Pfizer/ Boehringer Ingelheim)	2005
Cancer	Proteasome (threonine)	Bortezomib (Velcade; Millennium)	2003
Diabetes	DPP4 (serine)	Sitagliptin (Januvia; Merck)	2006
Coagulation	Thrombin (serine)	Desirudin (Revasc/Iprivask; Novartis)	1998
Coagulation	Factor Xa (serine)	Rivaroxaban (Xarelto; Bayer)	2008
Coagulation	Thrombin (serine)	Dabigatran (Rendix/Pradaxa; Boehringer Ingelheim)	2008
Coagulation	Thrombin (serine)	Argatroban (Acova; GlaxoSmithKline)	2000

Figure 3.6: Some examples of protease inhibitors developed as therapeutic drugs. [2]

analytical methods that test for this protease activity. In the next section, we will provide an overview of commonly used methods for monitoring protease activity and discuss their advantages and drawbacks.

3.2 Overview of methods used for detecting protease activity

A variety of detection techniques have been developed in which protease activity is monitored through the cleavage of specific peptide substrates or the activated protease itself is directly detected. The techniques used for the latter, such as western blot or ELISA, are however typically used for the detection of the presence of the protease, regardless of their activity [5]. Special modifications can be done to assess the actual protease activity using these methods. Methods that monitor the cleavage of specific peptide substrates are more suitable for assessing protease activities. These assays can be divided in homogeneous and heterogeneous assays [5]. In homogeneous assays, both the sample and the peptide substrate are in solution. On the contrary, in heterogeneous assays, peptide substrates are immobilized on a platform, while the protease is in solution. Table 3.1 shows a classification of different techniques used. The main disadvantages of the homogeneous methods are their limited capability of multiplexing, as only a limited number of proteases can be detected in the same sample, and their high sample volume consumption. On the other hand, peptide substrates in the heterogeneous assays are localized very precisely on a solid surface, allowing simultaneous and multiplexed detection of protease activity.

Homogeneous techniques	Heterogeneous techniques
Colorimetric assays	Electrochemical assays
Fluorescence and FRET assays	Liquid crystal assays
Mass spectrometry	Surface plasmon resonance (SPR) assays
Assays using nanomaterials	SERS assays

Table 3.1: Overview of the methods of protease activity detection via peptide cleavage.

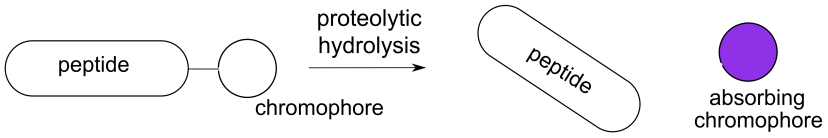

Figure 3.7: The principle of colorimetric sensing.

3.2.1 Homogeneous techniques

3.2.1.1 Colorimetric assays

In colorimetric assays, protease detection relies on monitoring the absorption or transmission spectrum of a specific reporter molecule. The peptide substrate is produced in such a way that it contains a recognition sequence for the protease, as well as a reporter molecule, which can be only detected after cleavage, as shown in Figure 3.7 [111, 112]. A typical reporter molecule is a chromophore such as p-nitroaniline (pNA) [113]. When pNA is attached at the C-terminus of the recognition site of the peptide substrate, no absorption at 405 nm can be detected. However, when pNA is released upon cleavage, it absorbs light at 405 nm, indicative of proteolytic activity. Colorimetric assays consequently also allow monitoring of reaction kinetics however, the presence of extra molecules like pNA in the substrates' P1' position can affect the accessibility of the cleavage sites for many proteases.

Colorimetric assays are widely used as they can be performed using standard laboratory equipment (i.e. an absorption spectrometer) using straightforward experimental procedures. They however offer only limited sensitivity. On the other hand, replacing chromophores with fluorophores greatly increases the sensitivity of the detection, as described in the next section.

3.2.1.2 Fluorescence and Fluorescence Resonance Energy Transfer (FRET) assays

Fluorophores can be used to detect protease activities using the same principle as for chromophores, shown in Figure 3.8(a). Among frequently used fluorophores are 7-amino-4-methyl coumarin (AMC) and 7-amino-4-trifluoromethyl coumarin (AFC) [114]. The changes in the fluorescence spectra after the proteolytic cleavage can be detected using similar spectrophotometers as in the case of the colorimetric assays.

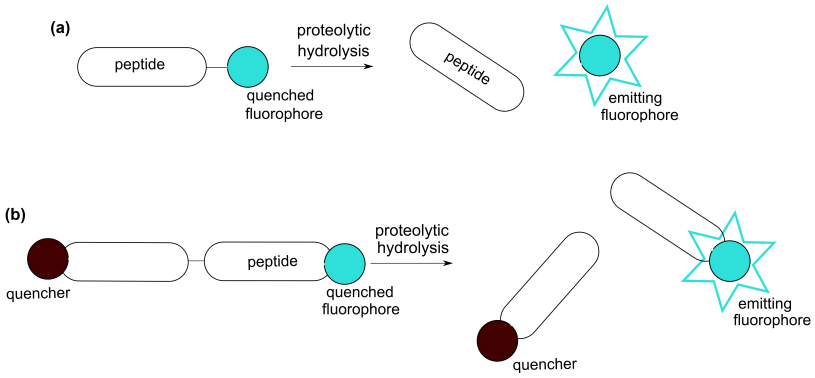

Figure 3.8: Schematic representation of fluorescence (a) and FRET (b) sensing.

The presence of a fluorophore at the P1' position can also influence peptide bond hydrolysis. To mitigate this problem, Fluorescence Resonance Energy Transfer (FRET) can be used [115, 116]. Here, a FRET donor and a FRET quencher are linked by a short peptide containing the cleavage site [117]. When the peptide is intact, the donor and the quencher are in close enough proximity (1-10 nm), so that the quencher suppresses the fluorescence of the FRET donor. After the peptide is cleaved by the protease, the FRET pair is separated and the fluorescence signal increases. The principle of FRET sensing is summarized in Figure 3.8(b).

3.2.1.3 Mass spectrometry assays

Mass spectrometry (MS) allows to identify peptides or peptide fragments by examining the mass-to-charge ratio of the generated gas-phase ions, and it is a widely used tool in proteomics research [118]. In MS, the protease activity is determined by comparing the peptide masses before and after incubation with the protease. The mass of the intact peptide is first determined, which should correspond to the calculated peptide mass based on its amino acid sequence. The peptide is then incubated with the protease, and the peptide mixture examined with MS. Depending on the efficiency of the cleavage, the mixture contains the cleaved peptide fragments, and if the cleavage is slow, still some of the intact peptide.

To determine the cleavage efficiency more quantitatively, liquid chromatography can be used to separate the peptide mixture after the incubation with the protease. In such a way it can be determined, how much of the

peptide is cleaved and how much still intact after a certain incubation time. There are numerous variations on this principle, and in this thesis we used high-performance liquid chromatography (HPLC) combined with MALDI-TOF mass spectrometry, as described in Chapter 6. These specific techniques are described in more details in Appendix B (HPLC) and Appendix C (mass spectrometry). However, compared to the fluorescent or colorimetric assays, the mass spectrometry experiments are resource-, time- and infrastructure-intensive.

3.2.1.4 Homogeneous assays using nanomaterials

More recently, nanomaterials are also used with remarkable detection limits [5]. As an example, a quantum dot-based assay can provide a detection limit as low as 4 pM for trypsin [119]. There, a dithiol peptide substrate is activated by the protease cleavage to form monothiol peptides, which then trigger quantum dot growth, generating a photoluminescence signal readout.

In general, there are several different approaches for protease activity detection using nanomaterials, using amongst other noble metal nanoparticles [120, 121], quantum dots [119, 122] and graphene oxide [123, 124]. For a comprehensive review of the latest developments we refer the reader to [5]. Unfortunately, these newly developed techniques also suffer from limited multiplexing capabilities, characteristic for all the homogeneous protease assays. In the next section, we focus on heterogeneous assays, which allow for simultaneous detection of several proteases simultaneously.

3.2.2 Heterogeneous assays

In the heterogeneous protease assay, peptide substrates are immobilized on solid surfaces while proteases are in solution. A large number of peptide substrates can be immobilized on the solid surface, making it suitable for multiplexing sensing applications. The proteases interact with the peptide substrates at specific locations on this surface, making it possible to identify the optical or fluorescence signals at these discrete locations and associate these signals with a specific protease. Heterogeneous protease assays make use of electrochemistry, surface plasmon resonance, liquid crystals or SERS for the detection of protease activity. The peptide substrates should be carefully designed such that functional groups are present for covalent immobilization of peptide substrates on the solid surfaces (i.e. metal surfaces

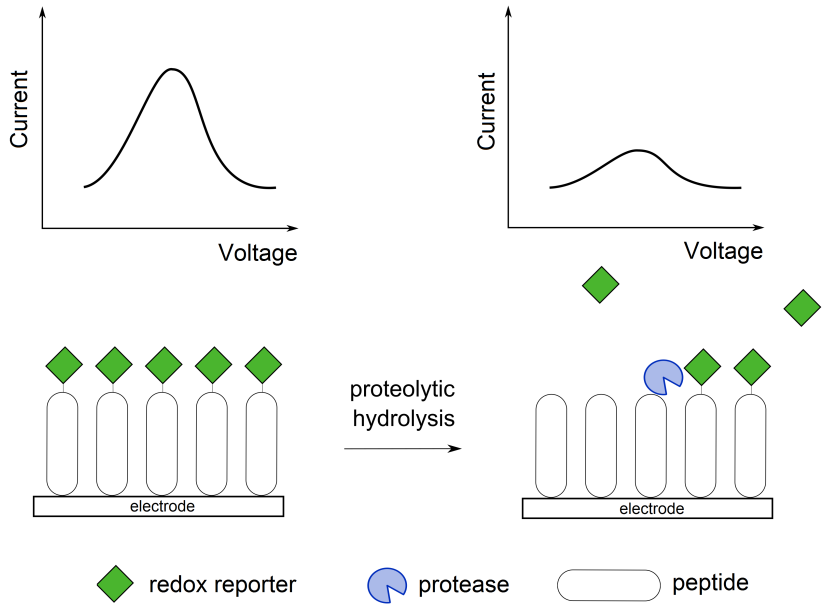

Figure 3.9: The principle of electrochemical detection of protease activity. The turn-off configuration is shown in the figure, where the electrochemical signal decreases upon proteolytic activity.

for electrochemical assays).

3.2.2.1 Electrochemical assays

With electrochemical sensors protease activity is detected via oxidation or reduction reactions that result in electrical signals which can be measured using electrodes [125]. In these sensors, the peptide substrates are usually labelled with redox reporters and immobilized on the electrodes. When a protease cleaves a peptide substrate, the electrochemical signal changes. The principle of electrochemical detection of protease activity is shown in Figure 3.9. In the turn-off configuration (shown in Figure 3.9), the electrochemical signal decreases upon proteolytic cleavage [126], whereas in the turn-on configuration, the signal increases when protease activity is detected [127].

In the last decade several variations of protease activity detection using electrochemical sensors have been developed. Most require synthetic

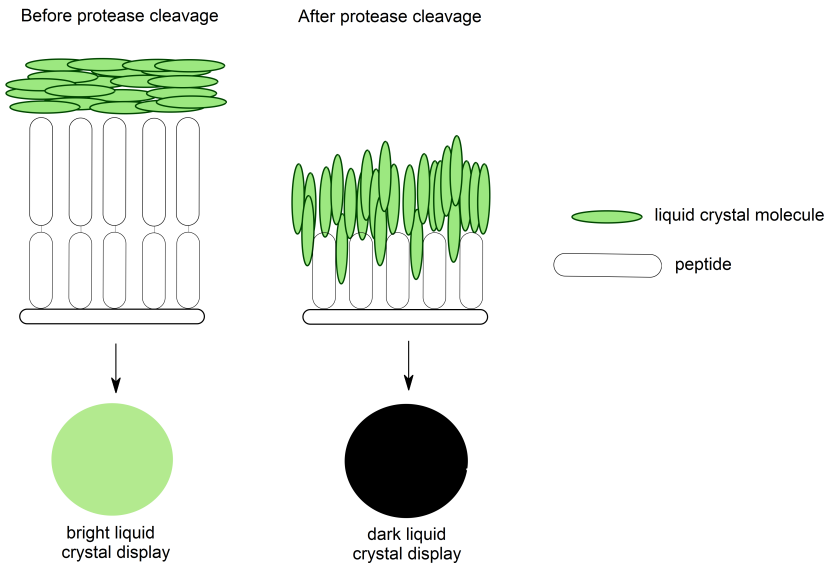

Figure 3.10: Concept of protease activity sensing using liquid crystals.

labels [128] or quantum dots [129] to peptide substrates, both of which may adversely affect protease activities. To avoid influences from synthetic labels, label-free alternatives are therefore preferred for protease activity detection.

3.2.2.2 Liquid crystal assays

Liquid crystals are a class of materials that exhibit a certain degree of molecular order while retaining the fluidity of conventional liquids. There are different liquid crystal phases, depending on the degree of molecular order. Especially the nematic phase is widely used for assay development [5]. In the nematic phase, the rod-like molecules of the liquid crystal are oriented in a specific direction without positional order when subjected to external fields. Important for assay development, the chemical composition of the surface in contact with the liquid crystal can influence the direction of the liquid crystal molecules. Due to the minimization of the free energy, also the liquid crystal molecules further away from the surface orient under the influence of the surface [130].

In the liquid crystal-based assays, the peptide substrate is immobilized

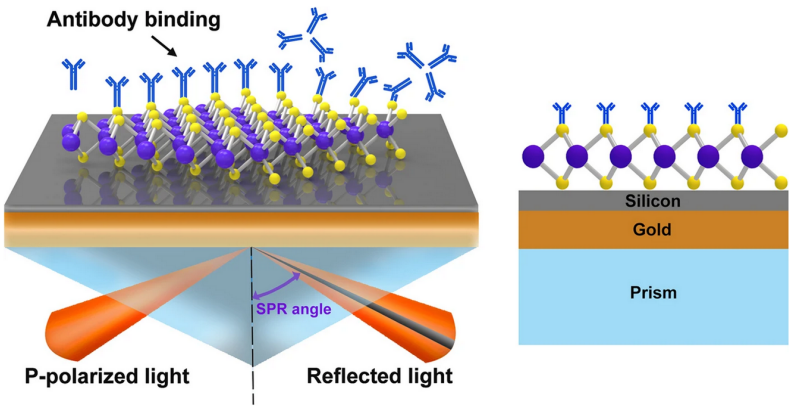

Figure 3.11: Schematic representation of a biosensor based on the surface plasmon resonance. [132]

on the surface, which causes the liquid crystal to orient parallel to the surface and produce a bright optical signal (see Figure 3.10). After the peptide substrates are cleaved by the protease, the decrease in the peptide surface density results in perpendicular orientation of the liquid crystal molecules with respect to the surface, producing a dark optical signal [131]. Liquid crystal-based assays provide real-time detection of protease activity, however further work is required to ensure better selectivity and sensitivity.

3.2.2.3 Surface plasmon resonance (SPR) assays

SPR is a commonly used label-free technique, which can be employed to monitor proteolytic activity without using synthetic labels. We have already discussed the theoretical background of this method in the previous chapter (Section 2.3.1). Shortly, a beam of light hits the gold surface at different incident angles and the intensities of reflected light are then measured at different reflection angles. By determining the angle where the reflected light is minimal, one can deduce the refractive index of the sensor surface. Typically, the gold surface is covered with the analyte. When the protease interacts with the analyte on the surface, this leads to a change in the refractive index (see schematic representation in Figure 3.11).

SPR sensors provide a quantitative detection mechanism, and can furthermore be used for the real-time activity monitoring. However, this technique is more adapted for monitoring protein-protein interactions [133]. Yet, to

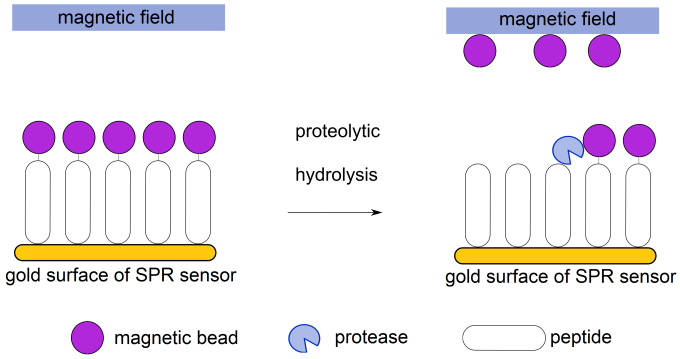

Figure 3.12: Schematic representation of a SPR biosensor, where the detection limit is increased by monitoring the electrochemical signal changes caused by the magnetic beads.

detect cleavage of a peptide substrate by a protease, some form of signal amplification is necessary, such as for example the use of magnetic beads in a magnetic field [134]. There, the peptide substrate with a conjugated magnetic bead is attached to the gold surface of SPR sensor (see Figure 3.12). When the HIV-1 protease cleaves its peptide substrate, the external magnetic field causes the magnetic beads to leave the surface of the SPR sensor, resulting in a change of the electrochemical signal. Using this assay, the detection limit of 10 pg/ml was achieved.

3.2.2.4 SERS

SERS-based protease assays can be implemented in a homogeneous format, where colloidal metal nanoparticles are used together with a SERS reporter molecule. The aggregation or dispersion of the nanoparticles in the presence of target proteases then produces SERS signals [135, 136]. The uncontrolled aggregation of the colloidal nanoparticles can however lead to reproducibility issues. To overcome these, the heterogeneous format can be used, where peptide substrates are immobilized on a reproducibly fabricated SERS substrate [137]. Proteolytic cleavage of a peptide substrate then causes changes in the SERS signal, as the peptide fragment diffuses away from the metal nanoparticle, effectively reducing its SERS signal. This is the approach we choose in this thesis, and its principle is described in detail in the next chapter. The main advantages of the heterogeneous SERS assays are:

- Controlled and reproducible performance of SERS substrates
- Good sensitivity and selectivity
- Possibility of multiplexing

3.3 Conclusion

In this chapter, we introduced proteases and their importance in human pathologies. As they are involved in numerous biological networks and pathways, they are an important factor in diseases ranging from cardiovascular disorders to cancer. They are therefore important targets for drug development, and sensitive, selective and multiplexed detection of protease activity is necessary for the pharmacological development of new drugs. We reviewed established and emerging techniques for detection of proteolytic activity, and summarized their advantages and drawbacks. In this thesis, we used a heterogeneous SERS assay for protease activity detection due to its good reproducibility, selectivity and the possibility of multiplexing. In the next chapter, we will discuss the principle of SERS sensing of proteolytic activity in more detail, and describe the design and fabrication of the suitable peptide substrate.

4

Peptide chemistry

Surface-Enhanced Raman Spectroscopy (SERS) enables selective and sensitive detection of a molecule by acquiring a molecule-specific Raman signal that is enhanced in the proximity of a plasmonic nanostructure. Its specificity and the fact that no labelling is needed, implies that SERS can be efficiently used to detect the activity of proteases. SERS can furthermore provide a real-time, multiplexed method to analyze protease activity. Moreover, a transition from free-space to a waveguide-based SERS detection of protease activity allows parallel measurements of a large number of SERS analytes, enabling high-throughput assays that are particularly of interest for pharmacological drug discovery [5].

In this chapter, the concept behind SERS-based sensing of protease activity is explained, and this for a single protease as well as for multiplexed experiments in which the activity of two (or more) proteases is detected simultaneously. We furthermore take a closer look at the design of the peptide substrates to be used and discuss their production.

4.1 Concept of SERS-based sensing of protease activity

SERS-based protease activity sensing relies on monitoring cleavage of specific peptide substrates, and is shown schematically in Figure 4.1. Here, the selected SERS substrate is labelled with a peptide substrate for trypsin, our model protease. We have designed a specific peptide substrate for trypsin with the amino acid sequence NH2-CALNN(CN-F)GSG(CN-F)GGGGV**R**-GNFSF-COOH, where each letter represents a natural amino acid and CN-F represents the non-natural aromatic amino acid cyano-phenylalanine (Figure 4.2). Trypsin cleaves the peptide at the carboxyl side of the arginine (R). The peptide contains a cysteine (C) that allows it to covalently bind to the gold nanostructure, which provides the SERS enhancement, with the peptide forming a monolayer on the gold surface. The Raman signal of the peptide comes from the two aromatic amino acids, in this particular case cyano-phenylalanine that provides the reference SERS peak at 1180 cm^{-1} and phenylalanine (F) with a peak at 1003 cm^{-1}. Each aromatic appears in the sequence twice to double their SERS signal strength. Between the two aromatics, there is a specific cleavage site for trypsin, which cleaves C-terminal to the arginine residue (R). After cleavage of the peptide, the short peptide fragment NH_2-GNFSF-COOH diffuses away from the gold surface, consequently reducing the intensity of the 1003 cm^{-1} peak in the SERS spectrum. The SERS peak originating from the CN-F is expected to stay constant, and can thus serve as a normalization peak. Peptide design and production are discussed in more detail in section 4.3.

4.2 Multiplexing capabilities – detecting the activities of different proteases simultaneously

Our approach should also allow multiplexing measurements in which one monitors the activity of two (or more) different proteases upon using different, protease-specific peptide substrates with non-overlapping SERS peak, as shown in Figure 4.3.

A key prerequisite for multiplexing measurements is the use of Raman reporters with non-overlapping SERS peaks in order to distinguish the contributions of the different proteases. As the three natural aromatic amino acids, namely phenylalanine, tyrosine and tryptophan, only offer limited

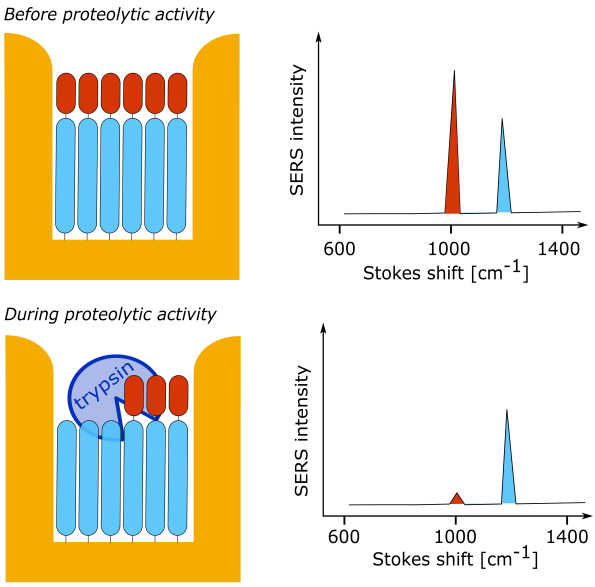

Figure 4.1: The concept of protease activity detection via peptide bond cleavage using surface-enhanced Raman spectroscopy. The peptide forms a monolayer on the gold nanostructures, and is then cleaved by a protease, here trypsin is used as an example, resulting in the decrease of the SERS peak of the part of the peptide that is cleaved off and exits the nanostructure.

Figure 4.2: Peptide substrate for trypsin, written with using the single-letter amino acid code. White letters represent the aromatic amino acids that provide SERS signals, namely phenylalanine (F) and the non-natural cyano-phenylalanine (CN-F).

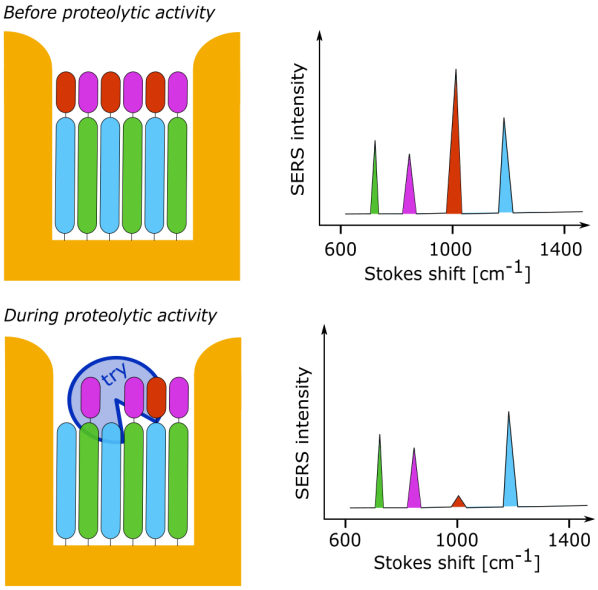

Figure 4.3: Multiplexing experiment where one detects the activity of two different proteases.

possibilities for multiplexing, we examined several non-natural aromatic amino acids with the aim of expanding our multiplexing possibilities. Such non-natural aromatics can additionally offer potentially higher Raman cross-sections, which provide higher SERS signal strengths than those of the natural aromatics, thus improving the signal-to-noise ratio. Here, we report on the SERS spectra and SERS peaks of different aromatic amino acids tested and assess their potential for multiplexing applications.

We investigated all three natural and eight selected non-natural aromatic amino acids (Table 4.1). We have chosen to investigate derivatives of tyrosine [138] and phenylalanine [139], as well as phenylalanines containing stable heavy isotopes of hydrogen, carbon and nitrogen [140]. To be able to record their SERS spectra, we incorporated these amino acids in a short peptide chain NH_2-CALNNXG-COOH, where X denotes the individual aromatic amino acid tested. In this peptide sequence, cysteine (C) again allows the peptide to bind to the gold nanodomes. The SERS spectra were obtained using a laser power of 1 mW and an integration time of 3 s for the Raman shifts of 300-1700 cm^{-1}. Background-subtracted SERS spectra of the aromatic amino acids are shown in Figure 4.4 for the phenylalanine derivatives and in Figure 4.5 for the tyrosine derivatives.

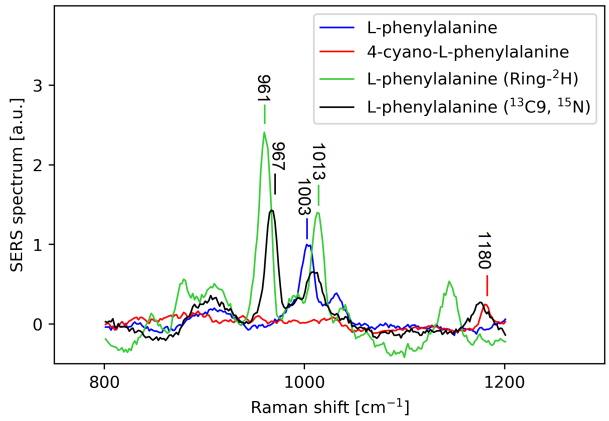

Figure 4.4: SERS spectra of phenylalanine derivatives in the spectral region 800-1200 cm^{-1}. The spectra are normalized on the 1003 cm^{-1} phenylalanine peak and the most prominent SERS peaks are indicated.

Aromatic amino acid	SERS peak position [cm^{-1}] with relative SERS peak strength
L-phenylalanine	1003 (s), 1031 (m)
L-tyrosine	831 (m), 850 (m), 1260 (w)
L-tryptophan	754 (m), 1118 (w), 1356 (m)
4-cyano-L-phenylalanine	1180 (m)
4-benzoyl-L-phenylalanine	1003 (m), 1031 (m), 1152 (m)
3,4-dichloro-L-phenylalanine	-
L-phenylalanine (ring-^{2}H)	961 (vs), 1013 (s), 1145 (s)
L-phenylalanine (^{13}C9, ^{15}N)	967 (s), 1009 (m), 1173 (m)
3-nitro-L-tyrosine	752 (m), 825 (vs), 1254 (s), 1355 (s)
O-phospho-L-tyrosine	820 (w), 843 (w), 1229 (w)
3-amino-L-tyrosine	Strong, but unstable SERS signal

Table 4.1: Measured prominent SERS peak positions of different aromatic amino acids with relative SERS peak strengths. Abbreviations: vs: very strong, s: strong, m: medium, w: weak.

After subtracting the SERS background from the spectra, we identified SERS peaks pertaining to the investigated aromatics (Table 4.1). For our analysis, we assumed that the aromatic amino acid residues provide the

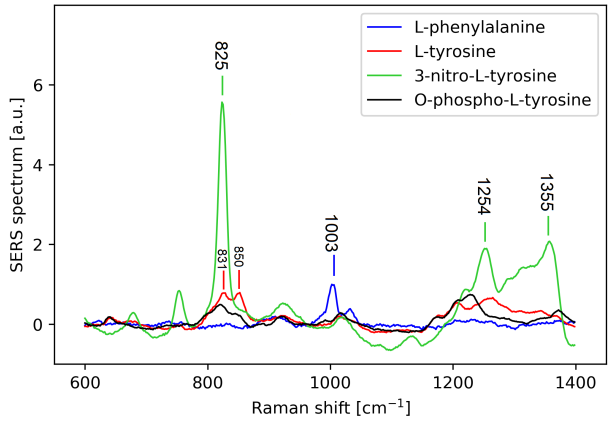

Figure 4.5: SERS spectra of selected tyrosine derivatives in the spectral region 600-1400 cm^{-1}. The SERS spectrum of phenylalanine is included for comparison with Figure 4.4 and the spectra are normalized on the 1003 cm^{-1} phenylalanine peak.

dominant features in the SERS spectra of peptides [141]. Most of the tested aromatic amino acids provided characteristic SERS peaks in the examined spectral region, more specifically in the 600-1400 cm^{-1} range. We notice that the SERS peaks of some aromatics (partially) overlap, such as for example the 961 cm^{-1} peak of L-phenylalanine (Ring-^{2}H) and the 967 cm^{-1} peak of the L-phenylalanine(^{13}C9, ^{15}N). Special care has to thus be taken to choose compatible aromatics as Raman reporters during multiplexing experiments. Several non-natural aromatics additionally provide strong SERS peaks compared to their corresponding natural aromatic amino acids, thus improving the signal-to-noise ratio. Of the examined non-natural aromatics, 3-nitro-tyrosine and the two phenylalanine molecules containing stable heavy isotopes seem particularly promising for multiplexing applications.

4.3 Design and production of peptide substrates

4.3.1 Design of peptide substrates

When using SERS to monitor protease activity, one monitors if a specific substrate peptide is cleaved by a given protease. To efficiently achieve this the peptides should form a stable monolayer on a gold surface, provide an accessible cleavage site and include strong SERS scatterers. The

peptide length should furthermore be limited to a few nanometers as the SERS signal decreases with increasing distance from the surface of the gold nanostructures [142].

We have designed a specific peptide substrate for trypsin with the amino acid sequence NH2-CALNN(CN-F)GSG(CN-F)GGGGV**R**-GNFSF-COOH. The peptide sequence starts with a cysteine (C) that allows it to bind to the gold nanostructure via a covalent sulfur-gold bond [143]. The amino acids alanine (A) and leucine (L) allow the formation of a self-assembled monolayer [144]. They are followed by a double hydrophilic asparagine (N) to ensure good solubility [144]. CALNN is followed by the sequence containing cyano-phenylalanine (CN-F), a non-natural aromatic amino acid that serves as a first SERS reporter. If present, the SERS peak of CN-F confirms that either the uncleaved or cleaved peptide is still bound to the gold surface. This means that there has not been any desorption of the peptide from the gold surface or ligand exchange, where the peptide would be substituted on the gold surface by another molecule with higher affinity to the gold [145]. To increase the strength of the SERS signal that can be detected, we used two cyano-phenylalanines to effectively double the SERS signal. The two cyano-phenylalanines are separated by a serine (S) that increases the overall solubility of the peptide. Our experiments have however shown that the peptide containing the sequence (CN-F)S(CN-F) is not stable in an ammonium bicarbonate buffer at pH=7.8 needed for our protease experiments, possibly due to covalent interactions between the hydroxyl function (OH) in the side chain of serine and the cyano function (CN) in the side chain of cyano-phenylalanine. One glycine was therefore added on each side of the serine to position the possibly interacting side chain further apart, thus ensuring that the resulting peptide was stable in the ammonium bicarbonate buffer. Further, we included a stretch of glycines (GGGG), small amino acids forming a flexible chain to improve the accessibility of the cleavage site for the protease. The presence of this spacer was found to be crucial for trypsin activity on surface-bound peptides [49]. This stretch of glycines is followed by VR being respectively the P2 and P1 subsite for trypsin, as trypsin cleaves at the carboxyl side of arginine (R) and lysine (K) [92]. The hydrophobic valine (V) in the P2 position was found to increase the efficiency of the catalysis [146]. This cleavage site is followed by a GNFSF sequence. The small glycine at P1' ensures good accessibility of trypsin to the cleavage site, and the hydrophilic asparagine (N) and serine (S) increases the solubility of the C-terminal part of the peptide that will be cleaved off by trypsin. The second aromatic amino acid phenylalanine (F) clearly also functions as a second SERS reporter and is again doubled

to increase its SERS signal. Consequently, for this specific substrate the intensity of the SERS peak of F divided by that of CN-F serves as a metric for the cleavage and diffusion of the –GNFSF fraction.

An analogous peptide substrate for different proteases can be produced by adjusting the specific cleavage site. We thus produced a peptide substrate for endoproteinase GluC, which cleaves the peptide bond C-terminal to glutamic acid (E) residues [147]. This was achieved by placing the amino acids NNE- in the P3-P1 positions. If we want to achieve multiplexing, we also need to use aromatic amino acids with non-overlapping SERS peaks in the peptide substrates we want to monitor simultaneously. The peptide substrate for endoproteinase GluC has thus the following peptide sequence: NH_2-CALNN(CN-F)S(CN-F)GGGGNN**E**-SYSYH-COOH.

4.3.2 Production of the peptide substrates

Peptides were synthesized using standard solid-phase fluorenylmethyloxycarbonyl chloride (Fmoc) chemistry on a SyroI (Biotage) instrument. The synthesis was started on 25 μmol preloaded Fmoc-His (Trt) or Fmoc-Phe wang resin respectively (Novabiochem). Amino acids were coupled in 4-fold excess using HOBT/HBTU activation. The peptides were cleaved with TFA containing phenol, triisopropylsilane and 5 % water for 3 hours. Then, peptides were precipitated with tributylmethyl ether and recovered by centrifugation at 2000xg. The ether washing/centrifugation step was repeated three times. The peptides were purified using a water/acetonitrile gradient elution on by using RP-HPLC on a RPC C18 column (Macherey-Nagel) and characterized using MALDI-TOF mass spectrometry. The reader can find more information on HPLC in Appendix B, whereas MALDI-TOF principle is described in Appendix C.

Several different peptide substrates for trypsin and for endoproteinase GluC were synthesized using the characteristics mentioned in the previous section, principally only by changing the cleavage site and the aromatic amino acids used as Raman reporters for SERS experiments. All the peptides that were synthesized are listed in Table 4.2. In the list below we highlight how the search for the optimal peptide substrate for trypsin has evolved. The cleavage site is marked in red, whereas the aromatic amino acids are underlined.

- NH_2-CALNNYGGGGV**R**GNF-COOH was already used in the protease activity sensing experiments on free-space based gold nan-

Peptide sequence	Molecular mass [Da]	Substrate for	Comments
NH_2-CALNNYGGGGGVRGNF-COOH	1498.68	Trypsin	Only natural aromatics
NH_2-CALNN(CN-F)GGGGGVRGNF-COOH	1506.69	Trypsin	
NH_2-CALNN(benzoyl-F)GGGGGVRGNF-COOH	1585.7	Trypsin	SERS peak of benzoyl-F overlaps with that of F
NH_2-CALNN(dichloro-F)GGGGGVRGNF-COOH	1550.7	Trypsin	No SERS peaks of dichloro-F
NH_2-CALNN(CN-F)S(CN-F)GGGGGVRGNFSF-COOH	1999.89	Trypsin	Doubled aromatics, not stable in ammonium bicarbonate (pH=7.8)
NH_2-CALNN(CN-F)GSG(CN-F)GGGGGVRGNFSF-COOH	2113.93	Trypsin	Doubled aromatics
NH_2-CALNNYGGGGNNESWH-COOH	1691.7	GluC	Only natural aromatics
NH_2-CALNN(CN-F)GGGGNNESYH-COOH	1677.67	GluC	
NH_2-CALNN(CN-F)S(CN-F)GGGGNNESYSYH-COOH	2186.86	GluC	Doubled aromatics
NH_2-CALNN(benzoyl-F)GGGGNNESYH-COOH	1756.67	GluC	
NH_2-CALNN(benzoyl-F)S(benzoyl-F)GGGGGNNE-SYSYH-COOH	2344.86	GluC	Doubled aromatics
NH_2-CALNN(CN-F)S(CN-F)GGGGVEGNFSF-COOH	1972.89	GluC	Stable in ammonium bicarbonate (pH=7.8), not suitable for multiplexing with trypsin
NH_2-CALNN(CN-F)GSG(CN-F)GGGGVEGNFSF-COOH	2086.93	GluC	Not stable in ammonium bicarbonate (pH=7.8)

Table 4.2: The list of synthesized peptide substrates for trypsin and endoproteinase GluC (GluC).

odomes [49]. It contains two natural aromatic amino acids as the SERS reporters. Whereas the phenylalanine (F) SERS peak is prominent, the SERS peak of the tyrosine (Y) is fairly weak, making the detection and the analysis of the SERS spectra challenging. We have therefore chosen to replace tyrosine with a non-natural aromatic that would provide a stronger SERS signal.

- In the peptide NH_2-CALNNXGGGGV**R**GNF-COOH the amino acid marked with X represents several different non-natural aromatics that we used to replace tyrosine, namely cyano-phenylalanine, benzoyl-phenylalanine, dichloro-phenylalanine and azido-phenylalanine. We could not produce a peptide containing azido-phenylalanine, since the azido group was reduced to an amino group during peptide purification. We were able to incorporate the other three non-natural aromatics into the peptide, but the dichloro-phenylalanine did not provide any characteristic SERS peaks in our spectral region of interest. The benzoyl-phenylalanine provided two SERS peaks, one at 1150 cm^{-1}, and another at 1003 cm^{-1}. However, the peak at 1003 cm^{-1} appears at exactly the same spectral position as the peak of phenylalanine, making the combination of benzoyl-phenylalanine and phenylalanine incompatible. On the other hand, cyano-phenylalanine provided a strong characteristic SERS peak at 1180 cm^{-1}.

- NH_2-CALNN(CN-F)GGGGV**R**GNF-COOH was fabricated with F as a SERS reporter of the protease cleavage and cyano-phenylalanine (CN-F) as a reference SERS signal. The two aromatic amino acids provide strong, non-overlapping SERS peaks, making their combination suitable for protease activity detection.

- An easy way to increase the SERS signal of the peptide is to simply double (triple, quadruple ...) the amount of the aromatic amino acids that provide the SERS signals. In order to implement that, we tried to fabricate the peptide NH_2-CALNN(CN-F)(CN-F)GGGGV**R**GNFF-COOH. However, due to the increased amount of the hydrophobic aromatic amino acids, the resulting peptide was too hydrophobic and could not be dissolved in water-based solvents.

- To mitigate the hydrophobicity of doubled aromatics, we used serine (S) as a hydrophilic spacer between the two adjacent aromatic amino acids in the peptide NH_2-CALNN(CN-F)S(CN-F)GGGGV**R**GNFSF-COOH. This way we fabricated a peptide that could be dissolved in water-based solvents. However, we have noticed chemical instability of the peptide in the water-based buffer (namely ammonium

bicarbonate buffer). We supposed that the instability was coming from the chemical interactions between the cyano group of CN-F and the -OH group of the serine, however this could not be corroborated experimentally.

- To overcome the apparent instability of the peptide with doubled aromatics separated with a serine, we used glycine as a spacer between cyano-phenylalanine and serine, resulting in a peptide NH_2-CALNN(CN-F)GSG(CN-F)GGGGV**R**GNFSF-COOH. This peptide proved to be chemically stable, and provided stronger SERS signal of two non-overlapping SERS peaks. Using the same principles, the amount of the aromatic amino acids could be further increased in the future to provide even stronger SERS signals.

In parallel, we also followed a similar path to produce optimal peptide substrate for GluC. The main difference compared to the trypsin substrate was that in the case of GluC, it was the peptide with the -GSG- spacer between the two cyano-phenylalanines that was chemically unstable. We therefore used the peptide with only serine as the spacer for the GluC experiments. Further experiments should be performed to establish the underlying reason for this inconsistent behaviour of different peptide substrates.

Incorporation of non-natural aromatic amino acids in the peptide chain is in principle done exactly the same as for natural aromatics, and can therefore be automatized. However, special care was taken to check that the peptide was correctly synthesized and that there was no interaction between the side chains of (adjacent) amino acids. The problems we encountered when incorporating non-natural aromatics are summarized below. If found, a solution to the problem or a workaround is described.

- The azido side group of the azido-phenylalanine was reduced to an amino group during the peptide purification.
- The nitro group of the nitro-tyrosine oxidized the side chain of cysteine when the peptide was dissolved in the DMSO.
- It is more problematic to incorporate non-natural aromatics close to the C-terminal end of the peptide, so these were incorporated closer to the N-terminal end.
- Special care has to be taken when incorporating nitro- or phosphotyrosine in the peptide chain. Since the bond is not very stable during deprotection, the efficiency of the peptide synthesis can be rather low.

- In the trypsin peptide substrate, the side group of the cyano-phenylalanine can potentially react with the –OH side group of the serine in ammonium bicarbonate at pH = 7.8. Glycine can be added as a spacer in the peptide sequence between the two amino acids to prevent the unwanted interaction.

Although the peptide substrates for both trypsin and endoproteinase GluC were designed in such a way that they should be cleaved by their respective proteases and show the corresponding SERS peak decrease, we decided to evaluate if this was the case. Hence, a series of experiments was designed and these are described in more detail in Chapter 6. To demonstrate the SERS-based detection of the protease activity, mostly the peptide NH_2-CALNN(CN-F)GSG(CN-F)GGGGV**R**-GNFSF-COOH for trypsin, and NH_2-CALNN(CN-F)S(CN-F)GGGGNN**E**-SYSYH-COOH for endoproteinase GluC were used, as described in Chapter 6.

5

From free-space to waveguide-based SERS platforms

A variety of plasmonic nanostructures has been developed for SERS signal excitation and collection in a conventional free-space microscope, among which the gold nanodomes offer one of the highest SERS enhancements [49]. Nanophotonic waveguides recently emerged as an alternative to the conventional Raman microscope as they can be used to efficiently excite and collect Raman signals [54]. Integration of plasmonic structures on nanophotonic waveguides enables reproducible waveguide-based excitation and collection of SERS spectra, as first demonstrated in integrated bowties using a monolayer of nitrothiophenol [77]. However, the SERS enhancement of the integrated bowties is still relatively low compared to the free-space excited gold nanodomes, and the gold nanodomes outperform the integrated bowties by a factor of 300 in terms of the signal-to-noise ratio. In this chapter, we first show that replacing the titanium adhesion layer with 3-mercaptopropyltrimethoxysilane leads to a 3-fold increase of the collected SERS signal from integrated bowties. To achieve even higher SERS enhancements, we examine several other waveguide-based SERS platforms, such as integrated nanotriangles [78] and nanoplasmonic slot waveguides [79]. We compare the SERS performance of free-space excited gold nanodomes and the waveguide-based SERS platforms. We evaluate the SERS signal

enhancement and the SERS background of the different SERS platforms using a monolayer of nitrothiophenol. We show that the nanoplasmonic slot waveguide approaches the gold nanodomes in terms of the observed signal-to-background ratio. Due to the less efficient fabrication process of the waveguide-based SERS platforms compared to the gold nanodomes, we also explore possibilities to clean and reuse the waveguide-based SERS chips and therefore examine hydrogen plasma cleaning of SERS substrates as an alternative to oxygen plasma cleaning, and show that hydrogen plasma cleaning leads to much more reproducible SERS spectra. The text of this chapter has been adapted from some of my published papers [148–150].

5.1 Using an organic adhesion layer to increase the waveguide-based SERS signal

On-chip Surface Enhanced Raman Spectroscopy was first demonstrated when gold bowtie antennas integrated on silicon nitride (Si_3N_4) waveguides were used to both excite and collect SERS spectra of gold-bound monolayers of 4-nitrothiophenol [77]. However, the sensitivity of waveguide-based SERS was still insufficient for the detection of biomolecules which have small Raman cross-sections. We propose the use of an organic adhesion layer to improve the field enhancement of the plasmonic antennas. This adhesion layer is a thin layer ensuring the attachment of gold antennas to the silicon nitride waveguide. Typically, a few nanometers thick adhesion layer of titanium (Ti) or chromium is used in the fabrication process. However, it has been demonstrated that metal adhesion layers dampen the localized surface plasmon resonance of the antennas, consequently lowering the SERS signal [151, 152]. The organic molecule 3-mercaptopropyltrimethoxysilane (MPTMS) has been proposed as a non-damping alternative to metal adhesion layers, and up to 10-fold enhancement of the SERS signal has been reported for top-down excitation [152]. In this section, we experimentally compare the influence of titanium and MPTMS adhesion layers on the waveguide excited SERS signal of bowtie antennas on a single-mode photonic waveguide. The text of this section has been adapted from the conference paper [148].

Gold bowtie antennas on a silicon nitride waveguide (as seen in Figure 5.1) were fabricated using a two-step electron beam lithography process [77]. First, gold antennas and alignment markers were defined using a liftoff process. Next, single mode Si_3N_4 waveguides were etched around these antennas. Samples with a titanium adhesion layer, an MPTMS ad-

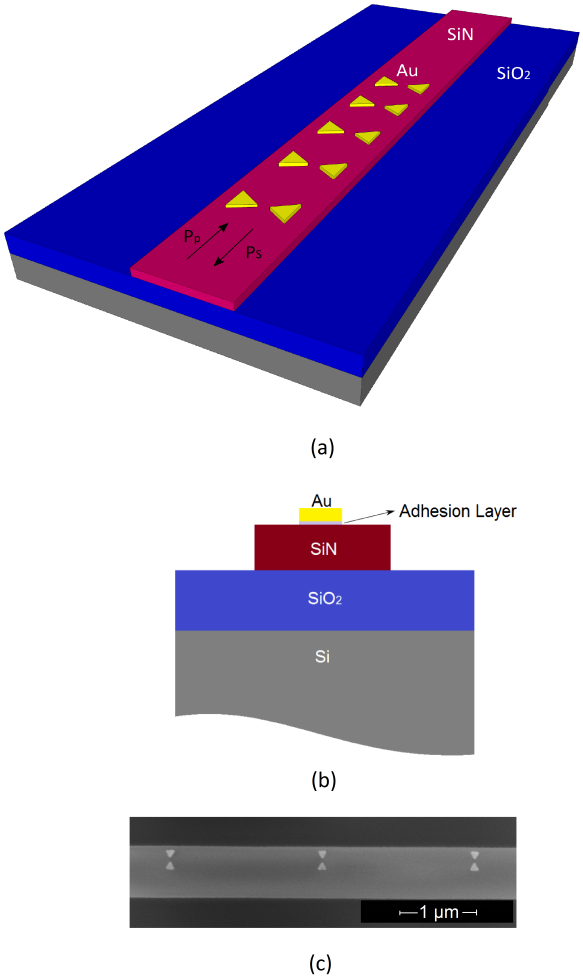

Figure 5.1: (a) Schematic of gold bowtie antennas on a Si_3N_4 rib waveguide. 10 bowtie antennas were fabricated on each waveguide, with a gap of 50 nm, length of 110 nm and a gold thickness of 30 nm. Antennas were excited with TE-polarized pump light P_p and Raman signal P_S was collected in back reflection geometry. (b) Cross-section view of an antenna on a waveguide, showing the adhesion layer between the gold antenna and the Si_3N_4 waveguide. In this work, we compared the influence of a titanium adhesion layer, an MPTMS adhesion layer or no adhesion layer on the SERS signal. (c) SEM image of bowtie antennas on Si_3N_4 waveguide.

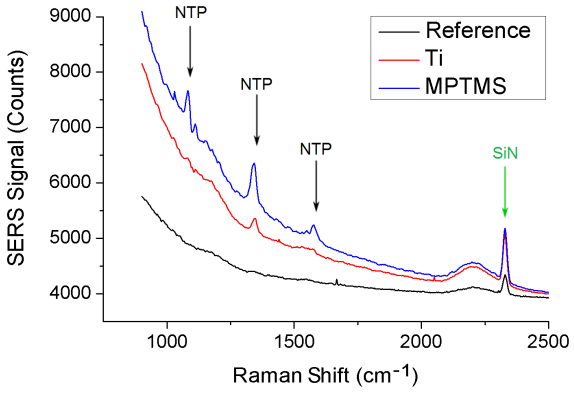

Figure 5.2: Raman spectra of NTP measured on a Si_3N_4 waveguides functionalized with 10 gold bowtie antennas for both titanium and MPTMS adhesion layers, compared to the spectrum of a reference waveguide. Black arrows indicate peaks characteristic of NTP, whereas the green arrow marks the position of Si_3N_4 peak that is used as a reference peak to achieve maximum coupling of the light to the waveguide.

hesion layer or no adhesion layer were fabricated. The efficiency of the adhesion layer was defined as the percentage of antennas left on the waveguides at the end of processing (out of 60 antennas in total for each sample). It amounted to 100 % for the titanium adhesion layer, 92 % for the MPTMS adhesion layer and 53 % when no adhesion layer was used. SERS experiments were performed only with the Ti and MPTMS samples.

Samples with Ti and MPTMS adhesion layer were immersed in 4-nitrothiophenol (NTP). This molecule binds selectively to the bowties through a gold-thiol bond, ensuring that the collected SERS signal originates exclusively from the antennas. Bowtie antennas were then excited through the waveguide and SERS spectra of NTP were collected on a confocal Raman microscope (100x/0.9 objective, 785 nm laser, 0.5 mW laser power before the objective) in a back-reflection geometry. The input polarization was aligned to the TE-mode of the waveguide and the spectra were obtained as averages of 10 measurements with integration times of 5 s each. The collected SERS spectra are presented in Figure 5.2. The integrated number of counts at the 1339 cm^{-1} NTP peak was calculated to quantify the strength of the SERS signal (Figure 5.3). The SERS signal from the MPTMS sample was on average (2.9 $\pm$ 0.8)- and (6.3 $\pm$ 1.9)-fold stronger than the signal of the titanium sample from two different fabrication runs.

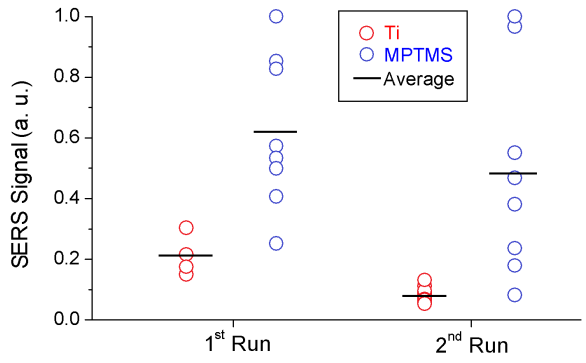

Figure 5.3: Comparison of SERS signal for titanium and MPTMS adhesion layers from two different fabrication runs of identical structures. Circles indicate individual measurements on each fabrication run, and the black line represents the average signal. The average SERS signal increases to about 3- and 6-fold in the two different fabrication runs when titanium adhesion layer is replaced with MPTMS.

We however noticed the high variability in the SERS signal for the MPTMS sample, which together with less than 100 % efficiency of adhesion suggests that the SERS signal from the MPTMS sample is not as reproducible as that from the titanium sample. We attribute the high variability of this signal to small variations in electron beam lithography processing that affect the antenna geometry and therefore its signal enhancement. Even with further optimization of the fabrication process, we were not able to reduce the variability of the SERS signal. To achieve high and reproducible SERS enhancements, we have therefore examined other waveguide-based SERS platforms, such as integrated nanotriangles and the nanoplasmonic slot waveguide. The text of the next section has been adapted from the journal paper [149].

5.2 Comparison of free-space and waveguide-based SERS platforms

5.2.1 Overview of the waveguide-based Raman and SERS platforms

A variety of plasmonic nanostructures providing high SERS enhancements has been developed for SERS signal excitation and collection in a conventional free-space confocal microscope [40]. Colloidal metal nanoparticles enable strong SERS enhancements, yet their fabrication methods offer only limited control of their geometry, size and position, consequently affecting the reproducibility of SERS measurements [40]. Conversely, a variety of SERS substrates has been developed using top-down fabrication techniques such as nanosphere lithography [41–44], and deep-UV [45] and electron beam lithography [46, 47]. These techniques enable precise control of the shape and position of the nanostructures, which allows more tunable and reproducible SERS enhancements [40]. Among the top-down fabricated SERS substrates, the gold nanodomes offer one of the highest SERS enhancements [48,49]. Their fabrication is simple and scalable, whilst ensuring better control of the hotspot size and enhancement factor as compared to colloidal approaches.

Moreover, novel techniques for more efficient collection of Raman signals have recently emerged as alternatives to the conventional Raman microscope, such as hollow-core photonic crystal fibers [50] and nanophotonic waveguides on photonic integrated circuits (PICs) [54, 64, 65, 153]. Nanophotonic waveguides can be used to efficiently excite and collect Raman signals of the molecules close to the waveguide, opening up the possibility to bring the selectivity of Raman measurements to an integrated lab-on-a-chip platform. PICs have also been used to collect SERS signals from external colloidal metal nanoparticles [73–75]. However, to enable reproducible waveguide-based excitation and collection of SERS spectra, top-down fabricated plasmonic structures can be integrated on dielectric nanophotonic waveguides. In the first demonstration of waveguide-excited and collected SERS on integrated plasmonic nanostructures, gold bowtie antennas (Fig. 5.4a) were patterned on a silicon nitride waveguide in a two-step electron beam lithography process [77, 154]. Electron beam lithography is however resource-intensive and time-consuming, so an alternative nanosphere lithography approach was used to fabricate integrated nanotriangles (Fig. 5.4b) [78]. Besides easier fabrication, such integrated

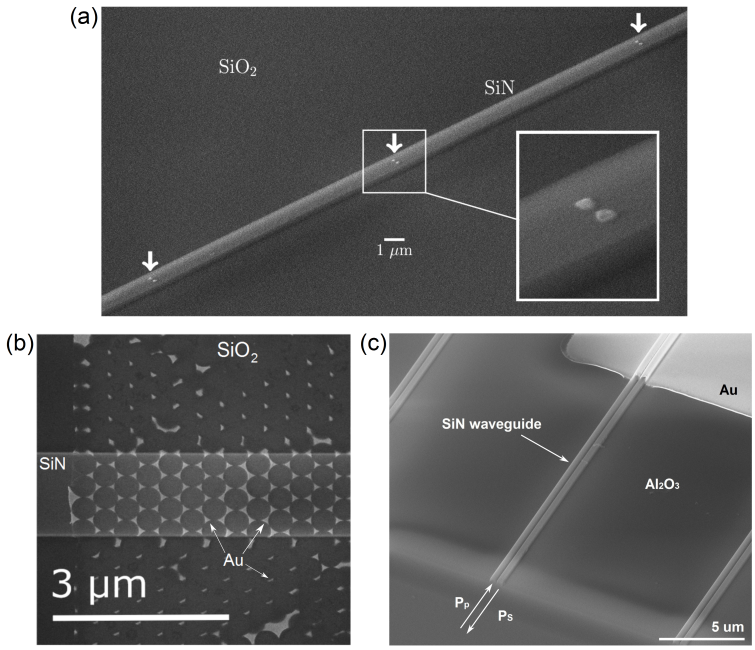

Figure 5.4: (a) Integrated gold bowtie antennas. [77] (b) Integrated nanotriangles. [78] (c) Nanoplasmonic slot waveguide.

nanotriangles also achieved a significant improvement in SERS enhancement compared to integrated bowties. More recently, new waveguide-based SERS platforms have emerged, such as the nanoplasmonic slot waveguide [79, 155–157] and the nanoporous gold on suspended silicon nitride waveguides [158].

Besides the advantages discussed in Section 2.5, the on-chip SERS platform shows great potential for high-throughput SERS assays on low sampling volumes, especially relevant for the detection of biological molecules. However, most biological molecules have low Raman cross-sections, making the SERS enhancements of the integrated bowties and the integrated nanotriangles platforms insufficient for their detection. The high SERS enhancement of the nanoplasmonic slot waveguide (Fig. 5.4c) might however prove sufficient for the SERS detection of biological molecules [79]. In addition to high SERS enhancement, the nanoplasmonic slot waveguides are fabricated using a combination of atomic layer deposition and deep-UV photolithography, enabling mass scale manufacturing. Furthermore, they offer a non-resonant enhancement, making SERS enhancement independent

of excited and scattered wavelengths.

In this section, we evaluate the SERS performance of the two top-performing SERS substrates, one for free-space and another for waveguide-based excitation and collection of SERS signals. This comparison is highly relevant for future on-chip SERS applications. We compare the gold nanodomes in which the signal is excited and collected in free space, and waveguide-based nanoplasmonic slot waveguides. We examine the SERS signal enhancement and the SERS background of the different SERS platforms using a monolayer of nitrothiophenol (NTP). We show that the nanoplasmonic slot waveguide approaches the gold nanodomes in terms of the measured signal-to-background ratio.

5.2.2 Fabrication of SERS substrates

Gold nanodomes were fabricated using a nanosphere lithography (NSL) based process, described in detail in Ref. [49] and shown in Figure 5.5. Briefly, we started from a 200 nm thick film of silicon nitride (Si_3N_4) deposited on top of a 4-inch silicon wafer. We spin-coated a colloidal solution of 450 nm polystyrene beads on the Si_3N_4 surface, thereby generating a monolayer of hexagonally-close packed (HCP) polystyrene beads. The polystyrene beads were then thinned down in an oxygen plasma and a periodic pattern of nanodomes was etched into the Si_3N_4 substrate by an anisotropic reactive-ion etch. These two steps effectively determine the height and the width of the gap between the nanodomes, the two most important parameters for tuning the plasmonic resonance and thus the SERS enhancement factor [49]. The remains of the polystyrene beads were lifted off in dichloromethane and the wafers were cleaned in a piranha solution (H_2SO_4:H_2O_2, 3:1). Finally, a 130 nm thick gold layer was sputtered on the sample. The nanodomes were characterized by scanning electron microscopy and the nanodome gap size was determined to be 12 ± 2 nm. UV-VIS reflection and SERS measurements were performed to optimize the localized surface-plasmon resonance wavelength of the gold nanodomes to match the 785 nm laser used for the SERS excitation, as published in [48]. 3D FDTD simulations predict the maximum SERS enhancement factor of the gold nanodomes for a single molecule in the order of 10^7 [49].

Nanoplasmonic slot waveguides were fabricated using a combination of atomic layer deposition and deep-UV photolithography, as described in detail in Ref. [79] and shown in Figure 5.6. Firstly, 2.3 μm thick SiO_2 and 220 nm thick Si_3N_4 layers were deposited on a 200 nm silicon wafer. The

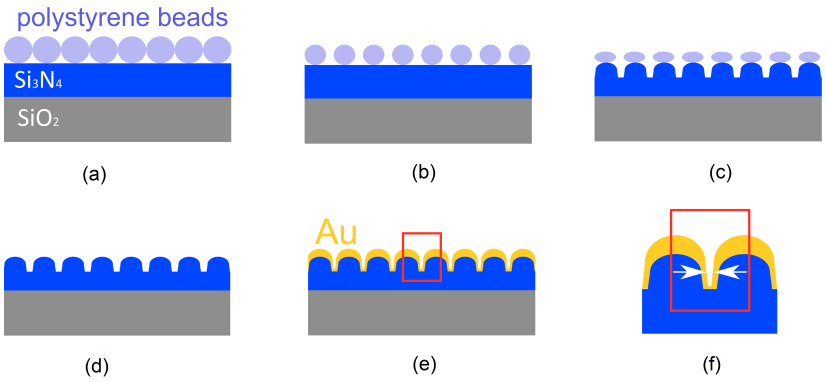

Figure 5.5: Fabrication process of gold nanodomes. (a) Spincoating of polystyrene beads on a Si_3N_4 chip. (b) Thinning down of the polystyrene beads by oxygen plasma. (c) Etching of the nanodome pattern in Si_3N_4. (d) Removal of the remains of the polystyrene beads. (e) Gold deposition. (f) The arrows mark the gap of the gold nanodomes.

Si_3N_4 slot waveguides were patterned with 193 nm deep-UV optical lithography and subsequently etched by a reactive-ion etch process. The resulting average slot width was 150 nm. The minimal width of the slot is limited to 150 nm by the resolution of the deep-UV lithography. To narrow down the slot width, the waveguides were uniformly coated using atomic layer deposition (ALD) with 58 nm Al_2O_3, which has a low SERS background [70]. After ALD, gold waveguides were defined using photolithography and a 2 nm titanium adhesion layer and a 120 nm thick layer of sputtered gold were deposited. The nanoplasmonic slot waveguides were characterized with scanning electron microscopy and the gap size was determined to be 15 $\pm$ 0.5 nm. To prove the non-resonant enhancement of the nanoplasmonic slot waveguides, we rely on the simulation results [79, 159], supported by the experimental measurements of the SERS signal at two different laser excitation wavelengths (632 and 785 nm), as reported in [79]. Numerical simulations predict the maximum SERS enhancement factor of the nanoplasmonic slot waveguide for a single molecule to be 1.5 x 10^7 [79].

5.2.3 Acquisition of SERS spectra of nitrothiophenol

Both SERS substrates were functionalized with a self-assembled monolayer of nitrothiophenol (NTP) that selectively binds to the gold via gold-thiol

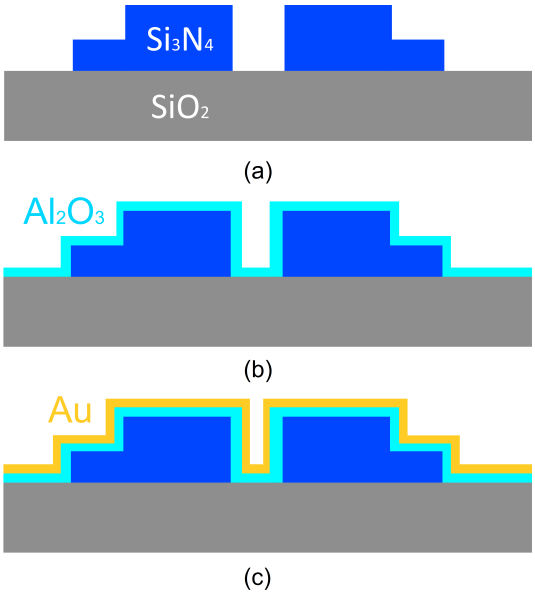

Figure 5.6: Fabrication of a nanoplasmonic slot waveguide. (a) Fabrication of the Si_3N_4 slot waveguides. (b) Atomic layer deposition of Al_2O_3. (c) Gold deposition.

bond, as described in detail in Ref. [79]. In short, the SERS substrates were cleaned with acetone, isopropyl alcohol and deionized (DI) water, and then dried with a N_2 gun. After oxygen plasma treatment, they were immersed overnight in 1 mM NTP solution in ethanol, and then rinsed with ethanol to remove non-bound NTP.

SERS spectra of the two substrates were acquired on a WITec Alpha 300 R+ confocal Raman microscope equipped with a -65 °C to -70 °C cooled CCD camera (Andor iDus 401BR-DD) and a 785 nm diode laser (Toptica, XTRA II). Stokes scattered light was collected by a 100 μm diameter multimode fiber and fed to the spectrometer, which used a 600 l/mm grating to diffract the Stokes scattered light on the spectral camera. All lines of the CCD camera were read out using full vertical binning, where the charges were summed across each column and reported out as a single pixel. The vertical shift (i.e. the time taken to shift the frame vertically by one row) was 16.25 μs and the horizontal shift speed was 0.033 MHz. For gold nanodomes, a 300 μW laser power before the microscope objective and a Nikon PlanFluor 10x/0.3 objective were used to acquire spectra on a spatially distributed map of 10x10 pixels in a 20x20 μm area with an integration time of 0.13 s on each point to avoid signal degradation upon

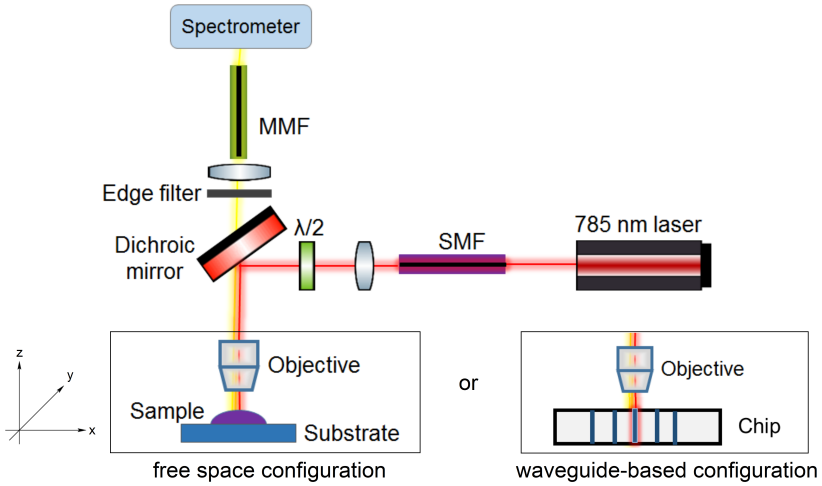

Figure 5.7: Schematic of an optical setup used to measure the SERS spectra. Gold nanodomes were measured in a conventional free-space configuration, whereas in the case of the nanoplasmonic slot waveguides, the microscope objective was used to couple the light to the waveguide and then collect the SERS signal in back-reflection.

laser illumination. Each trace represents a median spectrum of one map, so that half of all the spectra have lower and half higher values compared to the median spectrum at a certain Raman shift. To acquire the SERS spectra of the nanoplasmonic slot waveguide on the confocal microscope, the sample was positioned vertically and end-fire coupled, as shown in Figure 5.7 and explained in more detail in Ref. [79]. The polarization of the 785 nm excitation beam is set to the TE mode of the waveguide and a Zeiss 100x/0.9 EC Epiplan NEOFLUAR:∞/0 objective is used to couple the light into the waveguide with the laser power of 350 μW measured before the microscope objective. The integration time is set to 1 s. The SERS signal is collected in back-reflection using the same objective. The objective and chip are aligned with 100 nm accuracy based on a maximum intensity of the waveguide Raman spectrum. Simultaneously, maximum light scattering along the waveguide is observed from a camera imaging the top surface of the chip.

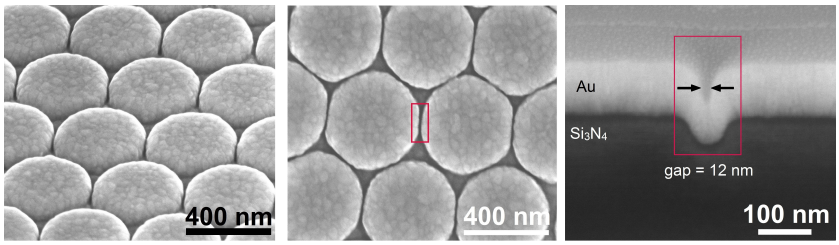

Figure 5.8: SEM images of gold nanodomes. (a) Tilted view. (b) Top-down view. (c) Cross-section of a nanodome-patterned chip with a 12 nm wide gap between nanodomes.

5.2.4 Comparison of free-space excited gold nanodomes and waveguide-based nanoplasmonic slot waveguide

In this section, we examine fabrication processes and the SERS performance of gold nanodomes, where the signal is excited and collected in free space, and of the waveguide-based nanoplasmonic slot waveguide.

5.2.4.1 Scalability of the fabrication processes

The SEM images of the gold nanodomes are shown in Figure 5.8. The fabrication of gold nanodomes is simple and scalable. Many SERS substrates are fabricated using electron beam lithography, however this resource-intensive and time-consuming method is primarily used for prototyping and is not often used in industrial scale fabrication. On the other hand, the fabrication process based on nanosphere lithography is easily implemented in a mass scale production, making gold nanodomes interesting for industrial applications.

Figure 5.9 shows the schematic and the SEM images of the nanoplasmonic slot waveguide. The nanoplasmonic slot waveguide provides high SERS enhancements that outperform previously developed waveguide-based SERS platforms, such as integrated bowties [77, 154] and integrated nanotriangles [78]. In addition to high SERS enhancement, the nanoplasmonic slot waveguides are fabricated using a combination of atomic layer deposition and deep-UV photolithography, enabling mass scale manufacturing. Both gold nanodomes and nanoplasmonic slot waveguides are therefore fabricated using widely available, mass-scalable fabrication methods that make them

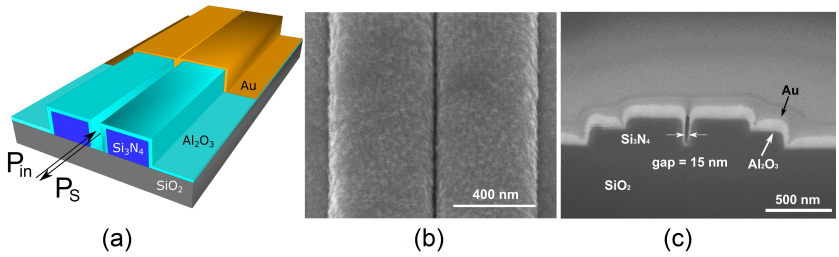

Figure 5.9: Nanoplasmonic slot waveguide. (a) Schematic showing that the input and Stokes powers are guided by the waveguide. (b) SEM image of the gold-covered slot in top view. (c) Cross-section of a nanoplasmonic slot waveguide with a gap of 15 nm.

interesting for industrial applications.

5.2.4.2 SERS performance comparison

To compare the SERS performance of gold nanodomes and nanoplasmonic slot waveguides, we used a monolayer of nitrothiophenol (NTP). NTP shows prominent SERS peaks at the Raman shifts of 1110, 1339 and 1573 cm^{-1} that correspond to C-S stretching, symmetric nitro stretching, and phenyl ring modes of the nitrothiophenol molecule respectively [160]. We used the integrated counts of the 1339 cm^{-1} NTP mode as a metric of the SERS signal and the SERS background. We additionally assessed the coefficient of variation on the SERS signal across a single chip on the gold nanodomes to be 6-7%, as previously reported [49]. For the metal slot waveguides, this coefficient cannot be defined since we are exciting the SERS response through a single access waveguide.

We acquired the SERS spectra of the gold nanodomes and nanoplasmonic slot waveguides using different excitation laser powers and integration times. These parameters were optimized so that no photoinduced reduction of NTP to dimercaptoazobenzene was observed, since these chemical changes would affect the SERS signal strength of the 1339 cm^{-1} mode of NTP [44]. The spectra are shown in Figure 5.10. The first step to consistent comparison of the SERS signals was therefore to normalize the SERS signal strength on the integration time. Since the signal increases linearly with the integration time, we simply normalized the SERS signal strength to an integration time of 1 s. To include the effect of the different excitation laser powers, we calculate the ratio of total collected power P_S at different Raman

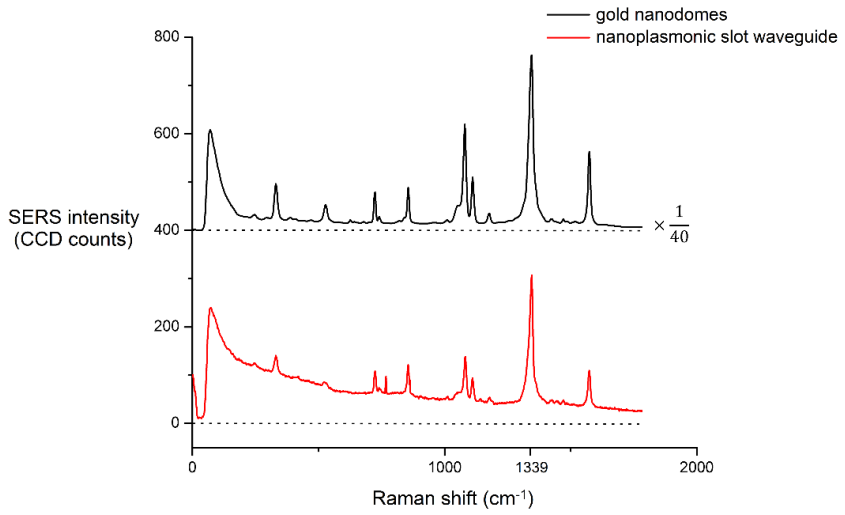

Figure 5.10: SERS spectra of the NTP monolayer acquired on gold nanodomes and on the nanoplasmonic slot waveguide. The spectrum on the gold nanodomes was obtained using a laser power of 300 μW and an integration time of 0.13 s. The spectrum on the nanoplasmonic slot waveguide was obtained using a laser power of 350 μW and an integration time of 10 s. The SERS spectrum on the nanodomes was divided by a factor of 40 to allow better visualization. We subtracted the dark counts, but not the SERS background of the spectra. The spectra are offset on the y axis for clarity and the dashed line represents the zero line of each spectrum.

shifts over input power P_{in} as:

$$\eta = \frac{P_S}{P_{in}} \tag{5.1}$$

Here, P_{in} is the laser power that is used to excite the SERS response of our analyte. In the case of nanodomes, all the free-space laser power is used to excite the SERS response of our analyte. P_{in} is therefore the laser power coming out of the microscope objective, whereas in the waveguide-based SERS platforms we define P_{in} as the laser power guided in the waveguide to the plasmonic structure, as shown in Figure 5.9(a). P_S is the power of the SERS scattered photons, in our case at the 1339 cm^{-1} peak. To convert the measured CCD counts to P_S, we use the formula:

$$P_S = F_{ph} h(\nu_0 - \nu_S) T_m^{-1} \tag{5.2}$$

For the 1339 cm^{-1} NTP peak excited at 785 nm, the Stokes frequency $(\nu_0 - \nu_S)$ equals 342 THz and the transmission of the microscope T_m is 0.61 at the 870 nm Stokes shifted wavelength. For the specific case of our spectrometer with settings as described in 5.2.3, the photon flux F_{ph} equals 5.9 times the number of counts in the Raman spectrum. The same calculation was also applied to calculate the SERS background signal. In Figure 5.11, the performance of the gold nanodomes and nanoplasmonic slot waveguides is compared in terms of the SERS signal strength and the SERS background. We additionally included the SERS performances of integrated bowties [77] and integrated nanotriangles [78] in the graph to highlight the progress that has been achieved in the last years in the field of waveguide-based SERS platforms. We see that the free-space excited gold nanodomes offer very high SERS enhancements, however, their high background contribution limits their SERS performance. On the other hand, the nanoplasmonic slot waveguides provide lower SERS enhancements, yet their SERS background is reduced compared to that of the nanodomes.

SERS background remains insufficiently understood and in the last years several new models were proposed to describe its origins [161–164]. Exact identification of the origin of the SERS background in gold nanodomes and nanoplasmonic slot waveguides was shown to be a difficult task that is beyond the scope of this thesis work. However, we try to narrow down the possible origins of the SERS background. The SERS background has been linked to the strength of the localized surface plasmons, the identity of the adsorbate and adsorbate coverage [162]. In our case, we use the same adsorbate (NTP) under identical labelling conditions to characterize both

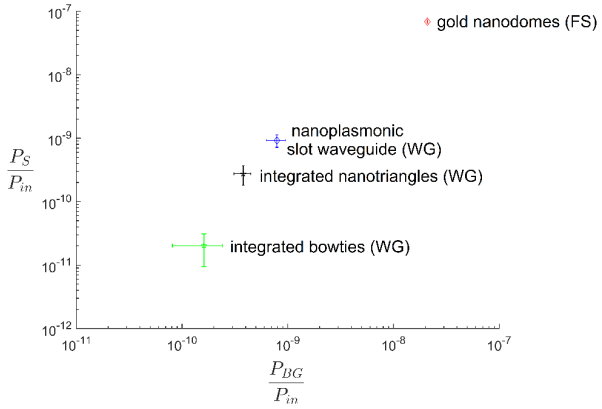

Figure 5.11: Comparison of SERS background power P_{BG} (x axis) and SERS scattered power P_S (y axis) of different SERS platforms. Both parameters are normalized on the input power and the integration time. FS indicates free-space and WG waveguide-based excitation and collection of the SERS signal.

nanodomes and nanoplasmonic slot waveguides. Furthermore, we always use newly fabricated SERS substrates to avoid any contaminants from previous labelings. We thus argue that the differences in the SERS background probably do not arise from the adsorbate itself or from the contamination of our samples. Conversely, the effects of plasmons on the SERS background are harder to evaluate. We fabricate the structures using the same gold deposition technique, indicating that the differences in the SERS background do not originate from differences in gold deposition. SERS enhancement is then achieved via localized surface-plasmon resonance in gold nanodomes [49] and via propagating surface plasmon polariton in the nanoplasmonic slot waveguide [79], which might at least in part cause differences in SERS background. Additional differences in this background might also arise from the two different ways of exciting the SERS response, that is via free-space and waveguide-based excitation for the gold nanodomes and nanoplasmonic slot waveguides, respectively. In the case of the nanoplasmonic slot waveguide, the silicon nitride waveguides might provide some additional contribution to the SERS background.

To compare the different SERS platforms, we consider both the SERS enhancement and SERS background. We propose signal-to-background ratio (SBR) and signal-to-noise ratio (SNR) as relevant parameters for comparing the SERS performance of different platforms. In case of strong SERS signals compared to background, the accuracy of SERS signal analysis is limited by

the imperfect background subtraction, since the background needs to be estimated from algorithmic extrapolation or from separate measurements [165]. In this case, we can use SBR as metric to evaluate the SERS performance:

$$SBR = \frac{P_S}{P_{BG}} = \frac{\frac{P_S}{P_{in}}}{\frac{P_B G}{P_{in}}} \tag{5.3}$$

The SBR-values of the different SERS platforms are shown in Table 5.1. We see that the nanoplasmonic slot waveguide offers a substantial improvement compared to other waveguide-based SERS platforms as it provides a more than 10-times higher SBR than integrated bowties and a 60 % higher SBR than integrated nanotriangles. The nanoplasmonic slot waveguide therefore approaches the SBR of the free-space excited gold nanodomes, providing only 3-times lower SBR than gold nanodomes.

SERS platform	SBR	SNR
Gold nanodomes (FS)	3.28	3x10^4
Integrated bowties (WG)	0.12	10^2
Integrated nanotriangles (WG)	0.72	10^3
Nanoplasmonic slot waveguide (WG)	1.16	2x10^3

Table 5.1: SBR and SNR values at P_{in} of 1 mW and t of 1 s for different SERS platforms evaluated based on the 1339 cm^{-1} mode of a NTP monolayer. If we use another input power or integration time, the absolute value of the SNR will change, but the relative SNR of different SERS platforms will remain the same. FS indicates free-space and WG waveguide-based excitation and collection of the SERS signal. Here, only the shot noise contribution from the background is considered (as will be relevant when looking for weaker peaks than the 1339 cm^{-1} mode).

On the other hand, when the photon number of the total signal within the integration time is below critical level, the accuracy of SERS signal analysis is not limited by the imperfect accuracy of the background subtraction but rather by shot noise. SNR then provides a more relevant metric for the SERS performance of different SERS platforms [165]. The noise N (shot noise) is proportional to the square root of the sum of the SERS peak and the SERS background signal. In the case of low SERS signals, the main contribution to the noise N (being the rms value of the signal fluctuation) is therefore from the background signal:

$$N = \sqrt{\frac{P_{BG} t}{h\nu}} \tag{5.4}$$

The SNR is then defined as:

$$SNR = \frac{\frac{P_S t}{h\nu}}{\sqrt{\frac{P_{BG} t}{h\nu}}} = \frac{\frac{P_S}{P_{in}}}{\sqrt{\frac{P_{BG}}{P_{in}}}} \sqrt{\frac{P_{in} t}{h\nu}} \tag{5.5}$$

We list the SNR of the different SERS platforms in Table 5.1. As the SNR also depends on the square root of the input power P_{in} and integration time t, we set the input power at 1 mW and the integration time to 1 s to be able to perform a relative comparison of the SNR of the different SERS platforms. If we use another input power, the absolute value of SNR will change, but the relative SNR of different SERS platforms will remain the same. We see that the nanoplasmonic slot waveguides provide significant SNR improvements compared to the other waveguide-based SERS platforms. Their SNR ratio is 20-times better than that of integrated bowties and 2-times better compared to integrated nanotriangles. Nevertheless, free-space excited gold nanodomes still outperform the nanoplasmonic slot waveguide with a 15-times higher SNR.

Besides the improved SBR, the nanoplasmonic slot waveguide also offers non-resonant SERS enhancement, making SERS enhancement independent of excited and scattered wavelengths, which offers an advantage compared to the highly resonant gold nanodomes. Moreover, the waveguide-based SERS platform shows great potential for high-throughput SERS assays on low sampling volumes, especially relevant for the detection of biological molecules.

5.3 Hydrogen plasma cleaning of gold plasmonic nanostructures for better reproducibility of SERS spectra

SERS is often used for the detection of self-assembled monolayers that attach to the gold surface of plasmonic nanostructures via gold-sulfur bonds. However, due to the less efficient fabrication process of the waveguide-based SERS platforms compared to the gold nanodomes, we explore the possibilities to reuse SERS substrates. Oxygen plasma is typically used to remove self-assembled monolayers in order to clean and reuse the plasmonic nanostructures for further SERS measurements. X-ray photoelectron spectroscopy, scanning tunneling microscopy, ellipsometry, and contact angle

measurements were used to show that oxygen plasma cleaning contaminates the gold surface with oxidized sulfur species [166]. Hydrogen plasma has thus been proposed as an alternative method to remove SAMs on gold nanostructures, as it produces a sulfur-free gold surface [166]. We therefore examine hydrogen plasma cleaning of SERS substrates as an alternative to oxygen plasma cleaning, and show that hydrogen plasma cleaning leads to much more reproducible SERS spectra. The text of this section has been adapted from the conference paper [150].

5.3.1 Experimental design

In this section, we examine the effects of oxygen or hydrogen plasma to remove the SAM from gold nanostructures, on SERS spectra. We perform these experiments on gold nanodomes, SERS substrates that provide high SERS enhancements and are easy to fabricate [49]. To make the SAM, we use the peptide NH_2-CALNN(CN-F)S(CN-F)GGGGVRGNFSF-COOH, described in more detail in Chapter 4. In this peptide, the SERS peaks originate from the aromatic amino acids phenylalanine (F) and cyano-phenylalanine (CN-F). We observe the SERS peak of F at 1003 cm^{-1}, and the peak of CN-F at 1180 cm^{-1}. The possible contaminants on the gold surface after plasma cleaning do not provide distinguishable SERS peaks but rather influence the SERS background signal.

We examined three different samples. In the first sample, a newly fabricated SERS substrate was labeled with the SAM. In the second and third samples, we labeled the SERS substrate with the SAM, then cleaned it for 2 minutes with hydrogen or oxygen plasma respectively, and relabeled the substrate with the same SAM. To assess the effects of oxygen and hydrogen plasma cleaning on the gold SERS substrates, we recorded the SERS spectra of the peptide and calculated the integrated counts of the SERS background signal.

5.3.2 Results and Discussion

In Figures 5.12 and 5.13, we show the SERS spectra of the three different samples. Figure 5.12 shows the background-subtracted SERS spectra acquired with identical acquisition conditions, namely identical laser power, laser spot size and integration time. The SERS peaks of the samples cleaned with hydrogen plasma have prominently lower SERS peak intensities com-

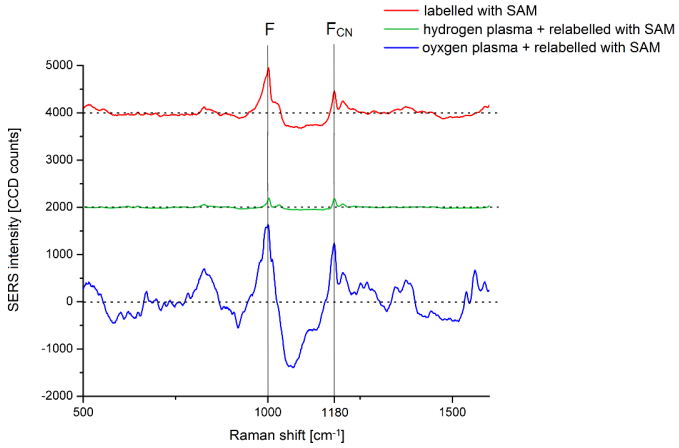

Figure 5.12: Background-subtracted SERS spectra of the samples labeled with the SAM (red), cleaned with hydrogen plasma and then relabeled with the SAM (green) or cleaned with oxygen plasma and relabeled with the SAM (blue). The spectra were acquired with identical acquisition conditions. The dashed horizontal lines represent the zero line of each spectrum, whereas the full vertical lines mark the SERS peaks of the aromatic amino acids.

pared to the other two samples. In addition, we plot the normalized SERS spectra of the three samples in Figure 5.13, where the spectra are normalized on their respective highest peak intensities. We see that the SERS background of the samples cleaned with oxygen plasma is much more prominent, so that even the higher SERS peaks are not easily distinguishable from the SERS background.

We then integrated the SERS background signal counts for the Raman shifts in the range from 500 to 1500 cm^{-1} to evaluate the effects of oxygen or hydrogen plasma cleaning of the gold SERS substrates (Figure 5.14). We notice that reusing the SERS substrates after cleaning with oxygen plasma increases their SERS background signal, and even more prominently, increases the variability of the background signal. On the other hand, hydrogen plasma cleaning offers a much more reproducible SERS background, which can be of crucial importance when subtracting the SERS background to detect (weaker) SERS peaks.

Next, we examined the F/CN-F peak intensities for the three different samples (Figure 5.15). As explained above, the remaining contaminants will only affect the SERS background and will not result in SERS peaks. However, to quantify the SERS peaks of the Raman analytes of interest,

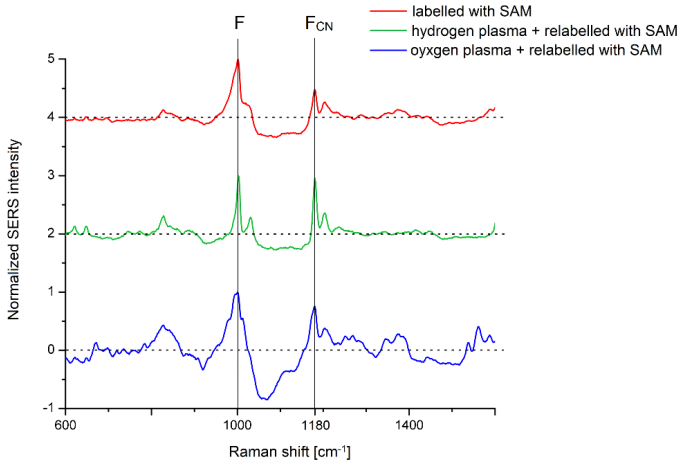

Figure 5.13: SERS spectra from 5.12, normalized on their respective highest peak intensities. The dashed horizontal lines represent the zero line of each spectrum, whereas the full vertical lines mark the SERS peaks of the aromatic amino acids.

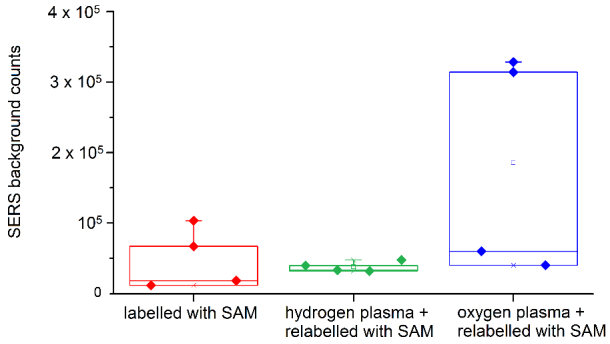

Figure 5.14: SERS background counts integrated between 500 and 1500 cm^{-1} for the samples labeled with the SAM (red), cleaned with hydrogen plasma and then relabeled with the SAM (green) or cleaned with oxygen plasma and relabeled with the SAM (blue). The points represent the averaged values on individual samples, whereas the box plot represents the statistical distribution of the points.

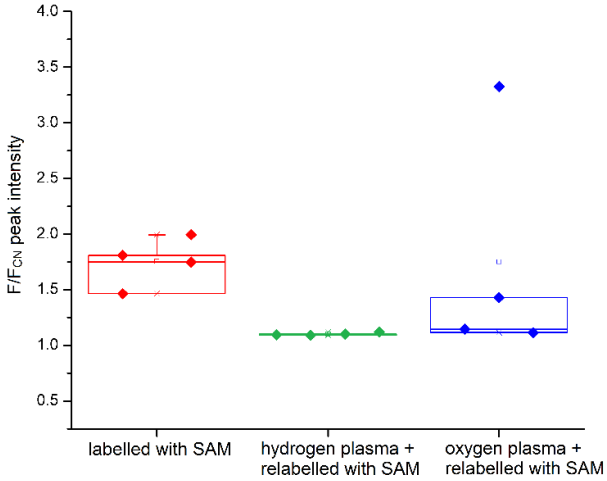

Figure 5.15: F/CN-F peak intensities for the samples labeled with the SAM (red), cleaned with hydrogen plasma and then relabeled with the SAM (green) or cleaned with oxygen plasma and relabeled with the SAM (blue). The points represent the averaged values on individual samples, whereas the box plot represents the statistical distribution of the points.

we rely on accurate subtraction of the SERS background. Since SERS background reproducibility is negatively affected by oxygen plasma cleaning, the background subtraction therefore becomes more unreliable, additionally resulting in an increased variability of the quantification of the SERS peaks of the Raman analytes of interest, in our case the peptide.

We show scanning electron microscopy images of the three different samples in Figure 5.16. From Figure 5.16(c) it is clear that hydrogen plasma cleaning can have a negative influence on the gold nanodome SERS substrate. Indeed, we notice the appearance of circular defects on the gold nanodomes fabricated on a silicon nitride wafer. We have not found a record of similar defects in literature, but assume that these defects are specific for the silicon nitride and the gold used to fabricate the gold nanodomes. With the optimization of the hydrogen plasma parameters, specifically the plasma power, it is however possible to avoid such circular defects from forming, as shown in Figure 5.16(c) and (d).

We have demonstrated that hydrogen plasma cleaning of self-assembled monolayers from gold nanostructures results in more reproducible SERS background spectra than when using oxygen plasma cleaning. Consequently, SERS peak characterization of Raman analytes is more reliable due to the

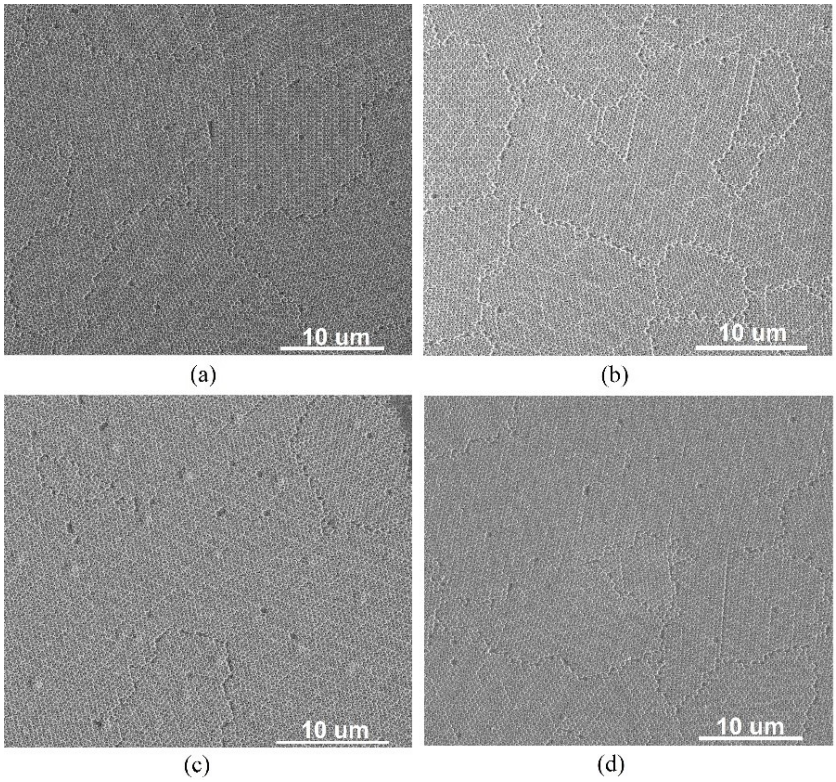

Figure 5.16: Scanning electron microscopy (SEM) images of the samples labeled with the SAM (a), cleaned with oxygen plasma and then relabeled with the SAM (b) or cleaned with hydrogen plasma with different plasma powers and relabeled with the SAM (c, d).

more reproducible background. We furthermore discovered that using hydrogen plasma to clean gold nanodomes on silicon nitride can introduce some additional surface defects, which can however be avoided by optimizing the parameters of the hydrogen plasma process.

6

Free-space and waveguide-based SERS detection of protease activity

6.1 Introduction

Our group previously showed SERS-based detection of protease activity using a model protease (trypsin) in a microscope-based free-space measurement using gold nanodomes [49]. In that experiment, all the aromatic amino acids that were used as Raman reporters in the peptide substrate were natural aromatics. However, there are only three natural aromatics, which limits our capabilities for multiplexing. In addition, these aromatics do not have very high Raman cross-sections, making the SERS signal they deliver rather low. Therefore, we explored selected non-natural aromatic amino acids as described in Chapter 4.

We took on the synthesis of several peptide substrates for both trypsin and endoproteinase GluC (Table 4.2). To demonstrate SERS-based detection of protease activity, we used the peptide NH_2-CALNN(CN-F)GSG(CN-F)GGGGV**R**-GNFSF-COOH as substrate for trypsin, where trypsin cleaves the peptide at the carboxyl side of the arginine (R). Similarly, NH_2-CALNN (CN-F)S(CN-F)GGGGNN**E**-SYSYH-COOH was designed as a substrate

for endoproteinase GluC, where GluC cleaves the peptide at the carboxyl side of the glutamic acid (E).

In this chapter, we describe free-space SERS detection of trypsin activity with a peptide substrate containing non-natural aromatics, done on a gold nanodome SERS platform. We also discuss our efforts towards SERS detection of the proteolytic activity of endoproteinase GluC. Next, we assess waveguide-based SERS detection of trypsin activity using nanoplasmonic slot waveguides. Additionally, we underline the advantages and challenges that we need to consider when translating protease activity detection from a free-space to a waveguide-based SERS platform.

6.2 Using non-natural aromatics for free-space SERS detection of trypsin activity

To check trypsin activity using SERS, we use the tryptic peptide substrate with the amino acid sequence NH_2-CALNN(CN-F)GSG(CN-F)GGGGV**R**-GNFSF-COOH. Although this peptide was designed such that it should be cleaved by trypsin, leading to a decrease in the corresponding SERS peak, we first verified this in the following experiments:

1. **Acquisition of SERS spectra of RP-HPLC separated peptide fragments generated by a trypsin cleavage experiment in solution.** First, we perform the cleavage of the peptide substrate by its protease in solution and then use RP-HPLC to separate the generated peptide fragments. Ideally, after a complete and specific cleavage, we would just see two fractions corresponding to the two cleaved peptide fragments. If the cleavage is inefficient, we can additionally still see peaks in the chromatogram corresponding to the uncleaved peptide. We then label gold nanodomes and record SERS spectra of each collected HPLC fraction.

2. **Labelling gold nanodomes with the solution from a bulk trypsin cleavage experiment, followed by the acquisition of the SERS spectra.** In the second experiment, we again perform bulk cleavage and then immediately label gold nanodomes with the solution containing peptide fragments and the protease. In principle, only the peptide fragment containing the N-terminal cysteine should attach to the gold surface of the SERS substrate via a gold-sulfur bond. We

therefore expect to only see the SERS peak of the aromatic amino acid that we use for normalization, here cyano-phenylalanine.

3. **Labelling gold nanodomes with the intact peptide substrate and performing trypsin cleavage directly on the SERS chip.** Lastly, we check if the peptide can also be cleaved when attached to the gold surface of the SERS substrate. Therefore, gold nanodomes are first labelled with the peptide, such that a peptide monolayer forms on the gold surface. This monolayer must provide cleavage sites that are accessible for the protease. Additionally, the gaps of the SERS structures need to be sufficiently big such that they remain accessible to the protease that needs to diffuse to the peptide monolayer in the gaps, where the SERS enhancements are the highest.

6.2.1 Acquisition of SERS spectra of RP-HPLC separated peptide fragments from a bulk trypsin cleavage experiment

We performed bulk trypsin cleavage of a peptide substrate, separated the peptide fractions by RP-HPLC, labelled them on the gold nanodomes and collected their SERS spectra.

First, trypsin was dissolved in 50 mM ammonium bicarbonate (ABC) buffer (pH = 7.8) to a concentration of 5 μg/ml (= 0.2μM). In all the subsequent experiments, the same trypsin concentration was used. Trypsin solution was warmed to 37°C, which is the optimal working temperature for trypsin. The lyophilized peptide was in the meantime first dissolved in DMF at a concentration of 25 μg/μl and then added to the trypsin solution in the ABC buffer to a final peptide concentration of 100 μg/ml and left to incubate for an hour at 37°C. We then separated the peptide solution via RP-HPLC (Figures 6.1 and 6.2) and analyzed the collected fractions by means of mass spectrometry to determine the masses of the prominent HPLC peaks, and thus to conclude which peptide fraction they represent.

In the chromatogram shown in Figure 6.1, we see a prominent peak at an elution time of 39.5 min with a mass corresponding to that of the intact peptide monomer. We additionally see a smaller peak eluting around 43 min. MALDI-MS analysis indicate that the peptides in this fraction had the same mass as in the case of the monomer. However it is more likely that this peptide is actually a dimer – as it eluted at a later time point and is thus more hydrophobic – that broke down into two monomers in the mass spectrometer ionization chamber. The peptides we use start with a cysteine and two such

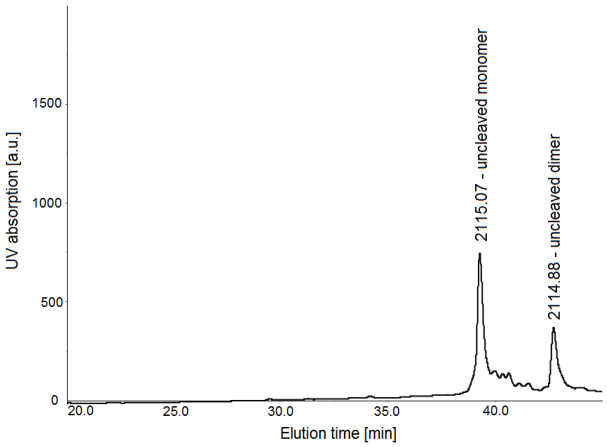

Figure 6.1: RP-HPLC chromatogram of the intact peptide substrate for trypsin. The measured mass along with the identified peptide fraction is written above each HPLC peak.

cysteines (of thus two individual peptides) can form a sulfur bridge under oxidizing conditions. It has previously been shown that the formation of dimers does not drastically reduce the ability of the peptides to bond to the gold surface that we wish to use as SERS substrates [7].

Figure 6.2 shows the RP-HPLC analysis of the peptide substrate digested by trypsin. Here, we want to primarily establish that trypsin cleaves its substrate specifically, i.e. only at the arginine (R) cleavage site. Furthermore, we want to determine how long the incubation needs to be for complete peptide cleavage in solution. Previous experiments suggested that trypsin cleavage is quite fast and we could expect to see full peptide cleavage after about one hour of incubation [49]. In Figure 6.2, we see that the peaks of peptides eluting at 39.5 and 43 min disappear, suggesting that the peptide had been completely digested. Further, two prominent peaks now appear at 33 and 37 min. The masses of the peptides in these peaks correspond to the adducts of the long peptide fragments of the cleaved monomer and the cleaved dimer, namely NH_2-CALNN(CN-F)GSG(CN-F)GGGGV**R**-COOH, as expected. Adducts are a common occurrence in mass spectroscopy analysis, and stem from the fact that the peptide fragment binds to a sodium or potassium ion, resulting in a corresponding increase in the mass of the peptide ion.

After establishing that the peptide was cleaved specifically and fully by trypsin, we labelled the gold nanodomes with the collected HPLC fractions

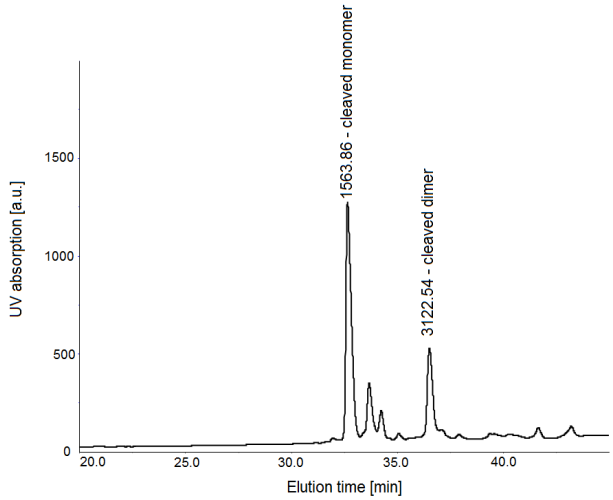

Figure 6.2: RP-HPLC chromatogram of the trypsin-digested peptide. The measured mass along with the identified peptide fraction is written above each HPLC peak.

in order to collect their SERS spectra. The gold nanodomes were cleaned with acetone, isopropyl alcohol and deionized (DI) water, and dried with a N_2 gun. After placing the gold nanodomes in oxygen plasma for 2 min, the nanodomes were immersed overnight in the peptide solution. Then, they were rinsed with DI water to remove peptides that did not covalently bound to the gold surface. The samples were placed in a Petri dish filled with 3 ml of 50 mM ammonium bicarbonate buffer (pH 7.8). The SERS spectra of the peptides were acquired with the WiTec confocal Raman microscope, described in Chapter 5. For gold nanodomes, a 1 mW laser power before the microscope objective and a 40x/0.5 Zeiss water immersion objective were used to acquire spectra on a spatially distributed map of 7x7 pixels in a 40x40 μm area with an integration time of 3 s on each point to avoid signal degradation upon laser illumination.

Starting from the 7x7 individual spectra, cosmic rays were removed using WiTec Project Four. The data were then exported to Matlab and aberrant spectra were discarded using a variance-based filter. Then, the background of each individual spectrum was subtracted using a high-pass filter. All free-space SERS spectra plotted in this chapter are the average spectra of one map of 7x7 measurements. Where applicable, peak intensities were calculated by integrating the peak counts at their respective positions and subtracting the background with a linear fit for the individual spectra. In Figure 6.3, the SERS spectra of different peptides or peptide fragments

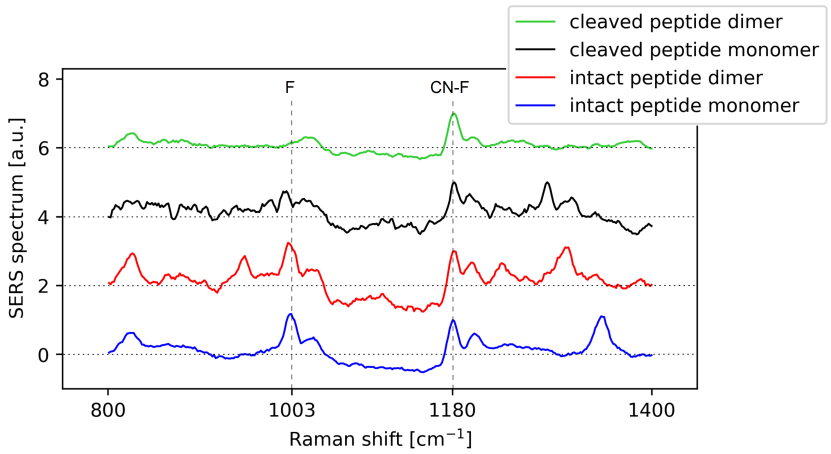

Figure 6.3: SERS spectra of the RP-HPLC separated peptides from a bulk trypsin cleavage experiment. The spectra are normalized on the CN-F maximum peak intensity for easier comparison and offset on the y axis. The horizontal lines represent the zero of each spectrum. The two vertical lines represent the positions of the characteristic SERS peaks of the phenylalanine (F) and cyano-phenylalanine (CN-F). After trypsin digestion, a complete disappearance of the SERS peak of phenylalanine F is evident, as expected.

are plotted, normalized on the CN-F maximum peak intensity.

We found that the gold nanodomes labelled with both the intact peptide monomer and dimer display the two characteristic SERS peaks, one at 1003 cm^{-1} corresponding to phenylalanine (F) and another at 1180 cm^{-1} that can be ascribed to cyano-phenylalanine (CN-F). As assumed above, also the peptide dimer seems to efficiently attach to the gold SERS substrate. After trypsin cleavage of the peptide substrate, the F peak completely disappears, as expected.

In summary, we have proven that trypsin efficiently and specifically cleaves the peptide substrate we designed. The resulting peptide fragments show the disappearance of their corresponding SERS peak as expected. In the next section, we will examine if the same behavior of the SERS peaks is found when no HPLC is used for separating the different fractions of the digested peptide. This is especially important when there are small amounts of contaminants in the peptide solution that could mask the peptides' SERS peak behavior, which we use as a metric for trypsin activity.

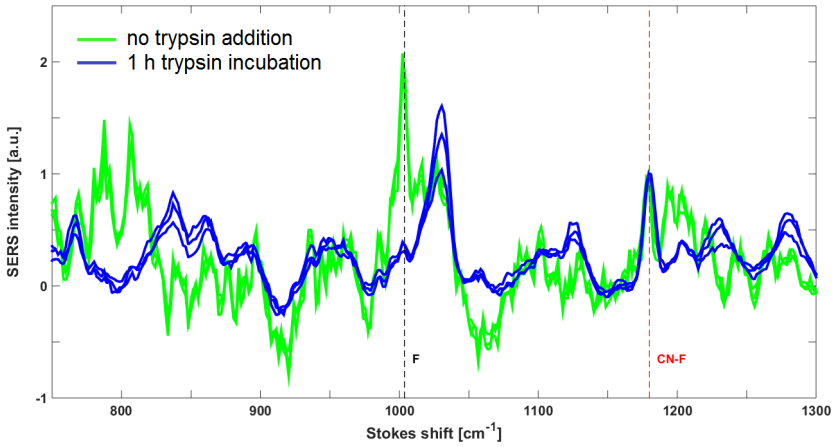

Figure 6.4: SERS spectra of the intact peptide (green) and of the cleavage solution after 1 h of incubating the peptide with trypsin (blue). The three spectra for each condition come from three different gold nanodome samples, all labelled under the same conditions. All spectra are normalized on the CN-F peak at 1180 cm^{-1}.

6.2.2 Labelling gold nanodomes with the solution from a bulk trypsin cleavage experiment, followed by acquisition of SERS spectra

As another control experiment, we again performed bulk cleavage of the peptide with trypsin, exactly as described in the previous section. We then immediately labelled the gold nanodomes with the cleavage solution containing all peptide fragments. In principle, only the long peptide fragment should be able to bind to the gold surface via a sulfur-gold bond via its N-terminal cysteine. We expect that the short peptide fragment, NH_2-GNFSF-COOH, would be washed away from the gold surface when rinsing the gold nanodomes after overnight labelling. We recorded SERS spectra from gold nanodomes labelled with the peptide solution using the same acquisition parameters as described in 6.2.1. The SERS spectra are shown in Figure 6.4 and were normalized on the CN-F peak at 1180 cm^{-1} for easier comparison.

We can see that the F peak disappears completely as expected after trypsin incubation, showing full cleavage of the peptide. To quantify this, we calculated the ratio of the SERS peak intensities as described in the previous chapter. We integrated the F and CN-F peak counts, and used the F/CN-F peak intensity ratio as a metric for the (efficiency of) trypsin cleavage, as plotted in Figure 6.5. As can be seen, due to the disappearance of the F peak,

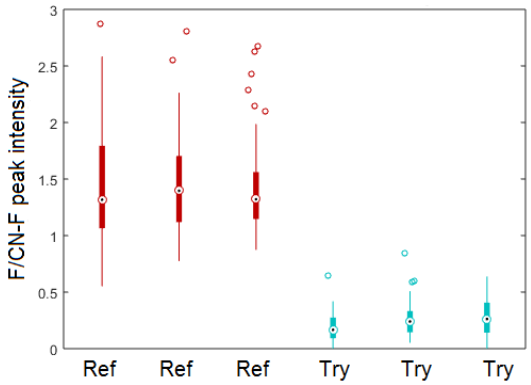

Figure 6.5: A box plot of F/CN-F peak intensities before (Ref) and after (Try) trypsin addition for the spectra shown in Figure 6.4. Each box plot corresponds to one SERS spectrum in the previous figure. We can see that the decrease of F/CN-F peak intensity corresponds to the trypsin cleavage of the peptide.

the F/CN-F peak intensity is greatly reduced upon trypsin digestion. Based on the experiments in the previous section showing complete cleavage of the peptide substrate, the small remaining contribution of the F peak after trypsin incubation can be ascribed to the data analysis method used and not to the contribution of the remains of uncleaved peptide.

6.2.3 Labelling gold nanodomes with intact peptide substrate and performing trypsin cleavage directly on the SERS chip

We have so far established that trypsin efficiently and specifically cleaves a peptide substrate. Furthermore, we have shown that when labelling the gold nanodomes with the entire cleavage solution, we clearly see the disappearance of the F peak, indicating the trypsin activity.

However, we still have to demonstrate that trypsin can also cleave peptides that are attached to the gold surface of the SERS nanostructures. This is not evident as the peptide might self-assemble on the gold surface such that its cleavage site would not be accessible for trypsin. Moreover, trypsin might not be able to enter the small nanodome gaps where the SERS signal is the most enhanced [48, 49]. In the previous chapter we established that the gold nanodomes have gaps of around 12 nm. Trypsin with a molecular mass of 23.3 kDa has an effective radius of 2-3 nm [167]. The accessibility

of the gaps for trypsin is not only limited by the gaps' relatively small size, but also by diffusion on which we rely to transport trypsin to these gaps.

In this last experiment we thus wanted to establish if trypsin can efficiently cleave peptides that are self-assembled on the gold surface of the SERS substrate. To label the gold nanodomes with the intact peptide, the lyophilized peptide was dissolved in DMF (at 25 μg/ml). We then diluted this solution to a final peptide concentration of 100 μM in 10% acetonitrile in deionized water. After overnight labelling of the gold nanodomes, the samples were rinsed with deionized water. We incubated the peptide-labelled nanodomes in three conditions:

1. In ammonium bicarbonate buffer **without any trypsin** present, to serve as a reference measurement.

2. **With trypsin** dissolved in ammonium bicarbonate buffer at a concentration of 5 μg/ml. We only expect to observe trypsin activity and the corresponding F peak decrease in this condition.

3. In ammonium bicarbonate buffer **with inactivated trypsin**. Trypsin (at 5 μg/ml) was inactivated using the inhibitor phenylmethylsulfonyl fluoride (PMSF, 40 μg/ml) [168].

The samples were left to incubate in these three conditions for 1 hour, and then rinsed. The SERS spectra were acquired and analyzed as described in Section 6.2.1. In Figure 6.6, the SERS spectra before and after trypsin incubation are shown and it is evident that trypsin efficiently cleaved the peptide, resulting in a decrease in the intensity of the SERS peak of phenylalanine (F) at 1003 cm^{-1}. We also conclude that this partial F peak decrease can be ascribed to the limited accessibility of the nanodome gaps for trypsin, as established in [49].

The F/CN-F peak intensities were then calculated for all three different conditions (Figure 6.7). We notice that the 30 % decrease in the F/CN-F peak intensity ratio is only caused by trypsin cleavage of the peptide substrate, as no change in the SERS spectra is detected in the presence of inactivated trypsin or when no trypsin is added.

We can therefore conclude that the peptide substrate NH_2-CALNN(CN-F)GSG(CN-F)GGGGV**R**-GNFSF-COOH can be labelled on the gold nanodomes and cleaved efficiently by trypsin. However, due to the limited accessibility of the nanodome gaps for trypsin, this cleavage is not complete.

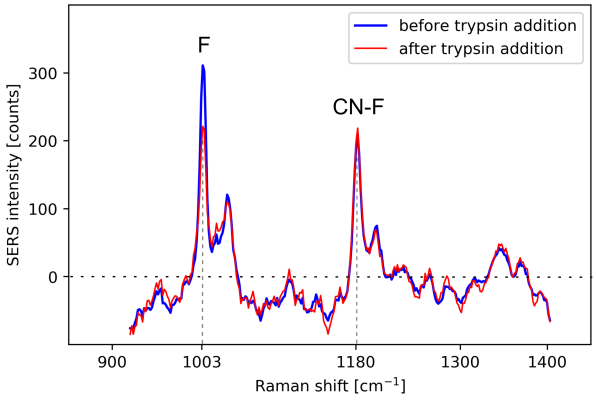

Figure 6.6: SERS spectra before and after trypsin addition. Addition of trypsin results in 30 % decrease in the intensity of the SERS peak of phenylalanine (F) at 1003 cm^{-1}.

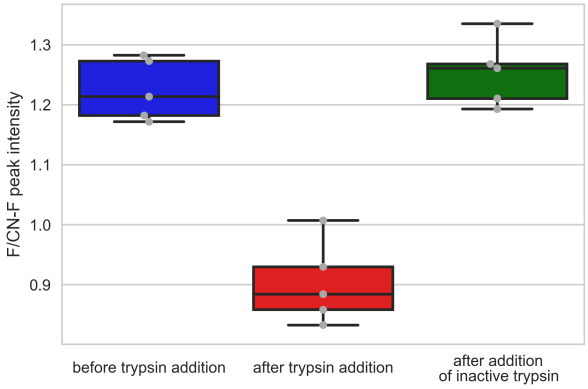

Figure 6.7: The box plot shows that the F/CN-F peak intensity ratio only decreases after trypsin addition. If no trypsin is added, or after the addition of inactive trypsin, there is no change in the F/CN-F peak intensity ratio. Gray dots represent individual measurements.

If we would find another SERS substrate with similarly high SERS enhancement, but bigger and therefore more accessible gaps, this problem could be circumvented.

Previously, the SERS-based detection of trypsin cleavage has been demonstrated using peptides with natural aromatics as Raman reporters [49]. In our work, we expanded the multiplexing possibilities of SERS based detection of protease activity by using non-natural aromatic amino acids. We can thus, in principle, evaluate the activities of several proteases simultaneously and additionally achieve stronger SERS signals than in the case of the natural aromatics.

6.3 Towards multiplexed SERS detection of protease activity

Due to the specificity of the Raman signals that are sometimes called "molecular fingerprints", we can use SERS for the simultaneous detection of two or more proteases as discussed in Chapter 4.

After developing a peptide substrate that can be used for the SERS detection of trypsin, we will in this section assess if we can also design a homologous peptide substrate for endoproteinase GluC. Following the template we used for the trypsin peptide, we designed a peptide sequence NH_2-CALNN(CN-F)S(CN-F)GGGGNNGGGGV**E**-SYSYH-COOH. Here, endoproteinase GluC recognizes the glutamic acid as its cleavage site. CN-F is used in both peptides as the normalization SERS peak as it should stay constant. On the other hand, phenylalanine (F) is here replaced by tyrosine (Y) to be able to distinguish between trypsin and GluC cleavage of peptides in a multiplexing experiment. However, the SERS signal of tyrosine is considerably weaker than that of phenylalanine. We have therefore not been able to obtain SERS results for the GluC peptide substrate. Nevertheless, we performed RP-HPLC and mass spectrometry investigation of this peptide, in order to establish if it is an efficient substrate for endoproteinase GluC. Further, we have also checked if trypsin did not cleave the endoproteinase GluC peptide substrate.

In future experiments however, the weak SERS signal strength of the tyrosine should be addressed. One could approach this with improved data analysis, while another option is to use another aromatic amino acid that gives a stronger SERS signal. The use of alternative SERS structures with

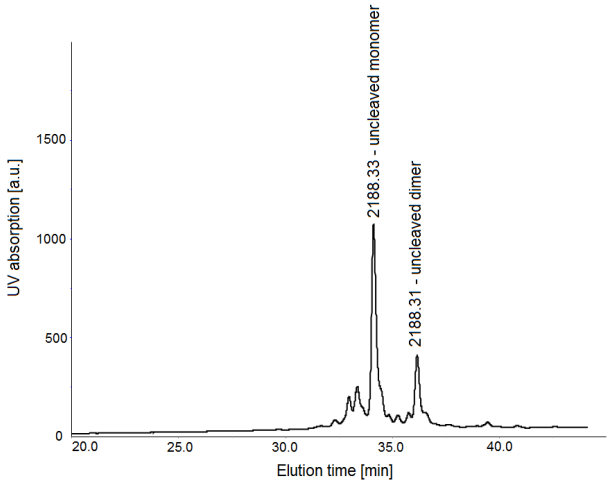

Figure 6.8: RP-HPLC chromatogram of the intact peptide substrate for endoproteinase GluC.

higher SERS enhancement can also be a solution.

6.3.1 Demonstrating the cleavage of the endoproteinase GluC peptide substrate

Bulk cleavage of the endoproteinase GluC peptide substrate was performed as for the trypsin peptide substrate (in Section 6.2.1) however, the incubation time was prolonged to 3 hours (instead of 1 hour). The RP-HPLC chromatograms of the intact and the cleaved peptide are shown in Figures 6.8 and 6.9, respectively.

The intact endoproteinase GluC peptide substrate is stable in ammonium bicarbonate buffer (pH = 7.8) and the formation of dimers as observed for the trypsin peptide substrate is evident. After three-hour incubation, we still observe a peak that corresponds to the intact peptide dimer, suggesting that endoproteinase GluC did not completely cleave the peptide. We furthermore notice the appearance of new peaks at earlier elution times. The intense peak at an elution time of 22 min corresponds to the short fragment of the digested peptide, namely NH_2-SYSYH-COOH. We also see the peak of the longer cleaved fragment at an elution time of 33 min. From the HPLC chromatograms, we conclude that endoproteinase GluC specifically cleaves its peptide substrate however, this cleavage is less efficient as compared to

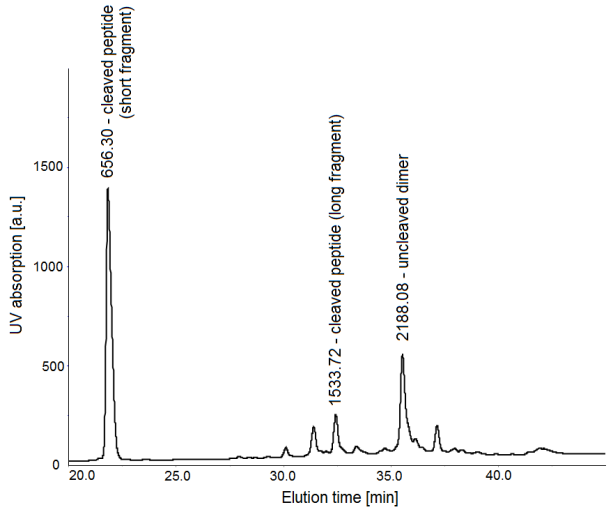

Figure 6.9: RP-HPLC chromatogram of the endoproteinase GluC peptide substrate, incubated with endoproteinase GluC for 3 hours at 37°C.

trypsin. When eventually translating this experiment to the SERS platform, we thus need to make sure that the incubation time is sufficiently long to enable endoproteinase GluC to cleave its peptide to a sufficiently large degree.

6.3.2 Checking for possible trypsin cleavage of the endoproteinase GluC peptide substrate

As a preparation for multiplexing experiments, we here check that there is no cleavage of the endoproteinase GluC substrate by trypsin. This is of paramount importance to ensure that the contributions of each protease in a multiplexing experiment can be correctly attributed.

We incubated trypsin with the endoproteinase GluC peptide substrate under the conditions described in Section 6.2.1. Here, the incubation lasted for 3 hours, as future multiplexing experiments need to consider the less efficient endoproteinase GluC. In Figure 6.10, the RP-HPLC chromatograms of the endoproteinase GluC substrate with or without trypsin incubation are overlaid. It is clear that trypsin does not cleave the endoproteinase GluC peptide substrate as it stays intact even after 3 hours of incubation. Before conducting multiplexing experiments, we would still have to check that

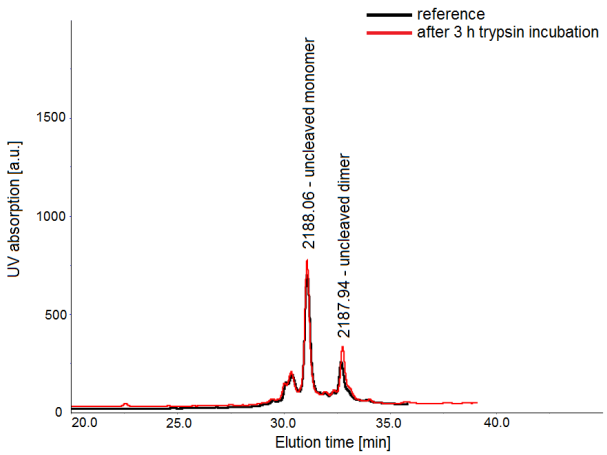

Figure 6.10: Comparison of the RP-HPLC chromatograms of the reference endoproteinase GluC peptide substrate (black) and the same peptide incubated with trypsin for 3 hours at 37°C.

endoproteinase GluC does not cleave the trypsin peptide substrate.

6.4 Nanophotonic slot waveguides for waveguide-based SERS detection of protease activity

We have shown that SERS can be used to detect active trypsin on gold nanodomes. Gold nanodomes are however free-space SERS substrates, which means that they require a bulky, complicated and expensive Raman microscope for read out. Novel techniques for the collection of Raman signals have recently emerged as alternatives to such a conventional Raman microscope, such as hollow-core photonic crystal fibers [50] and nanophotonic waveguides on photonic integrated circuits (PICs) [54, 64, 65, 153], as described in Chapter 5.

Nanophotonic waveguides were shown to efficiently excite and collect Raman signals of the molecules close to the waveguide, opening up the possibility to bring the selectivity of Raman measurements to an integrated lab-on-a-chip platform. Soon after, the first waveguide-based SERS platform was demonstrated, namely the integrated bowties [77]. The on-chip SERS platform shows great potential for high-throughput SERS assays on low sample volumes, especially relevant for the detection of biological molecules.

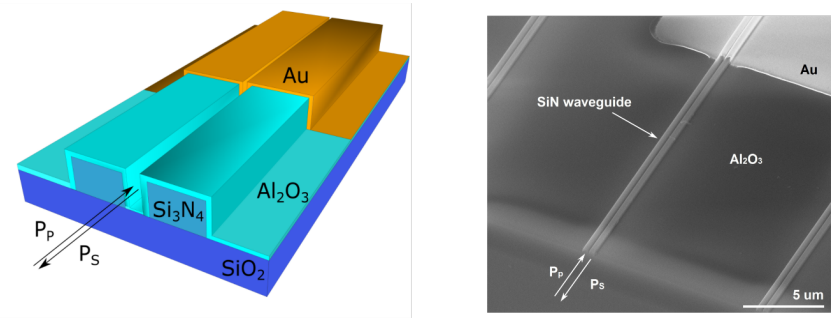

Figure 6.11: A schematic representation of the nanoplasmonic slot waveguide (left) and the corresponding SEM image (right).

Still, since most biological molecules have low Raman cross-sections, the SERS enhancements of the integrated bowties platforms is insufficient for their detection.

The high SERS enhancement of the nanoplasmonic slot waveguide shown in Figure 6.11 however shows promise for the SERS detection of biological molecules [79]. In addition to high SERS enhancement, the nanoplasmonic slot waveguides are fabricated using a combination of atomic layer deposition and deep UV photolithography, enabling mass scale manufacturing. Furthermore, they offer non-resonant enhancement, making the SERS enhancement independent of excited and scattered wavelengths [79].

In this section, we will discuss our efforts to demonstrate waveguide-based SERS detection of trypsin activity using the nanoplasmonic slot waveguide. First, we show how we have, for the first time, detected a SERS signal of a biomolecule, namely a peptide, on a waveguide-based SERS. Next, we had to check the stability of the SERS signal of the peptide labelled on the metal slot. To make sure that the SERS peak intensities change due to the trypsin activity, we had to establish that no chemical changes to the molecule coming from prolonged laser exposure and/or overheating took place and consequently altered the SERS spectra of the molecule. Finally, we performed trypsin cleavage experiments on the peptides labelled on the nanoplasmonic slot waveguides.

6.4.1 Detecting the peptide monolayer on the nanoplasmonic slot waveguide

Whereas the waveguide-based SERS platforms offer several advantages over conventional free-space SERS substrates, their SERS enhancements still lag behind the top performing free-space SERS substrates such as gold nandomes [149]. To detect a biomolecule – a peptide – for the first time on the on-chip SERS platform, we have turned to nanoplasmonic slot waveguides, which can currently offer the highest SERS enhancements with the lowest background [79]. To mitigate their lower SERS enhancement, we have at the same time modified our peptide substrate in order to increase its Raman cross-section and hence its intrinsic SERS signal. We have thus doubled both the aromatic amino acids in the peptide sequence to effectively double its SERS signal. This required some other small modifications in the peptide sequence, as described in Chapter 4. To establish that these changes did not affect trypsin cleavage of the peptide, we first demonstrated the SERS monitoring of trypsin cleavage on the free-space based gold nanodomes, as described in Section 6.2. We then used the peptide with the doubled aromatics and the sequence NH_2-CALNN(CN-F)GSG(CN-F)GGGGV**R**-GNFSF-COOH to label a nanoplasmonic slot waveguide with a gap size of 17 nm. The peptide labelling of the slot waveguide was done in exactly the same way as for the gold nanodomes described in Section 6.2.1. To acquire the SERS spectra of the nanoplasmonic slot waveguide on the confocal microscope, the sample was positioned vertically and end-fire coupled, as explained in more detail in Chapter 5. A Zeiss 63x/0.9 EC Epiplan NEOFLUAR:$\infty/0$ objective was used to couple the light into the waveguide with the laser power of 1 μW measured before the microscope objective and the integration time set to 5 s. The estimated laser power that was guided in the waveguide is approximately 300 μW, based on the coupling losses reported in [79].

A raw SERS spectrum is shown in Figure 6.12, which shows that the SERS background signal is quite high, but nevertheless the CN-F peak at 1180 cm^{-1} is clearly visible. The peak around 1600 cm^{-1} can be ascribed to the CALLN sequence in the peptide [49], and the peak at 2330 cm^{-1} belongs to the silicon nitride (Si_3N_4), and therefore indicates that the light is indeed guided in the Si_3N_4 waveguide [71].

The background subtracted SERS spectrum of the peptide is shown in Figure 6.13. There, one can clearly distinguish the SERS peaks of phenylalanine (F) and cyano-phenylalanine (CN-F). We have therefore shown the first time ever detection of a biomolecule, namely a peptide, on a waveguide-

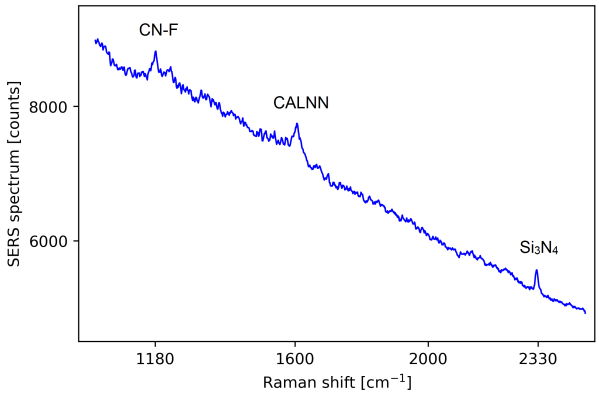

Figure 6.12: Raw SERS spectrum of the trypsin peptide substrate acquired on the nanoplasmonic slot waveguide. The silicon nitride peak at 2330 cm^{-1} indicates that the light is guided in the waveguide, whereas the other two peaks originate from the peptide itself.

based SERS platform. In the next section, we examine the stability of the SERS signal acquired on the nanoplasmonic slot waveguide.

6.4.2 Stability of the SERS spectrum of a peptide labelled on the nanoplasmonic slot waveguide

When acquiring SERS signals of different Raman reporters, the stability of the SERS spectra needs to be monitored. Upon prolonged exposure to high input laser power, Raman reporters may overheat and potentially burn or experience other chemical transitions that affect their molecular structure and therefore their Raman spectrum. One example is the photoinduced reduction of NTP to dimercaptoazobenzene, where these chemical changes affect the SERS signal strength of the 1339 cm^{-1} mode of the NTP [44].

In the case of the free-space excited nanodomes, we avoid this problem by acquiring spectra at several different locations on the nanodome sample. We typically record SERS spectra on 7x7 points at relatively low laser powers, as described in Section 6.2.1. However, when switching to waveguide-based nanoplasmonic slot waveguides, we are limited by the fact that we can excite and collect SERS spectra of one waveguide through only one access point, i.e. the silicon nitride access waveguide. We therefore have to pay special attention to use appropriate laser powers that will not chemically damage the peptides as this could lead to peak intensity changes

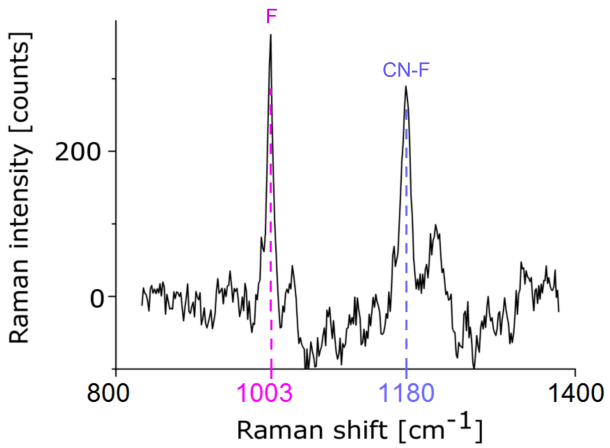

Figure 6.13: First time ever detection of the SERS signal of a peptide on a waveguide-based platform.

similar to those caused by trypsin cleavage of the peptide. In this section, we examine the effects of laser power and integration time on the stability of the peptides' SERS spectrum in the case of the nanoplasmonic slot waveguide.

To maximize the acquired SERS signal intensities, ideally one uses as high as possible laser powers with longer integration times. However, to avoid potential chemical changes to the peptide due to overheating, these parameters have to be correctly chosen. The peptides' exposure to the laser light will furthermore be affected by the physical parameters of the nanoplasmonic slot waveguide. The laser light can be coupled to the access waveguide with a varying efficiency, and the longer the access waveguide, the more laser light will be lost before it reaches the plasmonic structure [79]. The gap size of the metal slot will furthermore play an important role, since the smaller gaps will confine the incoming light much stronger [79].

Small variations in the above-mentioned parameters will greatly affect the laser light power that actually reaches the peptides. Due to the fabrication and measurement variations in the gap size, length of the access waveguide and the coupling efficiency, it is very hard to generically determine the laser excitation parameters. We have therefore decided to address this problem individually, by including a control experiment on our chips that will allow us to verify the stability of the peptide spectra for each individual chip. For this, we have designed our waveguides so that we always fabricate two identical neighboring waveguides (see Figure 6.14). These two waveguides have as much as possible the same length of the silicon access waveguide, the same

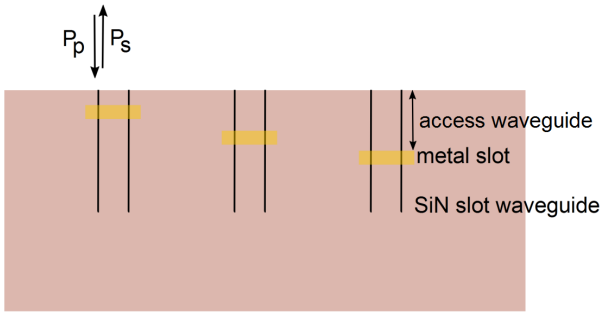

Figure 6.14: Schematic top view of a photonic chip with the integrated nanoplasmonic slot waveguides designed for SERS-based protease activity detection. The stability of the SERS signal is first checked on the reference waveguide.

gap size and the same coupling efficiencies for the input laser power. One of the two waveguides can therefore serve as a reference, where we acquire a time series of the SERS spectra. By analyzing the SERS peak intensities F/CN-F, we can establish if the SERS peak intensity ratio is stable in time when no trypsin cleavage is occurring. After the reference measurement is completed and the continuity of the SERS spectra is established, the sample can be then used in the trypsin experiment, as described in the next section.

We take the F/CN-F ratio as our relevant metric since the normalization on the CN-F peak makes it is robust against ligand exchange and desorption of the peptide from the gold surface, as mentioned in Chapter 4. In the case of the waveguide excitation and collection of the SERS spectra, the efficiency of the coupling of the laser light into the waveguide can change with time. The microscopic movements of the microscope stage can with time cause that the intensity of the SERS spectra and therefore its individual SERS peaks decrease due to less efficient light coupling. Using the F/CN-F ratio as our metric efficiently circumvents this coupling dependency as well.

The nanoplasmonic slot waveguides were labelled with the trypsin peptide substrate (NH_2-CALNN(CN-F)GSG(CN-F)GGGGV**R**-GNFSF-COOH) using the standard labelling procedure. SERS spectra were acquired using 0.3 mW laser power guided in the waveguide and an integration time of 30 s. To establish if there are any changes in the peak intensity ratio, we plot the F/CN-F peak intensity ratio as a function of time (Figure 6.15). The dashed vertical line indicates the average value of the F/CN-F peak intensity. We conclude that this particular waveguide set offers a good peptide stability in the desired time frame and thus allows us to perform a trypsin cleavage

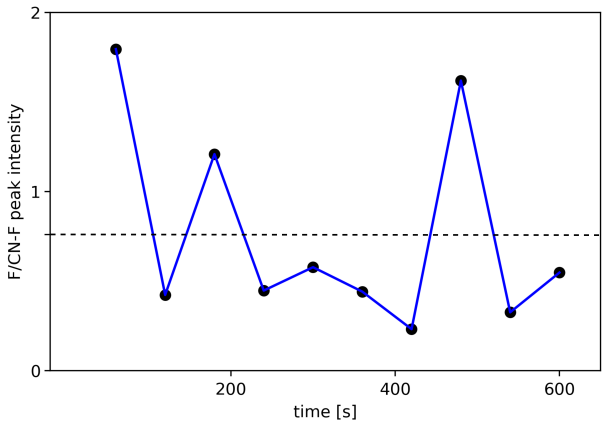

Figure 6.15: The F/CN-F peak intensity ratio is plotted as a function of time for assessing the stability of the SERS signal of the peptide under a continuous laser illumination. The dashed vertical line indicates the average value of the F/CN-F peak intensity. Due to the various geometrical parameters that can affect the amount of laser light that reaches the peptide, we have to establish the stability of the signal in each individual experiment.

experiment (see next section).

6.4.3 Detection of trypsin activity on the waveguide-based SERS platform

After establishing the stability of the SERS signal of the peptide described in the previous section, we proceeded with performing trypsin cleavage on the nanoplasmonic slot waveguide. We used the nanoplasmonic slot waveguide with a gap size of 43 nm (Figure 6.16). The sample was labelled with the peptide substrate for trypsin, where the doubled aromatic acids in the peptide substrate serve to effectively increase the Raman cross-section of the peptide, therefore ensuring a higher intrinsic SERS signal of the peptide. We acquired the SERS spectra of the peptide before and after trypsin addition using the waveguide-based excitation and collection of the SERS signal, as described in Chapter 5. These were collected on the neighboring nanoplasmonic slot waveguides with the same characteristics, as explained in the previous section. In this experiment, a laser power of 1 mW was used as measured before the microscope objective. The laser power guided in the waveguide and used to excite the SERS response was therefore around 0.3 mW, based on the coupling efficiency estimated in [79]. We recorded 10 measurements

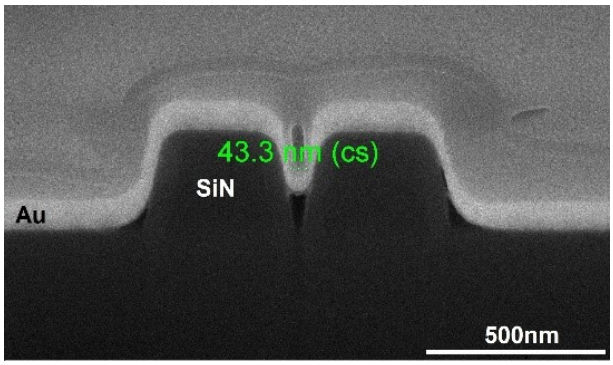

Figure 6.16: The cross-section of the nanoplasmonic slot waveguide used for the detection of trypsin activity on the waveguide-based SERS platform. A gap size of approximately 45 nm allows a good accessibility to the trypsin.

with an integration time of 60 s for each condition. The background was modelled using a polynomial fit and subtracted. In Figure 6.17 the averaged spectra of the background-subtracted measurements before and after trypsin addition are presented. The spectra are normalized on the CN-F peak at 1180 cm^{-1}. The F peak disappears completely, which corresponds with the 43 nm gap of the nanophotonic slot waveguide that should allow much better accessibility for trypsin compared to the small 12 nm gaps of the gold nanodomes.

To further quantify the trypsin activity, we calculated the integrated peak counts of the F and CN-F peaks at 1003 cm^{-1} and 1180 cm^{-1}, respectively. We notice a 70 % decrease in the F/CN-F peak intensity upon one hour of trypsin incubation (Figure 6.18), suggesting that trypsin has indeed cleaved the peptide substrate. Using our algorithm, we however did not notice full disappearance of the signal from the F peak. In this case, the remaining F/CN-F signal could be possibly attributed to another peak that appears at 1010 cm^{-1} after trypsin addition and is therefore an artefact of our data analysis. The appearance of such additional peak(s) after incubation with trypsin is not uncommon, as it can be caused either by trypsin sticking to the SERS substrate or other contaminants. The sample is always washed after incubation, but there might be some remaining contaminating molecules that cause the appearance of new SERS peaks. In our experiments, we never found additional contaminating peaks to be prominent compared to the SERS peaks of the investigated peptide, and these have thus never presented an issue when analyzing the SERS spectra.

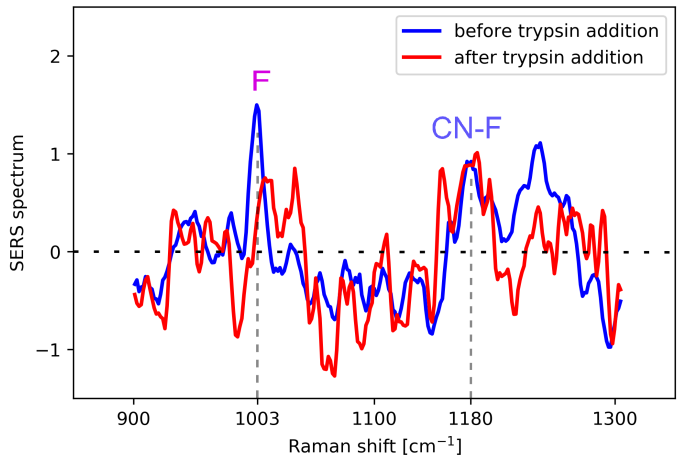

Figure 6.17: SERS spectra of the peptide before and after trypsin addition. The decrease in the F peak at 1003 cm^{-1} indicates trypsin-mediated cleavage of the peptide. Each spectrum shown in the graph is the average of 10 background-subtracted measurements. For better visualization, the spectra were smoothed with the simple moving average with the window size of 3.

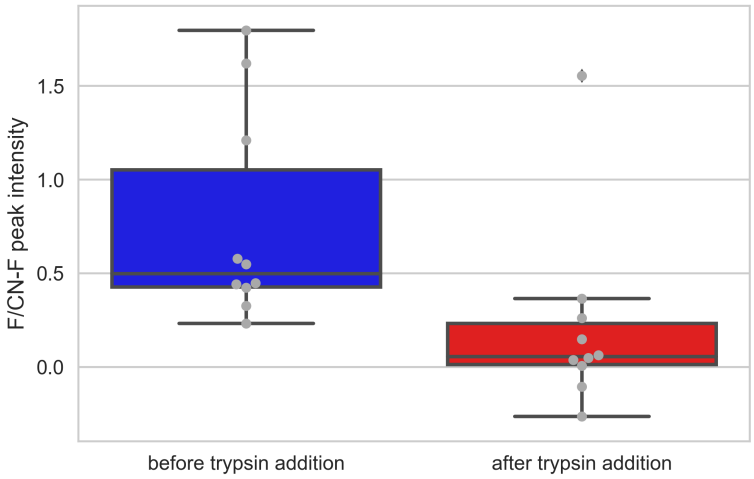

Figure 6.18: A box plot of F/CN-F peak intensities before and after trypsin addition. Individual measurements are presented as gray dots.

In conclusion, in this section we have examined the possibility of detecting protease activity on the waveguide-based SERS platform and have shown stable SERS signals of the peptides on the nanoplasmonic slot waveguide.

Finally, we have demonstrated for the first time the waveguide-based SERS detection of proteolytic activity via the cleavage of its peptide substrate that holds non-natural aromatic amino acids. We have demonstrated trypsin activity detection for a trypsin concentration of $2x10^{-7}$ M, however, it was previously shown that this technique can reach a detection limit of at least $8x10^{-9}$ M [49]. Whereas there already exist techniques that enable lower detection limits [169, 170], the use of the waveguide-based SERS substrate opens the possibility of multiplexed detection of protease activities on a small, mass-produced and reliable photonic chip.

7

Conclusions and Outlook

7.1 Conclusions

In this thesis, we have developed a waveguide-based SERS platform for protease activity sensing. To demonstrate waveguide-based detection of protease activity, we approached this challenge from both the biochemical and the photonics perspective. Both approaches proved complementary and their combination was crucial in achieving the final result.

Our main challenge from the photonics perspective was to establish a waveguide-based SERS platform which provides a high SERS enhancement. Early in this work, we examined the use of an organic adhesion layer of MPTMS as an alternative to the typically used titanium adhesion layer on integrated bowtie antennas. The latter was shown to dampen the plasmon resonances, thereby decreasing SERS enhancement. We demonstrated that the use of MPTMS results in at least 3-fold increase in the SERS signal compared to the samples with the titanium adhesion layer. However, we noticed a high variability in the SERS signal for the MPTMS sample, which probably stems from small variations in electron beam lithography processing that affect the antenna geometry and therefore its signal enhancement. Even with further optimization of the fabrication process, we were not able to

reduce the variability of the SERS signal. To achieve high and reproducible SERS enhancements, we therefore examined other waveguide-based SERS platforms, such as integrated nanotriangles [78] and the nanoplasmonic slot waveguide [79], comparing their SERS performance to the well-established free-space based gold nanodomes. We demonstrated that the nanoplasmonic slot waveguides are the best performing waveguide-based SERS substrate compared to the integrated bowtie antennas and the integrated nanotriangles, yet the free-space gold nanodomes still provide a 3-fold better signal-to-background ratio and a 15-fold better signal-to-noise ratio. We have therefore also explored the biochemical ways of increasing the SERS signal of the peptide substrate.

SERS-based protease activity sensing using natural aromatic amino acids was previously demonstrated in the free-space configuration using gold nanodomes [49]. Since these natural aromatics have relatively low Raman cross-sections, we explored the use of the non-natural aromatics. As there are only three natural aromatics, phenylalanine (F), tyrosine (Y) and tryptophan (W), the use of the non-natural aromatic amino acids provides a much more varied selection of Raman reporters with potentially higher Raman cross-sections. We examined several non-natural aromatics, including derivatives of tyrosine and phenylalanine, as well as phenylalanines containing stable heavy isotopes of hydrogen, carbon and nitrogen. The results, described in detail in Chapter 4, showed that nitro-tyrosine and phenylalanines with heavy isotopes provide strong Raman peaks in the 600-1400 cm^{-1} range. However, we noticed that the SERS peaks of some aromatics (partially) overlapped, so special care has to be taken to choose compatible aromatics as Raman reporters during multiplexing experiments.

We have successfully incorporated the non-natural aromatic cyano-phenylalanine (CN-F) in the peptide substrate for trypsin. We first tested the efficiency of trypsin cleavage of this peptide substrate using gold nanodomes in the free-space configuration. We demonstrated that trypsin efficiently cleaved the peptide and that the ratio of the F/CN-F peak intensities can be used as a metric to monitor peptide cleavage using SERS. We then used the integrated nanoplasmonic slot waveguides, labelled with the peptide with non-natural aromatic, to demonstrate waveguide-based detection of trypsin activity at a trypsin concentration of 0.2 μM.

As fabricating nanoplasmonic slot waveguide is more labor-intensive compared to gold nanodomes, we also explored possibilities to clean and reuse waveguide-based SERS chips. Typically, oxygen plasma is used to clean SERS substrates by removing the peptide monolayers. However,

oxygen plasma contaminates the gold surface with oxidized sulfur species, thereby increasing the SERS background signal and its variability. We found that hydrogen plasma cleaning leads to much more reproducible SERS spectra, thus providing a better alternative to oxygen plasma cleaning of SERS substrates.

7.2 Outlook

7.2.1 Improving the waveguide-based SERS platforms

Currently, the waveguide-based SERS platforms still do not match the performance of the free-space SERS substrates. However, several groups are researching new waveguide-based SERS platforms, and in the last years, a variety of new structures has been published with ever improving SERS enhancements. For a detailed review of the most recent developments, we refer the reader to Chapter 2, Section 2.5.3.

Nanoplasmonic slot waveguides for now still remain one of the best performing waveguide-based SERS platforms. However, lately some issues with the reproducibility of the gold deposition thickness occurred, which in turn lead to lower-performing devices that were used in the protease activity detection experiments. If these issues are solved, the nanoplasmonic slot waveguides can again provide SERS enhancements on par with the results reported in [79], thereby improving the signal-to-noise ratio in the protease sensing experiments.

Furthermore, oxygen and hydrogen plasma cleaning of the samples should be additionally examined to determine how many times the sample can be cleaned and reused before experiencing permanent damage.

7.2.2 Improving trypsin sensing using nanoplasmonic slot waveguides

In this work, we provided a proof-of-concept detection of trypsin activity using nanoplasmonic slot waveguides. In this demonstration, the detected trypsin concentration was 0.2 μM, but the actual detection limit still needs to be determined by performing further experiments. Previous free-space SERS experiments suggest that the detection limit of at least 8 nM can be achieved [49].

Furthermore, the time traces of trypsin-mediated peptide cleavage can be obtained with slight modification in the measurement setup. In principle, this can give some information on the kinetics of the cleavage reaction however, as the cleavage occurs on the peptide substrate bound to the gold surface, there might be significant differences compared to the kinetics of the unbound peptide substrates.

7.2.3 Multiplexed detection of protease activity

One of the most promising lines of investigation is to demonstrate the multiplexing capabilities of the SERS platform, both in free-space and waveguide-based configurations. SERS allows extended multiplexing [171], and we have already developed peptide substrates for endoproteinaseGluC, as described in Chapter 4, Section 4.3. The SERS based GluC activity detection however still needs to be demonstrated before performing multiplexed experiments with trypsin and GluC. In the multiplexing demonstration it is furthermore crucial that both peptide substrates can be identified with non-overlapping SERS peaks, so that the SERS signals pertaining to different proteases can be deconvoluted.

Once multiplexing with model proteases is established, more clinically relevant proteases can be evaluated, such as caspases [172]. There, the reductive environment needed for the cysteine protease activity currently presents an additional challenge, which can be addressed with special modifications to the peptide monolayer, as discussed in [7].

7.2.4 SERS sensing of tyrosine phosphorylation

The established methodology could be used to monitor tyrosine phosphorylation, either in free space or on a waveguide-based SERS platform. Tyrosine phosphorylation occurs when a phosphate group ($PO_4{}^{3-}$) is added to the amino acid tyrosine. It is an important mechanism of signal transduction and regulation in eukaryotic cells, influencing among other cell cycle progression, metabolic homeostasis, neural transmission, and aging [173]. Perturbations in the process are a root cause of many human diseases, in particular cancer, making the inhibitors of tyrosine kinases interesting drug targets [173].

In this thesis, we have shown the SERS spectra of tyrosine and phosphotyrosine in Chapter 4, Figure 4.5. Both spectra show characteristic SERS peaks, which are however not very prominent. In order to monitor phos-

phorylation of tyrosine, we would therefore need to enhance the SERS sensitivity of the current platforms, or alternatively use more advanced SERS data analysis techniques.

7.2.5 Fully integrated sensing of protease activity

Photonic integrated circuits enable the miniaturization of the bulky laboratory systems currently needed for the detection of the protease activity. Free-space SERS substrates require the use of a confocal Raman microscope however, in the waveguide-based approach the functionalities of the microscope can be implemented on a small photonic chip, as discussed in Chapter 2, Section 2.5.1.

In the long-term scope of this work, the integration of the waveguide-based SERS sensor with the other functionalities of the Raman microscope can be implemented. The on-chip laser source, filters and the spectrometer have already been developed, and integrating the necessary components will allow to establish a lab-on-a-chip platform for sensing of protease activity.

A

Peptide synthesis

A.1 Peptides

Peptides are biomolecules consisting of amino acids linked together via the so-called peptide bond. By definition, they are limited in size to about 50 amino acids. Longer peptides are named polypeptides or proteins.

To chemically synthesize a peptide, a so-called condensation reaction must occur between two amino acids. In this way, a peptide bond is formed between the carboxyl group of one amino acid and the amino group of another, and water is released as a byproduct, as shown in Figure A.1. The NH_2-end of a peptide is named the N- or amino-terminus, and the COOH-containing end is called the C- or carboxy-terminus. In this thesis and by convention, peptide sequence are always written from the N- to the C-terminus, whereas chemically, peptides are synthesized the other way around.

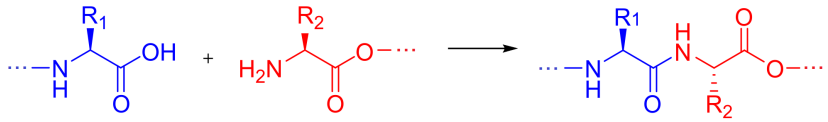

Figure A.1: Formation of the peptide bond. Adapted from [82]

A.2 Amino acids

All the amino acids contain amine (-NH_2) and carboxyl (-COOH) functional groups, but differ in their side chain (R group). Naturally occurring proteins all consist of different sequences of just 20 amino acids, presented in Figure A.2. For Raman applications, the aromatic amino acids containing a benzene ring, namely phenylalanine, tyrosine and tryptophan, are especially important as they provide the highest Raman cross-sections of all the 20 amino acids [141].

Conversely, there are numerous amino acids that are not present in natural proteins but can be incorporated by chemical synthesis, expanding their possible uses. One example are non-natural aromatics, which were used in this thesis to expand the multiplexing capabilities of the SERS based detection of the protease activity (Chapter 4).

A.3 Solid-phase peptide synthesis

The most widely used peptide synthesis method in is solid-phase peptide synthesis [175], presented schematically in Figure A.3. Here, small polymeric resin beads are used as anchors for the peptide chain to be synthesized. These beads are functionalized with reactive groups, to which the starting amino acid (thus, C-terminal amino acid) is already attached or can be chemically attached. Each amino acid to be coupled to the growing peptide chains' N-terminus must be protected on its N-terminal amino group and, if needed, on its side chain to prevent unwanted chemical reactions [176]. In this thesis, commercially available Fmoc protected amino acids were used for peptide synthesis. In each step of peptide synthesis, the N-terminal group of the peptide chain has to be deprotected, and then the next amino acid is added to the chain. The growing peptide is covalently attached to the support throughout synthesis, meaning that side products of the reaction and excess reagents can be efficiently washed away. At the end of the synthesis, the

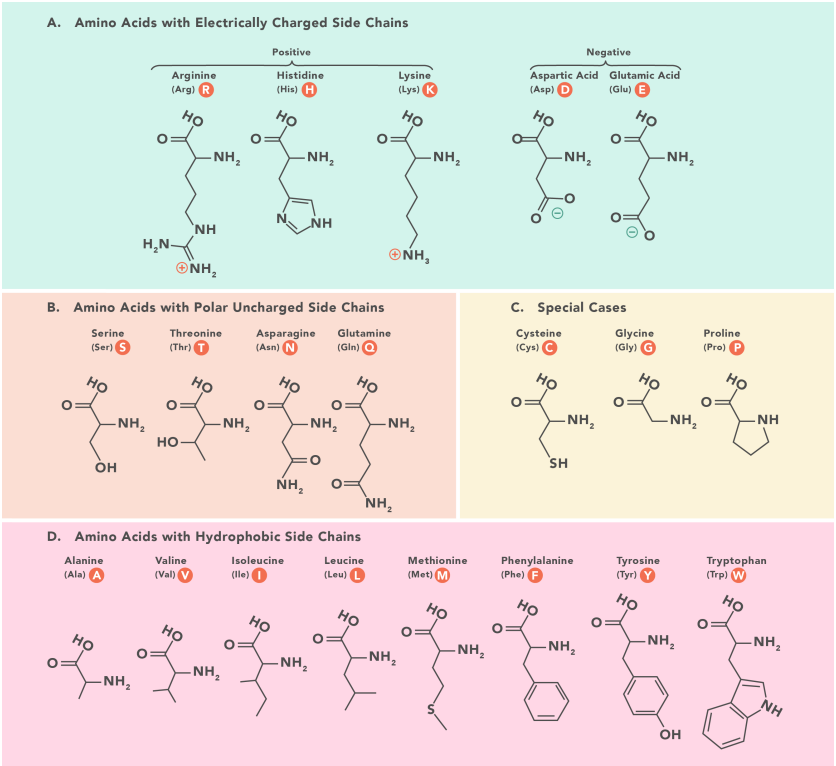

Figure A.2: Overview of the amino acids found in natural proteins. [174]

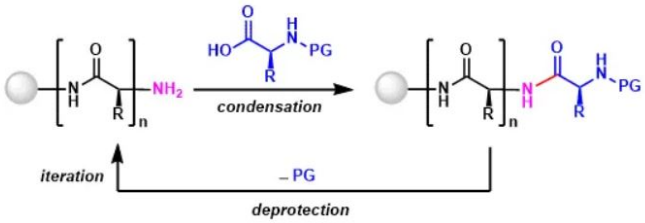

Figure A.3: Principle of solid-phase peptide synthesis. [178]

peptide chain is hydrolyzed from the resin while at the same time removing all protecting groups. This peptide is then dissolved in a non-polar solvent and precipitated to remove remaining byproducts. Next, it is purified using reversed-phase HPLC [177] (see Appendix B).

Solid-phase peptide synthesis has a limited reaction yield in each step, which depends on the amino acids used and the actual peptide sequence. The final yield is calculated as the multiplication of the yields in each step, and can get significantly low for longer peptides. However, peptides with lengths of up to 70 amino acids can be still synthesized relatively efficiently [175].

B

RP-HPLC

High-Performance Liquid Chromatography (HPLC) is an analytical chromatographic technique used to separate different components in a mixture. It uses columns filled with a solid adsorbent material, i.e. a stationary phase. A sample mixture is injected on the column and, then, a liquid solvent (mobile phase or eluent) is used to push the mixture through the column. Different components in the sample mixture interact slightly differently with the stationary phase, which leads to separation of components in this mixture. As the components leave the column, they can be collected for further analysis. The principle of column chromatography is shown in Figure B.1 for the gravity-based separation. In HPLC, the pressure is used instead of gravity to push the mixture through the column.

In this thesis, Reverse Phase HPLC (RP-HPLC) was used to purify peptides after their synthesis, and to evaluate if the proteases specifically cleaved their peptide substrates. In RP-HPLC, a hydrophobic stationary phase is used, which has a higher affinity for more hydrophobic compounds. A gradient of the mobile phase is created from polar to apolar, causing hydrophilic molecules to first elute from and pass through the column. Once hydrophilic molecules are eluted, the hydrophobic ones are still adsorbed to the stationary phase. Here, the solvent gradient comes into the picture, such that hydrophobic molecules also get eluted. This way all components in a

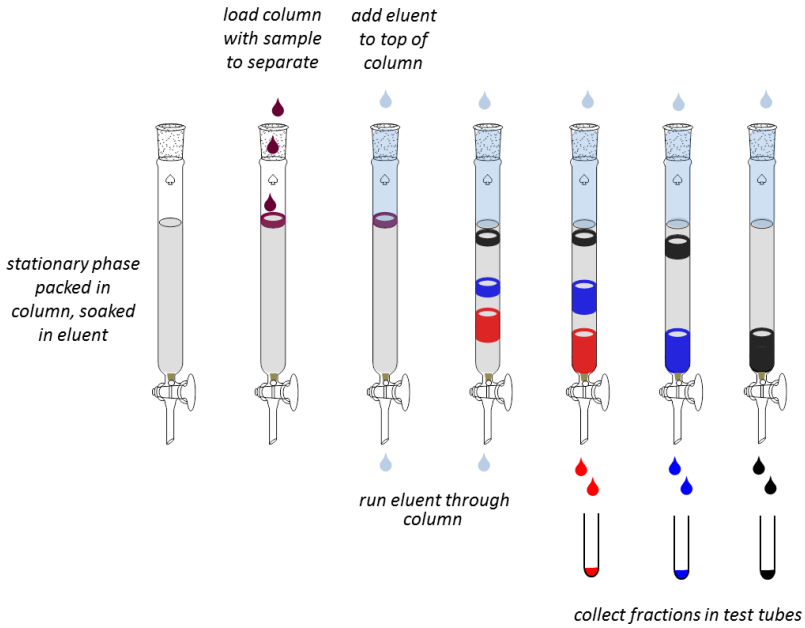

Figure B.1: The principle of column chromatography based on gravity separation. Conversely, in HPLC the pressure ensures that the mixture passes through the column. [[179]

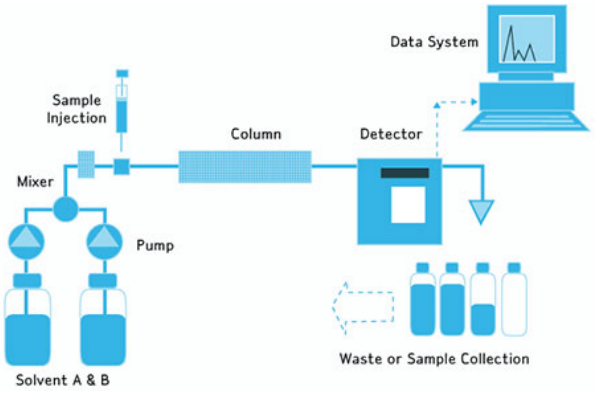

Figure B.2: Schematic of an RP-HPLC instrument. After the sample injection in the column, the sample is pushed through the column using high pressure. The hydrophilic molecules have a lower affinity for the stationary phase in the column, so they elute first. The solvent gradient of solvents A and B is then used to flush out the more hydrophobic molecules. As the HPLC fractions leave the column, they are detected via UV absorption spectroscopy and collected in separate HPLC fractions. [180]

mixture are separated and collected in different fractions. A schematic of a HPLC instrument is shown in Figure B.2.

UV absorption is typically used to detect eluting molecules. For example, in the case of peptides, absorption of UV-light (e.g. of 214 nm) by peptide bond is monitored. Figure B.3 shows a typical HPLC chromatogram. Each peak here represents a peptide with a specific peptide sequence, and the more hydrophilic peptides elute sooner. UV analysis can give rough estimation on the quantity of each component present in a mixture, with higher peak intensities indicating higher amount of this component. However, to precisely identify the peptides that are found in each collected fraction, further examination is needed, for instance by mass spectrometry, described in Appendix C.

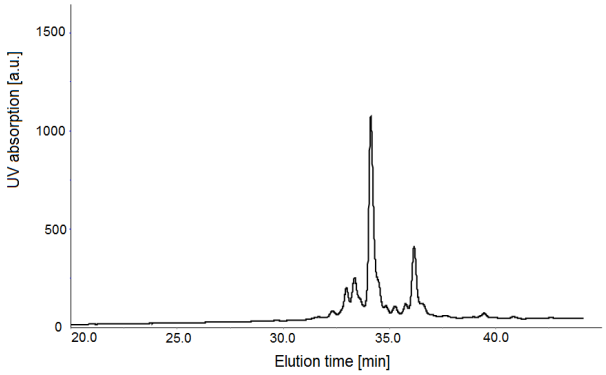

Figure B.3: An example of a RP-HPLC chromatogram of a peptide mixture. Different peaks represent different peptides in the sample mixture.

C

MALDI-TOF mass spectrometry

Mass spectrometry is an analytical technique that measures the mass-to-charge ratio of ions. The results are represented in a so-called mass spectrum, where the intensity of an ion is plotted with its mass-to-charge ratio. In a mass spectrometer, a sample is first ionized, which causes that the sample's molecules become charged. These ions are then accelerated through or transferred to an electric or magnetic field, where they are separated according to their mass-to-charge ratio. The ions are detected by a microchannel plate detector. The components in the sample can be identified by correlating known/predicted masses to identified masses or using a characteristic fragmentation pattern (so-called tandem mass spectrometry).

The ion source is the part of the mass spectrometer in which analytes are ionized. The ions are then transported by magnetic or electric fields to the mass analyzer. There are several different ionization techniques, of which matrix-assisted laser desorption/ionization (MALDI) is especially suited for the analysis of peptides because of its ability to create ions from large molecules with minimal fragmentation [181]. In MALDI, the sample is first mixed with matrix material and deposited on the metal plate. Next, the pulsed laser irradiates the sample, which causes the ablation and desorption of both the sample and the matrix material. In the end, the ablated analyte molecules are ionized by protonation or deprotonation, as summa-

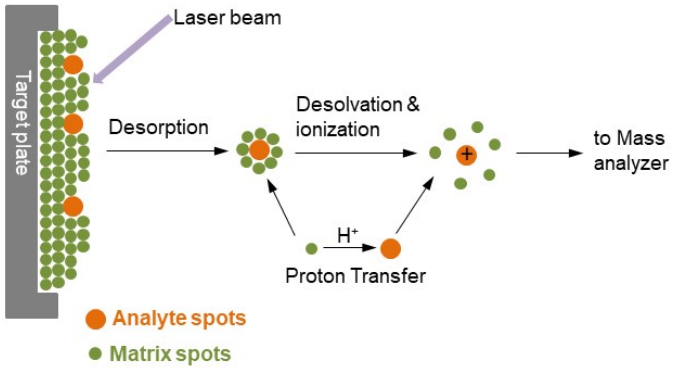

Figure C.1: Principle of matrix-assisted laser desorption/ionization (MALDI). [183]

rized schematically in Figure C.1. The ionized analyte molecules are then accelerated into the (in our case TOF) mass spectrometer [182].

In a time-of-flight (TOF) separator, ions are accelerated in an electric field through the same electrical potential, as shown in Figure C.2. The time needed to reach a detector is measured and the mass-to-charge ratio calculated. If ions have the same charge, their velocities in this electric field only depend on their masses.

To calculate the mass-to-charge ratio from the time-of-flight, one assumes that all the potential energy of an ion in an electric field is converted to its kinetic energy.

$$E_p = E_k \tag{C.1}$$

$$E_p = zU \tag{C.2}$$

where z is the charge of the ion and U the voltage.

$$E_k = \frac{1}{2}mv^2 \tag{C.3}$$

where m is the mass of the ion, and v the velocity. From this, one can calculate the time-of-flight as:

$$t = k\sqrt{\frac{m}{z}} \tag{C.4}$$

Based on the time-of-flight (TOF) calculations, a mass spectrum is plotted showing the ion signal strength (intensity) versus the mass-to-charge

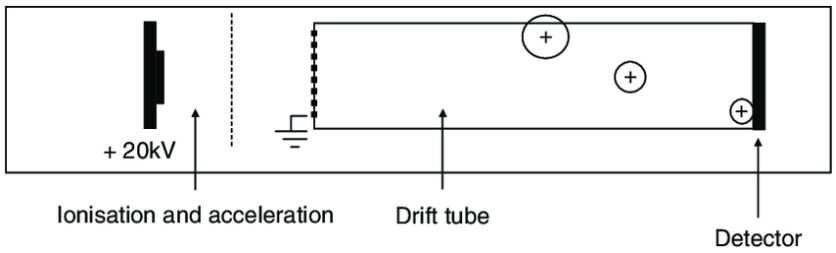

Figure C.2: Schematic of a time-of-flight (TOF) analyzer. [184]

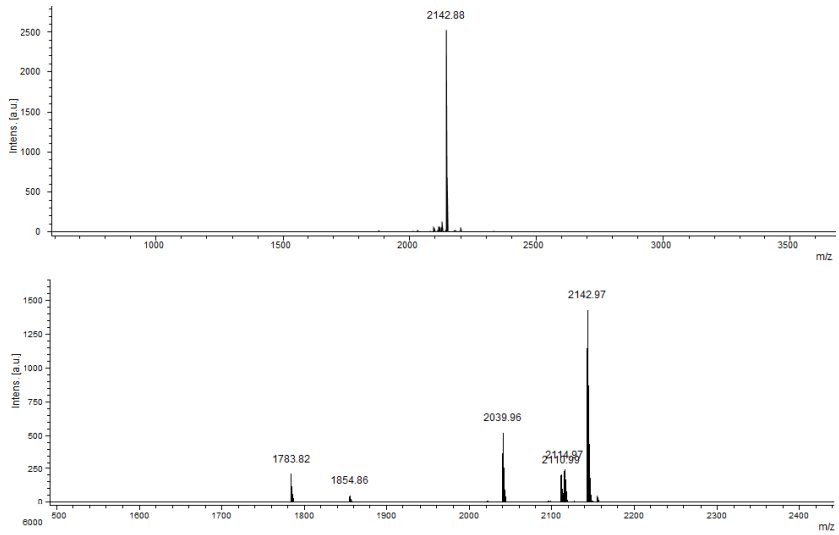

Figure C.3: Typical mass spectra where the intensity of the ion signal is plotted as a function of mass-to-charge ratio (m/z). In the upper spectrum, only one peak is clearly visible, whereas in the lower spectrum, several peaks are clearly apparent.

(m/z) ratio. From the peptide sequence, the mass of the peptide can be calculated and linked to the masses observed in the spectra.

D

SERS peak assignment of F and CN-F

We can attribute the SERS peak at 1003 cm^{-1} to the trigonal ring breathing of the benzene ring of L-phenylalanine [185].

We assigned the SERS peak at 1180 cm-1 to the non-natural aromatic amino acid cyano-phenylalanine experimentally. Therefore, we have measured the Raman spectra of the powders of phenylalanine, where we observed the peak at 1003 cm^{-1} as expected, and cyano-phenylalanine, where we observed a peak at 1180 cm^{-1}. The Raman spectra of cyano-phenylalanine measured were however of the Fmoc-protected amino acid, so the aromatic rings of Fmoc group provided some additional Raman peaks [186]. Due to the costly materials, we decided not to remove the Fmoc group. However to assess the peaks belonging to the Fmoc group, we recorded the Raman spectrum of Fmoc-alanine as alanine gives negligible Raman response compared to the aromatic rings of the Fmoc moiety [141]. All the prominent SERS peaks of the Fmoc-Alanine molecule can therefore be ascribed to Fmoc moiety. The recorded Raman spectra are shown in Figure D.1, where we can see that all the Raman peaks can be attributed to the Fmoc molecule, with the exception of the peak at 1180 cm^{-1}, that is therefore ascribed to the CN-F.

We additionally collected spectra of the peptide NH_2-CFG-COOH,

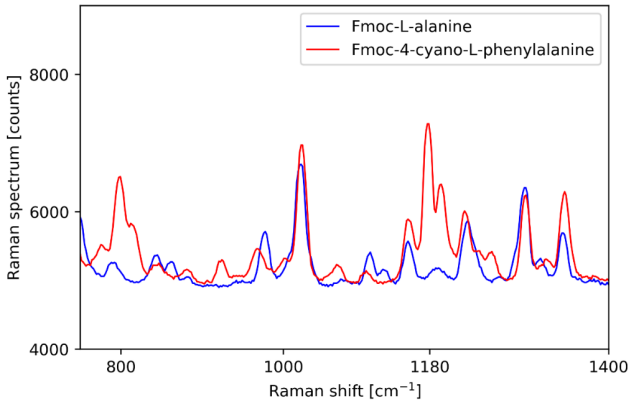

Figure D.1: The Raman spectra of the powders of Fmoc-L-alanine and Fmoc-4-cyano-L-phenylalanine.

where we observed the 1003 cm^{-1} peak pertaining to the phenylalanine, and spectra of the NH_2-CALNN(CN-F)S(CN-F)GGVR-COOH peptide, where the only aromatic acid is the cyano-phenylalanine (Figure D.2). The peptide NH_2-CF-COOH shows the expected peak at 1003 cm^{-1} and the smaller peak at 1030 cm^{-1}, which can both be ascribed to phenylalanine [185]. The spectra of the NH_2-CALNN(CN-F)FS(CN-F)GGGGVR-COOH showed only one peak at 1180 cm^{-1}.

Based on these two experiments, we therefore concluded that the 1180 cm^{-1} peak belongs to CN-F. In the literature, cyano-phenylalanine was used as a Raman probe to detect the polarity of the environment [139] but these authors used the C≡N vibration mode that yields a SERS peak at 2237 cm^{-1}. We therefore assume that the 1180 cm^{-1} peak comes from one of the vibration modes of the benzene ring, but are unable to pinpoint this further.

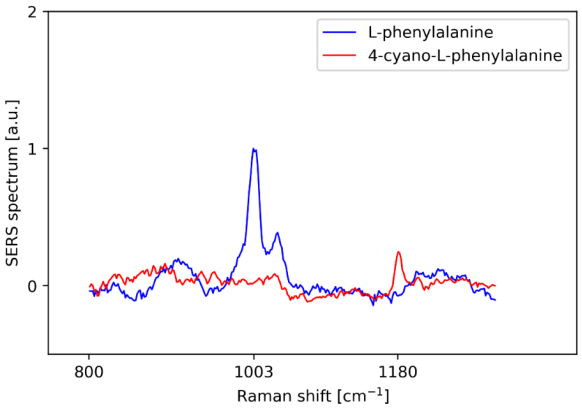

Figure D.2: The SERS spectra of the peptide chains containing the aromatic amino acids phenylalanine and cyano-phenylalanine. The peak intensities are arbitrary and cannot be directly compared.

References

[1] A. Z. Subramanian, E. Ryckeboer, A. Dhakal, F. Peyskens, A. Malik, B. Kuyken, H. Zhao, S. Pathak, A. Ruocco, A. D. Groote, P. Wuytens, D. Martens, F. Leo, W. Xie, U. D. Dave, M. Muneeb, P. V. Dorpe, J. V. Campenhout, W. Bogaerts, P. Bienstman, N. L. Thomas, D. V. Thourhout, Z. Hens, G. Roelkens, and R. Baets, "Silicon and silicon nitride photonic circuits for spectroscopic sensing on-a-chip," *Photon. Res.*, vol. 3, pp. B47–B59, Oct 2015.

[2] M. Drag and G. S. Salvesen, "Emerging principles in protease-based drug discovery," *Nature Reviews Drug Discovery*, vol. 9, no. 9, 2010.

[3] K. Anand, J. Ziebuhr, P. Wadhwani, J. R. Mesters, and R. Hilgenfeld, "Coronavirus main proteinase (3clpro) structure: Basis for design of anti-sars drugs," *Science*, vol. 300, no. 5626, pp. 1763–1767, 2003.

[4] L. Zhang, D. Lin, X. Sun, U. Curth, C. Drosten, L. Sauerhering, S. Becker, K. Rox, and R. Hilgenfeld, "Crystal structure of sars-cov-2 main protease provides a basis for design of improved α-ketoamide inhibitors," *Science*, vol. 368, no. 6489, pp. 409–412, 2020.

[5] I. L. H. Ong and K.-L. Yang, "Recent developments in protease activity assays and sensors," *Analyst*, vol. 142, pp. 1867–1881, 2017.

[6] Y. S. Yamamoto, Y. Ozaki, and T. Itoh, "Recent progress and frontiers in the electromagnetic mechanism of surface-enhanced raman scattering," *Journal of Photochemistry and Photobiology C: Photochemistry Reviews*, vol. 21, pp. 81 – 104, 2014. Special issue on Surface-Enhanced Raman Scattering (SERS).

[7] P. Wuytens, *Surface-Enhanced Raman Spectroscopy for Intracellular Sensing and Protease Activity Detection: From Chip Technology to Applications*. PhD thesis, Ghent University, 10 2017.

[8] H. Hamaguchi, C. Kato, and M. Tasumi, "Observation of transient resonance raman spectra of the s1 state of trans-stilbene," *Chemical Physics Letters*, vol. 100, no. 1, pp. 3 – 7, 1983.

[9] J. R. Lakowicz, *Principles of Fluorescence Spectroscopy*. Springer, 2006.

[10] D. A. Long, *The Raman Effect: A Unified Treatment of the Theory of Raman Scattering by Molecules*. Wiley, 2002.

[11] "Absorption spectrum of water." https://en.wikipedia.org/wiki/File:Absorption_spectrum_of_liquid_water.png. Accessed: May 5, 2020.

[12] E. Le Ru and P. Etchegoin, *Principles of Surface-Enhanced Raman Spectroscopy*. Elsevier Science, 2008.

[13] S. A. Meyer, E. C. L. Ru, and P. G. Etchegoin, "Quantifying resonant raman cross sections with sers," *The Journal of Physical Chemistry A*, vol. 114, no. 17, pp. 5515–5519, 2010.

[14] J. R. Ferraro, K. Nakamoto, and C. W. Brown, *Introductory Raman Spectroscopy*. Academic Press, 2003.

[15] R. Loudon, *The Quantum Theory of Light*. Oxford University Press, 2000.

[16] L. Novotny and B. Hecht, *Principles of Nano-Optics*. Cambridge University Press, 2006.

[17] J. D. Jackson, *Classical Electrodynamics*. Wiley, 1998.

[18] "Morse potential." https://en.wikipedia.org/wiki/Morse_potential. Accessed: May 5, 2020.

[19] "Raman and infrared spectra of carbon dioxide." https://www.americanpharmaceuticalreview.com/Featured-Articles/37183-Understanding-Infrared-and-Raman-Spectra-of-Pharmaceutical-Polymorphs/. Accessed: August 6, 2020.

[20] S. A. Maier, *Plasmonics: Fundamentals and Applications*. Springer, 2007.

[21] A. Raza, *Raman spectroscopy enhanced by on-chip dielectric and metal waveguides*. PhD thesis, Ghent University, 12 2019.

[22] J. M. Pitarke, V. M. Silkin, E. V. Chulkov, and P. M. Echenique, "Theory of surface plasmons and surface-plasmon polaritons," *Reports on Progress in Physics*, vol. 70, pp. 1–87, dec 2006.

[23] R. Dragila, B. Luther-Davies, and S. Vukovic, "High transparency of classically opaque metallic films," *Phys. Rev. Lett.*, vol. 55, pp. 1117–1120, Sep 1985.

[24] I. Pockrand, "Coupling of surface plasma oscillations in thin periodically corrugated silver films," *Optics Communications*, vol. 13, no. 3, pp. 311 – 313, 1975.

[25] J. Homola, S. S. Yee, and G. Gauglitz, "Surface plasmon resonance sensors: review," *Sensors and Actuators B: Chemical*, vol. 54, no. 1, pp. 3 – 15, 1999.

[26] K. A. Willets and R. P. Van Duyne, "Localized surface plasmon resonance spectroscopy and sensing," *Annual Review of Physical Chemistry*, vol. 58, no. 1, pp. 267–297, 2007. PMID: 17067281.

[27] K. M. Mayer and J. H. Hafner, "Localized surface plasmon resonance sensors," *Chemical reviews*, vol. 111, p. 3828—3857, June 2011.

[28] C. Boozer, G. Kim, S. Cong, H. Guan, and T. Londergan, "Looking towards label-free biomolecular interaction analysis in a high-throughput format: a review of new surface plasmon resonance technologies," *Current opinion in biotechnology*, vol. 17, p. 400—405, August 2006.

[29] G. Sun, J. B. Khurgin, and A. Bratkovsky, "Coupled-mode theory of field enhancement in complex metal nanostructures," *Phys. Rev. B*, vol. 84, p. 045415, Jul 2011.

[30] E. W. Weisstein, "Legendre polynomial." https://mathworld.wolfram.com/LegendrePolynomial.html. Accessed: May 5, 2020.

[31] S. Lal, S. Link, and N. Halas, "Nano-optics from sensing to waveguiding," *Nature Photon*, vol. 1, pp. 641–648, 2007.

[32] A. Melikyan, L. Alloatti, and A. Muslija, "High-speed plasmonic phase modulators," *Nature Photon*, vol. 8, pp. 229–233, 2014.

[33] Y. Xu, P. Bai, X. Zhou, Y. Akimov, C. E. Png, L.-K. Ang, W. Knoll, and L. Wu, "Optical refractive index sensors with plasmonic and

photonic structures: Promising and inconvenient truth," *Advanced Optical Materials*, vol. 7, no. 9, p. 1801433, 2019.

[34] J. N. Anker, W. P. Hall, O. Lyandres, N. C. Shah, J. Zhao, and R. P. Van Duyne, "Biosensing with plasmonic nanosensors," *Nature Materials*, vol. 7, pp. 442–453, 2008.

[35] P. West, S. Ishii, G. Naik, N. Emani, V. Shalaev, and A. Boltasseva, "Searching for better plasmonic materials," *Laser & Photonics Reviews*, vol. 4, no. 6, pp. 795–808, 2010.

[36] M. Moskovits, "Surface-enhanced raman spectroscopy: a brief retrospective," *Journal of Raman Spectroscopy*, vol. 36, no. 6-7, pp. 485–496, 2005.

[37] S. R., I. C., and L. C.M., "Sers-active silver colloids prepared by reduction of silver nitrate with short-chain polyethylene glycol," *Nanoscale Res Lett*, vol. 8, 2013.

[38] J. Neddersen, G. Chumanov, and T. M. Cotton, "Laser ablation of metals: A new method for preparing sers active colloids," *Applied Spectroscopy*, vol. 47, no. 12, pp. 1959–1964, 1993.

[39] O. Péron, E. Rinnert, M. Lehaitre, P. Crassous, and C. Compère, "Detection of polycyclic aromatic hydrocarbon (pah) compounds in artificial sea-water using surface-enhanced raman scattering (sers)," *Talanta*, vol. 79, no. 2, pp. 199 – 204, 2009.

[40] P. Mosier-Boss, "Review of sers substrates for chemical sensing," *Nanomaterials*, vol. 7, 2017.

[41] J. C. Hulteen and R. P. Van Duyne, "Nanosphere lithography: A materials general fabrication process for periodic particle array surfaces," *Journal of Vacuum Science & Technology A*, vol. 13, no. 3, pp. 1553–1558, 1995.

[42] D. A. Stuart, C. R. Yonzon, X. Zhang, O. Lyandres, N. C. Shah, M. R. Glucksberg, J. T. Walsh, and R. P. Van Duyne, "Glucose sensing using near-infrared surface-enhanced raman spectroscopy: Gold surfaces, 10-day stability, and improved accuracy," *Analytical Chemistry*, vol. 77, no. 13, pp. 4013–4019, 2005. PMID: 15987105.

[43] C. Farcau and S. Astilean, "Mapping the sers efficiency and hot-spots localization on gold film over nanospheres substrates," *The Journal of Physical Chemistry C*, vol. 114, no. 27, pp. 11717–11722, 2010.

[44] M. Tabatabaei, A. Sangar, N. Kazemi-Zanjani, P. Torchio, A. Merlen, and F. Lagugné-Labarthet, "Optical properties of silver and gold tetrahedral nanopyramid arrays prepared by nanosphere lithography," *The Journal of Physical Chemistry C*, vol. 117, no. 28, pp. 14778–14786, 2013.

[45] J. Li, C. Chen, H. Jans, X. Xu, N. Verellen, I. Vos, Y. Okumura, V. V. Moshchalkov, L. Lagae, and P. Van Dorpe, "300 mm wafer-level, ultra-dense arrays of au-capped nanopillars with sub-10 nm gaps as reliable sers substrates," *Nanoscale*, vol. 6, pp. 12391–12396, 2014.

[46] U. Huebner, K. Weber, D. Cialla, R. Haehle, H. Schneidewind, M. Zeisberger, R. Mattheis, H.-G. Meyer, and J. Popp, "Microfabricated polymer-substrates for sers," *Microelectronic Engineering*, vol. 98, pp. 444 – 447, 2012. Special issue MNE 2011 - Part II.

[47] F. Peyskens, A. Z. Subramanian, P. Neutens, A. Dhakal, P. V. Dorpe, N. L. Thomas, and R. Baets, "Bright and dark plasmon resonances of nanoplasmonic antennas evanescently coupled with a silicon nitride waveguide," *Opt. Express*, vol. 23, pp. 3088–3101, Feb 2015.

[48] P. C. Wuytens, A. Z. Subramanian, W. H. De Vos, A. G. Skirtach, and R. Baets, "Gold nanodome-patterned microchips for intracellular surface-enhanced raman spectroscopy," *Analyst*, vol. 140, pp. 8080–8087, 2015.

[49] P. C. Wuytens, H. Demol, N. Turk, K. Gevaert, A. G. Skirtach, M. Lamkanfi, and R. Baets, "Gold nanodome sers platform for label-free detection of protease activity," *Faraday Discuss.*, vol. 205, pp. 345–361, 2017.

[50] F. Benabid, J. C. Knight, G. Antonopoulos, and P. S. J. Russell, "Stimulated raman scattering in hydrogen-filled hollow-core photonic crystal fiber," *Science*, vol. 298, no. 5592, pp. 399–402, 2002.

[51] A. Dhakal, P. Wuytens, F. Peyskens, A. Subramanian, A. Skirtach, N. Le Thomas, and R. Baets, "Nanophotonic lab-on-a-chip raman sensors: A sensitivity comparison with confocal raman microscope," in *2015 International Conference on BioPhotonics (BioPhotonics)*, pp. 1–4, May 2015.

[52] E. P. Haglund, S. Kumari, P. Westbergh, J. S. Gustavsson, G. Roelkens, R. Baets, and A. Larsson, "Silicon-integrated short-wavelength hybrid-cavity vcsel," *Opt. Express*, vol. 23, pp. 33634–33640, Dec 2015.

[53] X. Nie, N. Turk, Y. Li, Z. Liu, and R. Baets, "High extinction ratio on-chip pump-rejection filter based on cascaded grating-assisted contra-directional couplers in silicon nitride rib waveguides," *Opt. Lett.*, vol. 44, pp. 2310–2313, May 2019.

[54] A. Dhakal, A. Z. Subramanian, P. Wuytens, F. Peyskens, N. L. Thomas, and R. Baets, "Evanescent excitation and collection of spontaneous raman spectra using silicon nitride nanophotonic waveguides," *Opt. Lett.*, vol. 39, pp. 4025–4028, Jul 2014.

[55] X. Nie, E. Ryckeboer, G. Roelkens, and R. Baets, "Cmos-compatible broadband co-propagative stationary fourier transform spectrometer integrated on a silicon nitride photonics platform," *Opt. Express*, vol. 25, pp. A409–A418, Apr 2017.

[56] E. Ryckeboer, R. Bockstaele, M. Vanslembrouck, and R. Baets, "Glucose sensing by waveguide-based absorption spectroscopy on a silicon chip," *Biomed. Opt. Express*, vol. 5, pp. 1636–1648, May 2014.

[57] K. D. Vos, I. Bartolozzi, E. Schacht, P. Bienstman, and R. Baets, "Silicon-on-insulator microring resonator for sensitive and label-free biosensing," *Opt. Express*, vol. 15, pp. 7610–7615, Jun 2007.

[58] Y. Levy, C. Imbert, J. Cipriani, S. Racine, and R. Dupeyrat, "Raman scattering of thin films as a waveguide," *Optics Communications*, vol. 11, no. 1, pp. 66 – 69, 1974.

[59] J. F. Rabolt, R. Santo, and J. D. Swalen, "Raman spectroscopy of thin polymer films using integrated optical techniques," *Appl. Spectrosc.*, vol. 33, pp. 549–551, Nov 1979.

[60] J. F. Rabolt, R. Santo, and J. D. Swalen, "Raman measurements on thin polymer films and organic monolayers," *Applied Spectroscopy*, vol. 34, no. 5, pp. 517–521, 1980.

[61] J. Rabe, J. Swalen, and J. Rabolt, "Order–disorder transitions in langmuir–blodgett films. iii. polarized raman studies of cadmium arachidate using integrated optical techniques," *The Journal of Chemical Physics*, vol. 86, pp. 1601–1607, 01 1987.

[62] J. S. Kanger, C. Otto, M. Slotboom, and J. Greve, "Waveguide raman spectroscopy of thin polymer layers and monolayers of biomolecules using high refractive index waveguides," *The Journal of Physical Chemistry*, vol. 100, no. 8, pp. 3288–3292, 1996.

[63] A. Pope, A. Schulte, Y. Guo, L. Ono, B. R. Cuenya, C. Lopez, K. Richardson, K. Kitanovski, and T. Winningham, "Chalcogenide waveguide structures as substrates and guiding layers for evanescent wave raman spectroscopy of bacteriorhodopsin," *Vibrational Spectroscopy*, vol. 42, no. 2, pp. 249 – 253, 2006.

[64] C. C. Evans, C. Liu, and J. Suntivich, "Tio2 nanophotonic sensors for efficient integrated evanescent raman spectroscopy," *ACS Photonics*, vol. 3, no. 9, pp. 1662–1669, 2016.

[65] S. A. Holmstrom, T. H. Stievater, D. A. Kozak, M. W. Pruessner, N. Tyndall, W. S. Rabinovich, R. A. McGill, and J. B. Khurgin, "Trace gas raman spectroscopy using functionalized waveguides," *Optica*, vol. 3, pp. 891–896, Aug 2016.

[66] A. Dhakal, P. C. Wuytens, F. Peyskens, K. Jans, N. L. Thomas, and R. Baets, "Nanophotonic waveguide enhanced raman spectroscopy of biological submonolayers," *ACS Photonics*, vol. 3, no. 11, pp. 2141–2149, 2016.

[67] D. A. Coucheron, D. N. Wadduwage, G. S. Murugan, P. T. C. So, and B. S. Ahluwalia, "Chip-based resonance raman spectroscopy using tantalum pentoxide waveguides," *IEEE Photonics Technology Letters*, vol. 31, no. 14, pp. 1127–1130, 2019.

[68] A. Dhakal, *Nanophotonic Waveguide Enhanced Raman Spectroscopy*. PhD thesis, Ghent University, 9 2016.

[69] F. Peyskens, *Surface Enhanced Raman Spectroscopy Using a Single Mode Nanophotonic-Plasmonic Platform*. PhD thesis, Ghent University, 5 2016.

[70] A. Raza, S. Clemmen, P. Wuytens, M. de Goede, A. S. K. Tong, N. L. Thomas, C. Liu, J. Suntivich, A. G. Skirtach, S. M. Garcia-Blanco, D. J. Blumenthal, J. S. Wilkinson, and R. Baets, "High index contrast photonic platforms for on-chip raman spectroscopy," *Opt. Express*, vol. 27, pp. 23067–23079, Aug 2019.

[71] A. Dhakal, P. Wuytens, A. Raza, N. Le Thomas, and R. Baets, "Silicon nitride background in nanophotonic waveguide enhanced raman spectroscopy," *Materials*, no. 2, 2017.

[72] N. L. Thomas, A. Dhakal, A. Raza, F. Peyskens, and R. Baets, "Impact of fundamental thermodynamic fluctuations on light propagating in

photonic waveguides made of amorphous materials," *Optica*, vol. 5, pp. 328–336, Apr 2018.

[73] S. Lin, W. Zhu, Y. Jin, and K. B. Crozier, "Surface-enhanced raman scattering with ag nanoparticles optically trapped by a photonic crystal cavity," *Nano Letters*, vol. 13, no. 2, pp. 559–563, 2013. PMID: 23339834.

[74] L. Kong, C. Lee, C. M. Earhart, B. Cordovez, and J. W. Chan, "A nanotweezer system for evanescent wave excited surface enhanced raman spectroscopy (sers) of single nanoparticles," *Opt. Express*, vol. 23, pp. 6793–6802, Mar 2015.

[75] P. Measor, L. Seballos, D. Yin, J. Z. Zhang, E. J. Lunt, A. R. Hawkins, and H. Schmidt, "On-chip surface-enhanced raman scattering detection using integrated liquid-core waveguides," *Applied Physics Letters*, vol. 90, no. 21, p. 211107, 2007.

[76] M. Fan, G. F. Andrade, and A. G. Brolo, "A review on the fabrication of substrates for surface enhanced raman spectroscopy and their applications in analytical chemistry," *Analytica Chimica Acta*, vol. 693, no. 1, pp. 7 – 25, 2011.

[77] F. Peyskens, A. Dhakal, P. Van Dorpe, N. Le Thomas, and R. Baets, "Surface enhanced raman spectroscopy using a single mode nanophotonic-plasmonic platform," *ACS Photonics*, vol. 3, no. 1, pp. 102–108, 2016.

[78] P. C. Wuytens, A. G. Skirtach, and R. Baets, "On-chip surface-enhanced raman spectroscopy using nanosphere-lithography patterned antennas on silicon nitride waveguides," *Opt. Express*, vol. 25, pp. 12926–12934, May 2017.

[79] A. Raza, S. Clemmen, P. Wuytens, M. Muneeb, M. Van Daele, J. Dendooven, C. Detavernier, A. Skirtach, and R. Baets, "Ald assisted nanoplasmonic slot waveguide for on-chip enhanced raman spectroscopy," *APL Photonics*, vol. 3, no. 11, p. 116105, 2018.

[80] R. Pilot, R. Signorini, C. Durante, L. Orian, M. Bhamidipati, and L. Fabris, "A review on surface-enhanced raman scattering," *Biosensors*, vol. 9, no. 57, 2019.

[81] B. Turk, "Targeting proteases: successes, failures and future prospects," *Nature Reviews Drug Discovery*, vol. 5, no. 9, 2006.

[82] "Peptide synthesis." https://en.wikipedia.org/wiki/Peptide_synthesis. Accessed: June 17, 2020.

[83] L. A. Urry, M. L. Cain, S. A. Wasserman, P. V. Minorsky, and J. B. Reece, *Campbell Biology*. Pearson, 2020.

[84] "Activation energy." https://en.wikipedia.org/wiki/Activation_energy. Accessed: May 5, 2020.

[85] "Classification and nomenclature of enzymes by the reactions they catalyse." https://web.archive.org/web/20150317054348/http://www.chem.qmul.ac.uk/iubmb/enzyme/rules.html. Accessed: June 17, 2020.

[86] E. Fischer, "Einfluss der configuration auf die wirkung der enzyme," *Berichte der deutschen chemischen Gesellschaft*, vol. 27, no. 3, pp. 2985–2993, 1894.

[87] D. E. Koshland, "Application of a theory of enzyme specificity to protein synthesis," *Proceedings of the National Academy of Sciences*, vol. 44, no. 2, pp. 98–104, 1958.

[88] "Induced fit." https://en.wikipedia.org/wiki/Enzyme#cite_note-url_Enzyme_Classification-20. Accessed: June 17, 2020.

[89] "Merops database of peptidases." https://www.ebi.ac.uk/merops/cgi-bin/statistics_index?type=P. Accessed: June 17, 2020.

[90] I. M. Verhamme, S. E. Leonard, and R. C. Perkins, *Proteases: Pivot Points in Functional Proteomics*, pp. 313–392. New York, NY: Springer New York, 2019.

[91] A. Laskar and A. Chatterjee, "Protease – revisting the types and potential," *Online Journal of Biotechnology Research (OJBR)*, vol. 1(1), pp. 55–61, 01 2009.

[92] E. Vandermarliere, M. Mueller, and L. Martens, "Getting intimate with trypsin, the leading protease in proteomics," *Mass Spectrometry Reviews*, vol. 32, no. 6, pp. 453–465, 2013.

[93] N. D. Rawlings and A. J. Barrett, "[2] families of serine peptidases," in *Proteolytic Enzymes: Serine and Cysteine Peptidases*, vol. 244 of *Methods in Enzymology*, pp. 19 – 61, Academic Press, 1994.

[94] "Sequencing grade modified trypsin." https://be.promega.com/products/mass-spectrometry/proteases-and-surfactants/sequencing-grade-modified-trypsin/?catNum=V5111. Accessed: May 5, 2020.

[95] "Catalytic mechanism of trypsin and other serine proteases." https://proteopedia.org/wiki/index.php/Image:Serine_protease_ mechanism_by_snellios.png. Accessed: November 9, 2020.

[96] "Sequencing grade glu-c." https://be.promega.com/products/mass-spectrometry/proteases-and-surfactants/glu_c_-sequencing-grade/?catNum=V1651. Accessed: May 5, 2020.

[97] J. Houmard and G. R. Drapeau, "Staphylococcal protease: A proteolytic enzyme specific for glutamoyl bonds," *Proceedings of the National Academy of Sciences*, vol. 69, no. 12, pp. 3506–3509, 1972.

[98] S. Krishnaswamy, "Exosite-driven substrate specificity and function in coagulation," *Journal of Thrombosis and Haemostasis*, vol. 3, no. 1, pp. 54–67, 2005.

[99] D. C. RIJKEN and H. R. LIJNEN, "New insights into the molecular mechanisms of the fibrinolytic system," *Journal of Thrombosis and Haemostasis*, vol. 7, no. 1, pp. 4–13, 2009.

[100] R. Düsing and F. Sellers, "Ace inhibitors, angiotensin receptor blockers and direct renin inhibitors in combination: a review of their role after the ontarget trial," *Current Medical Research and Opinion*, vol. 25, no. 9, pp. 2287–2301, 2009. PMID: 19635044.

[101] H. C. Maisey, K. S. Doran, and V. Nizet, "Recent advances in understanding the molecular basis of group b streptococcus virulence," *Expert Reviews in Molecular Medicine*, vol. 10, p. e27, 2008.

[102] T. Imamura, J. Potempa, and J. Travis, "Activation of the kallikrein-kinin system and release of new kinins through alternative cleavage of kininogens by microbial and human cell proteinases," *Biological Chemistry*, vol. 385, no. 11, pp. 989 – 996, 2004.

[103] C. M. Overall and R. A. Dean, "Degradomics: Systems biology of the protease web. pleiotropic roles of mmps in cancer," *Cancer and Metastasis Reviews*, vol. 25, no. 1, 2006.

[104] J. Hu, P. E. Van den Steen, Q.-X. A. Sang, and G. Opdenakker, "Matrix metalloproteinase inhibitors as therapy for inflammatory and

vascular diseases," *Nature Reviews Drug Discovery*, vol. 6, no. 6, 2007.

[105] J. Adams and M. Kauffman, "Development of the proteasome inhibitor velcad (bortezomib)," *Cancer Investigation*, vol. 22, no. 2, pp. 304–311, 2004. PMID: 15199612.

[106] D. R. Green and G. I. Evan, "A matter of life and death," *Cancer Cell*, vol. 1, no. 1, pp. 19 – 30, 2002.

[107] B. F. Mohamed, Mona Mostafa amd Sloane, "Multifunctional enzymes in cancer," *Nature Reviews Cancer*, vol. 6, no. 10, 2006.

[108] A. D. Schimmer, K. Welsh, C. Pinilla, Z. Wang, M. Krajewska, M.-J. Bonneau, I. M. Pedersen, S. Kitada, F. L. Scott, B. Bailly-Maitre, G. Glinsky, D. Scudiero, E. Sausville, G. Salvesen, A. Nefzi, J. M. Ostresh, R. A. Houghten, and J. C. Reed, "Small-molecule antagonists of apoptosis suppressor xiap exhibit broad antitumor activity," *Cancer Cell*, vol. 5, no. 1, pp. 25 – 35, 2004.

[109] C. Flexner, G. Bate, and P. Kirkpatrick, "Tipranavir," *Nature Reviews Drug Discovery*, vol. 4, no. 12, 2005.

[110] C. G. SMITH and J. R. VANE, "The discovery of captopril," *The FASEB Journal*, vol. 17, no. 8, pp. 788–789, 2003. PMID: 12724335.

[111] X. Ding and K.-L. Yang, "Quantitative serine protease assays based on formation of copper(ii)–oligopeptide complexes," *Analyst*, vol. 140, pp. 340–345, 2015.

[112] Z. Zhou, L. Peng, X. Wang, Y. Xiang, and A. Tong, "A new colorimetric strategy for monitoring caspase 3 activity by hrp-mimicking dnazyme–peptide conjugates," *Analyst*, vol. 139, pp. 1178–1183, 2014.

[113] "3. general principles for the assay of proteases with chromogenic substrates," *Scandinavian Journal of Clinical and Laboratory Investigation*, vol. 42, no. sup162, pp. 25–32, 1982.

[114] "Protease assays." https://www.ncbi.nlm.nih.gov/books/NBK92006/. Accessed: June 17, 2020.

[115] H. Wang, D. N. Udukala, T. N. Samarakoon, M. T. Basel, M. Kalita, G. Abayaweera, H. Manawadu, A. Malalasekera, C. Robinson, D. Villanueva, P. Maynez, L. Bossmann, E. Riedy, J. Barriga, N. Wang,

P. Li, D. A. Higgins, G. Zhu, D. L. Troyer, and S. H. Bossmann, "Nanoplatforms for highly sensitive fluorescence detection of cancer-related proteases," *Photochem. Photobiol. Sci.*, vol. 13, pp. 231–240, 2014.

[116] T. M. Feltrup and B. R. Singh, "Development of a fluorescence internal quenching correction factor to correct botulinum neurotoxin type a endopeptidase kinetics using snaptide," *Analytical Chemistry*, vol. 84, no. 24, pp. 10549–10553, 2012. PMID: 23181535.

[117] E. A. Jares-Erijman and T. M. Jovin, "Fret imaging," *Nature Biotechnology*, vol. 21, no. 11, 2003.

[118] X. Han, A. Aslanian, and J. R. Yates, "Mass spectrometry for proteomics," *Current Opinion in Chemical Biology*, vol. 12, no. 5, pp. 483 – 490, 2008. Analytical Techniques/Mechanisms.

[119] X. He and N. Ma, "Biomimetic synthesis of fluorogenic quantum dots for ultrasensitive label-free detection of protease activities," *Small*, vol. 9, no. 15, pp. 2527–2531, 2013.

[120] X. Ding, D. Ge, and K.-L. Yang, "Colorimetric protease assay by using gold nanoparticles and oligopeptides," *Sensors and Actuators B: Chemical*, vol. 201, pp. 234 – 239, 2014.

[121] A. V. Fuchs, N. Kotman, J. Andrieu, V. Mailänder, C. K. Weiss, and K. Landfester, "Enzyme cleavable nanoparticles from peptide based triblock copolymers," *Nanoscale*, vol. 5, pp. 4829–4839, 2013.

[122] G. B. Kim and Y.-P. Kim, "Analysis of protease activity using quantum dots and resonance energy transfer," *Theranostics*, vol. 2, pp. 127–138, 2012.

[123] L. Jin, K. Yang, K. Yao, S. Zhang, H. Tao, S.-T. Lee, Z. Liu, and R. Peng, "Functionalized graphene oxide in enzyme engineering: A selective modulator for enzyme activity and thermostability," *ACS Nano*, vol. 6, no. 6, pp. 4864–4875, 2012. PMID: 22574614.

[124] J. Li, C.-H. Lu, Q.-H. Yao, X.-L. Zhang, J.-J. Liu, H.-H. Yang, and G.-N. Chen, "A graphene oxide platform for energy transfer-based detection of protease activity," *Biosensors and Bioelectronics*, vol. 26, no. 9, pp. 3894 – 3899, 2011.

[125] R. A. Marcus, "Chemical and electrochemical electron-transfer theory," *Annual Review of Physical Chemistry*, vol. 15, no. 1, pp. 155–196, 1964.

[126] J. Ji, J. Gan, J. Kong, P. Yang, B. Liu, and C. Ji, "Electrochemical detection of the activities of thrombin and its inhibitor," *Electrochemistry Communications*, vol. 16, no. 1, pp. 53 – 56, 2012.

[127] H. Ko, S. Park, and K. Kim, "Aptamer-free electrochemical detection of thrombin based on coagulation reaction of ferrocene-labeled fibrinogen," *Journal of Electroanalytical Chemistry*, vol. 742, pp. 70 – 73, 2015.

[128] H. Wu, S. Liu, J. Jiang, G. Shen, and R. Yu, "A novel electrochemical biosensor for highly selective detection of protease biomarker from bacillus licheniformis with d-amino acid containing peptide," *Analyst*, vol. 137, pp. 4829–4833, 2012.

[129] Y.-F. Liu, J.-X. Chen, M.-Q. Xu, and G.-C. Zhao, "A novel photoelectrochemical platform for detection of protease," *Int. J. Electrochem. Sci.*, vol. 9, 2014.

[130] P. G. de Gennes and J. Prost, *The Physics of Liquid Crystals*. Clarendon Press, 1993.

[131] X. Bi, S. L. Lai, and K.-L. Yang, "Liquid crystal multiplexed protease assays reporting enzymatic activities as optical bar charts," *Analytical Chemistry*, vol. 81, no. 13, pp. 5503–5509, 2009. PMID: 19492802.

[132] Q. Ouyang, S. Zeng, L. Jiang, L. Hong, G. Xu, X.-Q. Dinh, J. Qian, S. He, J. Qu, P. Coquet, and K.-T. Yong, "Sensitivity enhancement of transition metal dichalcogenides/silicon nanostructure-based surface plasmon resonance biosensor," *Scientific Reports*, vol. 6, no. 1, 2016.

[133] J. Homola, "Present and future of surface plasmon resonance biosensors," *Analytical and Bioanalytical Chemistry*, vol. 377, 2013.

[134] C. Esseghaier, A. Ng, and M. Zourob, "A novel and rapid assay for hiv-1 protease detection using magnetic bead mediation," *Biosensors and Bioelectronics*, vol. 41, pp. 335 – 341, 2013.

[135] L. Chen, X. Fu, and J. Li, "Ultrasensitive surface-enhanced raman scattering detection of trypsin based on anti-aggregation of 4-mercaptopyridine-functionalized silver nanoparticles: an optical

sensing platform toward proteases," *Nanoscale*, vol. 5, pp. 5905–5911, 2013.

[136] Z. Wu, Y. Liu, X. Zhou, A. Shen, and J. Hu, "A "turn-off" sers-based detection platform for ultrasensitive detection of thrombin based on enzymatic assays," *Biosensors and Bioelectronics*, vol. 44, pp. 10 – 15, 2013.

[137] C. Sun, K.-H. Su, J. Valentine, Y. T. Rosa-Bauza, J. A. Ellman, O. Elboudwarej, B. Mukherjee, C. S. Craik, M. A. Shuman, F. F. Chen, and X. Zhang, "Time-resolved single-step protease activity quantification using nanoplasmonic resonator sensors," *ACS Nano*, vol. 4, no. 2, pp. 978–984, 2010. PMID: 20121209.

[138] J. Moger, P. Gribbon, A. Sewing, and C. Winlove, "Feasibility study using surface-enhanced raman spectroscopy for the quantitative detection of tyrosine and serine phosphorylation," *Biochimica et Biophysica Acta (BBA) - General Subjects*, vol. 1770, no. 6, pp. 912 – 918, 2007.

[139] C. L. Weeks, A. Polishchuk, Z. Getahun, W. F. DeGrado, and T. G. Spiro, "Investigation of an unnatural amino acid for use as a resonance raman probe: detection limits and solvent and temperature dependence of the ν c$\equiv$n band of 4-cyanophenylalanine," *Journal of Raman Spectroscopy*, vol. 39, no. 11, pp. 1606–1613, 2008.

[140] H.-J. van Manen, A. Lenferink, and C. Otto, "Noninvasive imaging of protein metabolic labeling in single human cells using stable isotopes and raman microscopy," *Analytical Chemistry*, vol. 80, no. 24, pp. 9576–9582, 2008. PMID: 19006335.

[141] F. Wei, D. Zhang, N. J. Halas, and J. D. Hartgerink, "Aromatic amino acids providing characteristic motifs in the raman and sers spectroscopy of peptides," *The Journal of Physical Chemistry B*, vol. 112, no. 30, pp. 9158–9164, 2008. PMID: 18610961.

[142] S. S. Masango, R. A. Hackler, N. Large, A.-I. Henry, M. O. McAnally, G. C. Schatz, P. C. Stair, and R. P. Van Duyne, "High-resolution distance dependence study of surface-enhanced raman scattering enabled by atomic layer deposition," *Nano Letters*, vol. 16, no. 7, pp. 4251–4259, 2016. PMID: 27243108.

[143] H. Häkkinen, "The gold–sulfur interface at the nanoscale," *Nature Chemistry*, vol. 4, no. 6, 2012.

[144] R. Lévy, N. T. K. Thanh, R. C. Doty, I. Hussain, R. J. Nichols, D. J. Schiffrin, M. Brust, and D. G. Fernig, "Rational and combinatorial design of peptide capping ligands for gold nanoparticles," *Journal of the American Chemical Society*, vol. 126, no. 32, pp. 10076–10084, 2004. PMID: 15303884.

[145] L. Duchesne, D. Gentili, M. Comes-Franchini, and D. G. Fernig, "Robust ligand shells for biological applications of gold nanoparticles," *Langmuir*, vol. 24, no. 23, pp. 13572–13580, 2008. PMID: 18991409.

[146] M. POZSGAY, G. CS. SZABÓ, P. ELÖDI, R. GÁSPÁR, S. BAJUSZ, and R. SIMONSSON, "Investigation of the substrate-binding site of trypsin by the aid of tripeptidyl-p-nitroanilide substrates," *European Journal of Biochemistry*, vol. 115, no. 3, pp. 497–502, 1981.

[147] K. BREDDAM and M. MELDAL, "Substrate preferences of glutamic-acid-specific endopeptidases assessed by synthetic peptide substrates based on intramolecular fluorescence quenching," *European Journal of Biochemistry*, vol. 206, no. 1, pp. 103–107, 1992.

[148] N. Turk, P. Wuytens, A. Raza, A. Skirtach, and R. Baets, "Organic adhesion layer for an increased waveguide-excited surface-enhanced raman signal," in *Frontiers in Optics 2017* [148].

[149] N. Turk, A. Raza, P. Wuytens, H. Demol, M. Van Daele, C. Detavernier, A. Skirtach, K. Gevaert, and R. Baets, "Comparison of free-space and waveguide-based sers platforms," *Nanomaterials*, vol. 9, no. 10, 2019.

[150] N. Turk, A. Skirtach, K. Gevaert, and R. Baets, "Hydrogen plasma cleaning of gold plasmonic nanostructures for better reproducibility of the sers spectra," in *Proceedings of the 24th Annual Symposium of the IEEE Photonics Benelux Chapter*.

[151] T. G. Habteyes, S. Dhuey, E. Wood, D. Gargas, S. Cabrini, P. J. Schuck, A. P. Alivisatos, and S. R. Leone, "Metallic adhesion layer induced plasmon damping and molecular linker as a nondamping alternative," *ACS Nano*, vol. 6, no. 6, pp. 5702–5709, 2012. PMID: 22646820.

[152] M. Lamy de la Chapelle, H. Shen, N. Guillot, B. Frémaux, B. Guelorget, and T. Toury, "New gold nanoparticles adhesion process opening the way of improved and highly sensitive plasmonics technologies," *Plasmonics*, vol. 8, no. 2, pp. 411–415, 2013.

[153] M. Boerkamp, T. van Leest, J. Heldens, A. Leinse, M. Hoekman, R. Heideman, and J. Caro, "On-chip optical trapping and raman spectroscopy using a triplex dual-waveguide trap," *Opt. Express*, vol. 22, pp. 30528–30537, Dec 2014.

[154] F. Peyskens, P. Wuytens, A. Raza, P. V. Dorpe, and R. Baets, "Waveguide excitation and collection of surface-enhanced raman scattering from a single plasmonic antenna," *Nanophotonics*, vol. 7, no. 7, 2018.

[155] F. Tang, P.-M. Adam, and S. Boutami, "Theoretical investigation of sers nanosensors based on hybrid waveguides made of metallic slots and dielectric strips," *Opt. Express*, vol. 24, pp. 21244–21255, Sep 2016.

[156] S. Li, L. Xia, X. Chen, Z. Yang, and W. Li, "Surface-enhanced raman scattering sensor based on hybrid deep slot waveguide on an integrated photonic platform," *J. Opt. Soc. Am. B*, vol. 36, pp. 2423–2428, Sep 2019.

[157] H. M. K. Wong, M. K. Dezfouli, L. Sun, S. Hughes, and A. S. Helmy, "Nanoscale plasmonic slot waveguides for enhanced raman spectroscopy," *Phys. Rev. B*, vol. 98, p. 085124, Aug 2018.

[158] Q. Cao, J. Feng, H. Lu, H. Zhang, F. Zhang, and H. Zeng, "Surface-enhanced raman scattering using nanoporous gold on suspended silicon nitride waveguides," *Opt. Express*, vol. 26, pp. 24614–24620, Sep 2018.

[159] Y. C. Jun, R. D. Kekatpure, J. S. White, and M. L. Brongersma, "Nonresonant enhancement of spontaneous emission in metal-dielectric-metal plasmon waveguide structures," *Phys. Rev. B*, vol. 78, p. 153111, Oct 2008.

[160] P. Du, X. Zhang, H. Yin, Y. Zhao, L. Liu, Z. Wu, and H. Xu, "In situ surface-enhanced raman scattering monitoring of reduction of 4-nitrothiophenol on bifunctional metallic nanostructure," *Japanese Journal of Applied Physics*, vol. 57, p. 030308, feb 2018.

[161] S. M. Barnett, N. Harris, and J. J. Baumberg, "Molecules in the mirror: how sers backgrounds arise from the quantum method of images," *Phys. Chem. Chem. Phys.*, vol. 16, pp. 6544–6549, 2014.

[162] S. Mahajan, R. M. Cole, J. D. Speed, S. H. Pelfrey, A. E. Russell, P. N. Bartlett, S. M. Barnett, and J. J. Baumberg, "Understanding the

surface-enhanced raman spectroscopy "background"," *The Journal of Physical Chemistry C*, vol. 114, no. 16, pp. 7242–7250, 2010.

[163] K. Ikeda, S. Suzuki, and K. Uosaki, "Enhancement of sers background through charge transfer resonances on single crystal gold surfaces of various orientations," *Journal of the American Chemical Society*, vol. 135, no. 46, pp. 17387–17392, 2013.

[164] J. T. Hugall and J. J. Baumberg, "Demonstrating photoluminescence from au is electronic inelastic light scattering of a plasmonic metal: The origin of sers backgrounds," *Nano Letters*, vol. 15, no. 4, pp. 2600–2604, 2015. PMID: 25734469.

[165] Z. Liu, H. Zhao, A. Raza, N. Le Thomas, and R. Baets, "On the performance of tantalum pentoxide and silicon nitride slot waveguides for on-chip raman spectroscopy," in *21st European Conference on Integrated Optics (ECIO 2019), Proceedings*, p. 3, 2019.

[166] J.-D. Liao, M.-C. Wang, C.-C. Weng, R. Klauser, S. Frey, M. Zharnikov, and M. Grunze, "Modification of alkanethiolate self-assembled monolayers by free radical-dominant plasma," *The Journal of Physical Chemistry B*, vol. 106, no. 1, pp. 77–84, 2002.

[167] H. P. Erickson, "Size and shape of protein molecules at the nanometer level determined by sedimentation, gel filtration, and electron microscopy," *Biological Procedures Online*, vol. 11, no. 1, 2009.

[168] J. C. Powers, J. L. Asgian, O. D. Ekici, and K. E. James, "Irreversible inhibitors of serine, cysteine, and threonine proteases," *Chemical Reviews*, vol. 102, no. 12, pp. 4639–4750, 2002.

[169] G. Ertürk, M. Hedström, and B. Mattiasson, "A sensitive and real-time assay of trypsin by using molecular imprinting-based capacitive biosensor," *Biosensors and Bioelectronics*, vol. 86, pp. 557 – 565, 2016.

[170] L. Hu, S. Han, S. Parveen, Y. Yuan, L. Zhang, and G. Xu, "Highly sensitive fluorescent detection of trypsin based on bsa-stabilized gold nanoclusters," *Biosensors and Bioelectronics*, vol. 32, no. 1, pp. 297 – 299, 2012.

[171] Y. Lai, S. Sun, T. He, S. Schlücker, and Y. Wang, "Raman-encoded microbeads for spectral multiplexing with sers detection," *RSC Adv.*, vol. 5, pp. 13762–13767, 2015.

[172] S. Shalini, L. Dorstyn, S. Dawar, and S. Kumar, "Old, new and emerging functions of caspases," *Cell Death & Differentiation*, vol. 22, no. 4, 2015.

[173] T. Hunter, "Tyrosine phosphorylation: thirty years and counting," *Curr Opin Cell Biol*, vol. 21, no. 2, pp. 140–146, 2009.

[174] "Amino acids." https://www.technologynetworks.com/applied-sciences/articles/essential-amino-acids-chart-abbreviations-and-structure-324357. Accessed: June 17, 2020.

[175] W. Chan and P. White, *Fmoc Solid Phase Peptide Synthesis*. Oxford University Press, 1999.

[176] A. Isidro-Llobet, M. Álvarez, and F. Albericio, "Amino acid-protecting groups," *Chemical Reviews*, vol. 109, no. 6, pp. 2455–2504, 2009. PMID: 19364121.

[177] G. B. Fields, *Peptide Characterization and Application Protocols*. Humana Press, 2007.

[178] "Solid state peptide synthesis." https://en.chem-station.com/reactions-2/2014/02/merrifield-solid-phase-peptide-synthesis.html. Accessed: June 17, 2020.

[179] "Chromatography." https://chembam.com/techniques/chromatography/adsorption-chromatography/. Accessed: June 17, 2020.

[180] "Schematic of hplc." https://www.analyticaltoxicology.com/en/high-performance-liqud-chromatography-hplc/. Accessed: May 5, 2020.

[181] F. Hillenkamp, M. Karas, R. C. Beavis, and B. T. Chait, "Matrix-assisted laser desorption/ionization mass spectrometry of biopolymers," *Analytical Chemistry*, vol. 63, no. 24, pp. 1193A–1203A, 1991. PMID: 1789447.

[182] M. Karas and R. Kruger, "Ion formation in maldi: The cluster ionization mechanism," *Chemical Reviews*, vol. 103, no. 2, pp. 427–440, 2003. PMID: 12580637.

[183] "Maldi working principle." https://www.creative-proteomics.com/technology/maldi-tof-mass-spectrometry.htm. Accessed: June 17, 2020.

[184] S. Ma, S. K. Chowdhury, and K. B. Alton, "Application of mass spectrometry for metabolite identification," *Current Drug Metabolism*, vol. 7, no. 5, 2006.

[185] J. De Gelder, K. De Gussem, P. Vandenabeele, and L. Moens, "Reference database of raman spectra of biological molecules," *Journal of Raman Spectroscopy*, vol. 38, no. 9, pp. 1133–1147, 2007.

[186] Y. Zou, K. Razmkhah, N. P. Chmel, I. W. Hamley, and A. Rodger, "Spectroscopic signatures of an fmoc–tetrapeptide, fmoc and fluorene," *RSC Adv.*, vol. 3, pp. 10854–10858, 2013.